Hadean water-dew cycles drive the evolution of DNA and protocells

Alan Ianeselli

München 2022

Hadean water-dew cycles drive the evolution of DNA and protocells

Alan Ianeselli

Dissertation
der Fakultät für Physik
der Ludwig-Maximilians-Universität
München

vorgelegt von
Alan Ianeselli
aus Bozen

München, 28. Februar 2022

Contents

List of Figures

Zusammenfassung

Flüssiges Wasser ist eine Grundvoraussetzung für jede Form von Leben. Auf der Erde ist es ubiquitär in Form von Regen, Nebel oder Tau, und der Wechsel zwischen diesen Formen erfordert einen kontinuierlichen Energiezufluss. Solche Wasserverdampfungs-Kondensations-zyklen können global durch die Sonne oder lokal durch Temperaturunterschiede verursacht werden. Unterschiedlich erhitzte Gesteinsporen auf der hadeanischen Erde bieten eben diese Ungleichgewichtsbedingungen, die Wasser zu verdampfen und als Nebel und Tau wieder zu kondensieren lassen. Die daraus resultierenden mikroskala Wasser-Tau-Zyklen werden durch die Oberflächenspannung des Wassers angetrieben und führen zu periodischen Schwankungen in der Konzentration von Salzen und Molekülen, des pH-Werts und des Feucht-Trocken-Zustands

Diese mikroskala Wasserkreisläufe könnten die Evolution langer DNAs vorantreiben und Antworten auf die noch ungelösten Probleme im Kern der DNA-Evolution liefern: das Problem der Strangtrennung und die Spiegelmann'sche "Tyrannei der kürzesten Stränge". Die salzarmen Tautropfen versauerten in der CO_2-reichen Hadean-Atmosphäre und induzierten die Denaturierung von Oligonukleotiden 30 K unter der typischen Schmelztemperaturen und sorgten so für niedrige Hydrolyseraten. Der Großteil der Flüssigkeit hingegen bewahrt eine hohe Salzkonzentration und einen neutralen pH-Wert, wodurch die einzelsträngigen DNAs schnell repliziert werden konnten. Die erhitzten Gas-Wasser-Grenzflächen reicherten bevorzugt Oligonukleotide mit zunehmender Längen bis zum 10'000-fachen an, die schließlich nach dem Kaffeering-Effekt trockneten. Die extremen Konzentrationen, die während der DNA-Nass-Trocken-Zyklen erreicht wurden, lösten ein unspezifisches Annealing der Stränge, die sich zu längeren Sequenzen (von 50 nt bis 1300 nt) von zunehmender Komplexität rekombinierten und damit das Spiegelmann'sche Dilemma aufhoben. Ihre ATGC-Zusammensetzung wurde durch die Schmelzbedingungen des Taus selektiert, der lange, mit AT angereicherte Sequenzen bevorzugte.

Die mikroskala Wasserkreisläufe förderten auch den Aufbau und die Teilung von Urzellen. Komplexe Koazervat-Mikrotröpfchen aus RNA, Polyzuckern und Polypeptiden begannen ihren Zusammenbau an den erhitzten Gas-Wasser-Grenzflächen, wo sie dann weiter verschmolzen und wuchsen. Die unterschiedliche Anhäufung von Molekülen an den Gas-Wasser-Grenzflächen bestimmte auch die endgültige Zusammensetzung der Protozellen. Die durch die Wasser-Tau-Zyklen verursachten perturbativen Strömungen führten zur Dehnung oder Fragmentierung der Koazervattröpfchen, die sich ausdehnten und in Tochterprotozellen teilten. Diese Art der Teilung konnte bisher in keiner anderen Umgebung er-

reicht werden.

Unsere Ergebnisse zeigen ein wichtiges, fehlendes Bindeglied zwischen der Geophysik der frühen Erde und der Chemie, die für die Entstehung von Leben erforderlich ist. Frühes Leben könnte im Inneren der Erde, in erhitzten Poren von Vulkangestein beherbergt worden sein, zwischen Kondensation Tautropfen unter intensiven Nass-Trocken-, pH- und Salzzyklen.

Abstract

Liquid water is a fundamental requirement for any form of life. On Earth, it can ubiquitously be found in the form of bulk, fog or dew, and cycling between them requires a continuous influx of energy. These water evaporation-condensation cycles can be provided globally by the sun, or locally by differences in temperatures. Differentially heated rock pores on the Hadean Earth present the non-equilibrium conditions to evaporate bulk water and re-condense it as fog and dew. The resulting microscale bulk-dew cycles are driven by the surface tension of water and lead to periodic oscillations in the concentration of salts and molecules, pH and wet-dry states.

These microscale water cycles could drive the evolution of long DNAs, overriding the yet-to-be-solved issues at the core of DNA evolution: the strand separation problem and Spiegelmann's "tyranny of the shortest strands". The low-salt dew droplets acidified in the CO_2-rich Hadean atmosphere and induced the denaturation of oligonucleotides 30 K below their melting temperatures, thus maintaining low hydrolysis rates. The bulk instead retained high salts and neutral pH that promptly replicated the single-stranded DNAs. The heated gas-water interfaces preferentially accumulated oligonucleotides of increasing lengths up to 10'000 fold, which eventually dried after the coffee-ring effect. The extreme concentrations reached during the DNA wet-dry cycles triggered unspecific annealing of the strands, which recombined into longer sequences (from 50 nt up to 1300 nt) of increased complexity, overriding Spiegelmann's dilemma. Their ATGC composition was biased by the melting conditions of the dew, that selected long sequences enriched in AT.

The microscale water cycles also promoted the assembly and division of primordial cells. Complex coacervate microdroplets made of RNA, poly-sugars and poly-peptides initiated their assembly at the heated gas-water interfaces, where they then continued to fuse and grow. The differential accumulation of molecules at the gas-water interfaces also drove the final composition of the protocells. The perturbative flows caused by the water-dew cycles led to the stretching or fragmentation of the coacervate droplets, which elongated and divided into daughter protocells. These types of division could not yet be achieved in any other environment.

Our results show an important missing link between the geophysics of the early Earth and the chemistry required for life to form. Early life could have been harbored inside the non-equilibrium of the heated pores of volcanic rock, oscillating between condensation droplets of dew under intense wet-dry, pH and salt cycles.

The DNA and RNA replicators on the early Earth

The replication of the genetic information, in the form of DNA or RNA, is essential for the first steps of Darwinian evolution during the origin of life. During these early stages of evolution, some issues still remain unclear:

- How could the oligonucleotide strands separate in the salt-rich conditions that are necessary for the prebiotic replication chemistries?

- How could the longer sequences be preserved under Spiegelman's "tyranny of the shortest"?

- How could long sequences with biased composition emerge in the immense entropic land of the sequence space?

Many proposed chemistries for the prebiotic replication of oligonucleotides require high concentration of ions to work[1], for example Na^+, Mg^{2+}. They strongly stabilize oligomers in the duplex form, which can even achieve melting temperatures higher than 100 °C in salt-rich solutions. Moreover, ions catalyze the hydrolysis of RNA and chemical reagents when temperatures are increased[2,3]. Heat-induced denaturation seems therefore to not be a viable route for RNA melting[4]. Other studies suggest denaturation methods such as low pH[5] or chaotropic agents[6,7], but how they can be integrated in a primordial replicative system remains unclear.

A primordial replicator of oligonucleotides must also drive the evolution of the sequence information. Spiegelman observed that during replication the longer oligomers are quickly lost, because the shorter ones replicate with a faster kinetics and quickly outcompete them. Mutations that cause shortening in the sequences start an evolutionary race towards the shortest oligomers, leading to a progressive loss of the longer ones. This phenomenon is known as the 'tyranny of the shortest' and is a problem for the onset of Darwinian evolution[8].

Also, the sequence space of long oligomers is an immensely vast entropic land. During standard replicative conditions, the spontaneous emergence of sequences that contain particular motifs or that are enriched in specific nucleotides is extremely rare. Without a selective pressure, any sequence bias that could give an informational or catalytical advantage is likely to not emerge and remain unexplored[9].

These problems must be investigated in the context of the geo-physics of the primordial Earth. As we will see, lab models of heated volcanic rock pores in a Hadean atmosphere present the non-equilibrium conditions to host microscale water-dew cycles that could drive the molecular evolution of DNA.

Chapter 1

Water raindrops denature DNA and RNA

This chapter corresponds to the paper from Ianeselli *et al.* published in *Angewandte Chemie* in 2019 (attachment A).

The concentration of salts like NaCl, the major component of oceanic water, determines the melting temperature of oligonucleotides over a wide range[10,11]. Positive ions (e.g. Na$^+$) screen the repulsion between the phosphate charges of the phosphodiesteric backbone. Therefore, low-salt concentrations are destabilizing for duplexes, since the repulsion between the strands is not neutralized. A natural cause for the change in salt concentrations comes from the terrestrial hydrological cycle driven by the sun (Figure 1.1a)[12]. Water evaporates leaving the salts behind, and condenses as it cools down into droplets made of pure water that then coalesce and precipitate.

A similar water cycle can take place at the microscale, for example between the differentially heated surfaces of rock pores (Figure 1.1b). The water that evaporates at the warm side recondenses as dew droplets made of pure water on the colder side. The droplets fuse to each other by surface tension and then rainfall back into the bulk by gravity. This generates fluctuations in the concentration of salts, where droplets made of pure water continuously rainfall on top of a salt-rich bulk.

1.1 The water cycle at the microscale

We created a lab model of a heated rock pore at the millimeter scale. A small chamber (500 µm) was created between two surfaces, and was half-filled with a salt-rich solution. A temperature gradient was created by differentially heating one surface (sapphire) with rod resistors and the other (silicon) with a Peltier element. The microscope was pointed through the sapphire and focused on the silicon wall. The atmospheric pressure was reduced down to 0.2 bar, by means of a vacuum pump, in order to imitate the lower barometric pressure of the Hadean Earth or higher altitudes[13,14]. The lower pressure increased the speed of the evaporation-condensation-raindrop cycles[15]. The time required for a single droplet

to nucleate, grow and rainfall was reduced from 66 ± 31 seconds down to 17 ± 10 seconds at 0.2 bar.

The temperature gradient drove the microscale water cycles, which have been imaged by bright field and fluorescence microscopy (Figure 1.1c-d). Condensation droplets of pure water could be seen growing and fusing above the gas-water interface. They then continuously fell down as raindrops and diluted the salts and DNA in the bulk.
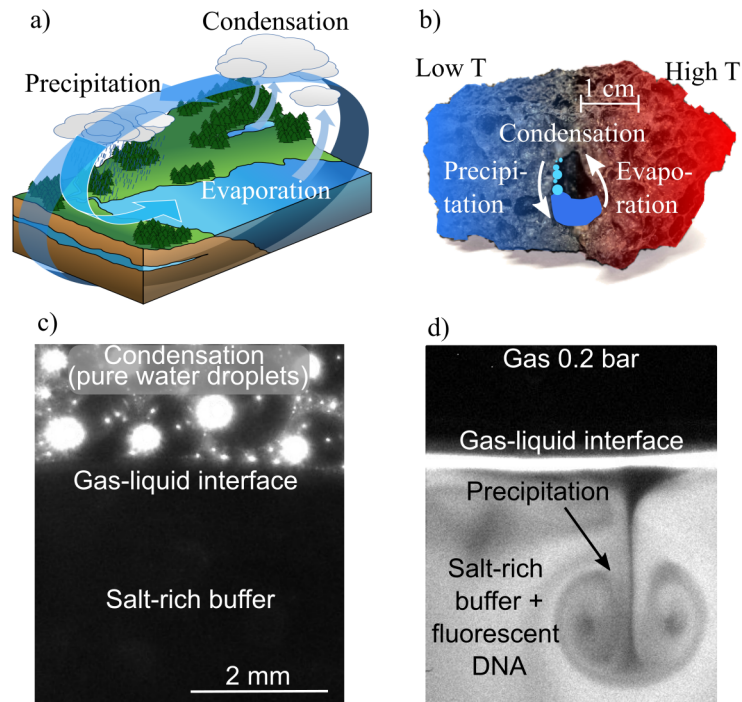

Figure 1.1: *The water cycle is a natural cause for oscillations of salts. It occurs at global scale driven by the sun (a) or within heated rock pores (b) containing gas and water. c) Bright field image of droplets of condensation water growing and fusing on the cold wall. d) Fluorescence image (DNA fluorescence) of a raindrop diluting the bulk.*

1.2   Oligonucleotides melting by salt oscillations

We used FRET (Förster Resonance Energy Transfer) to measure the fraction of double stranded DNA (or RNA) during the microscale water cycle by fluorescence microscopy[16]. The two complementary strands were centrally labeled with different fluorophores (FAM carboxy-fluorescein, and ROX carboxy-rhodamine) able to perform FRET when the oligonucleotide was in the duplex conformation[17]. As DNA probe, a DNA of 51 nt has been utilized. As expected, its melting temperature (T_m) was a function of the salt concentration of the bulk (NaCl). It could be modulated from 88 to 11 °C by [Na$^+$] from 500 to 0 mM,

respectively (Figure 1.2a).

The experiment in the microfluidic chamber was performed using a solution of 50 mM NaCl at pH 7.5 (with 10 mM Tris and 1 mM EDTA). Under these conditions, the DNA showed a T_m of 67 °C. The walls of the chamber were differentially heated at 67 and 55 °C. The raindrops induced continuos dilution of the salts, leading to periodic DNA denaturation in the proximity of the gas-water interface (Figure 1.2b-c). Upon their rainfall, they left a trace of low-FRET that slowly recovered to the initial value when the salt back-diffused there. These denaturation-reannealing cycles last around 10 - 30 seconds and were seen happening numerous times during the course of each experiment.
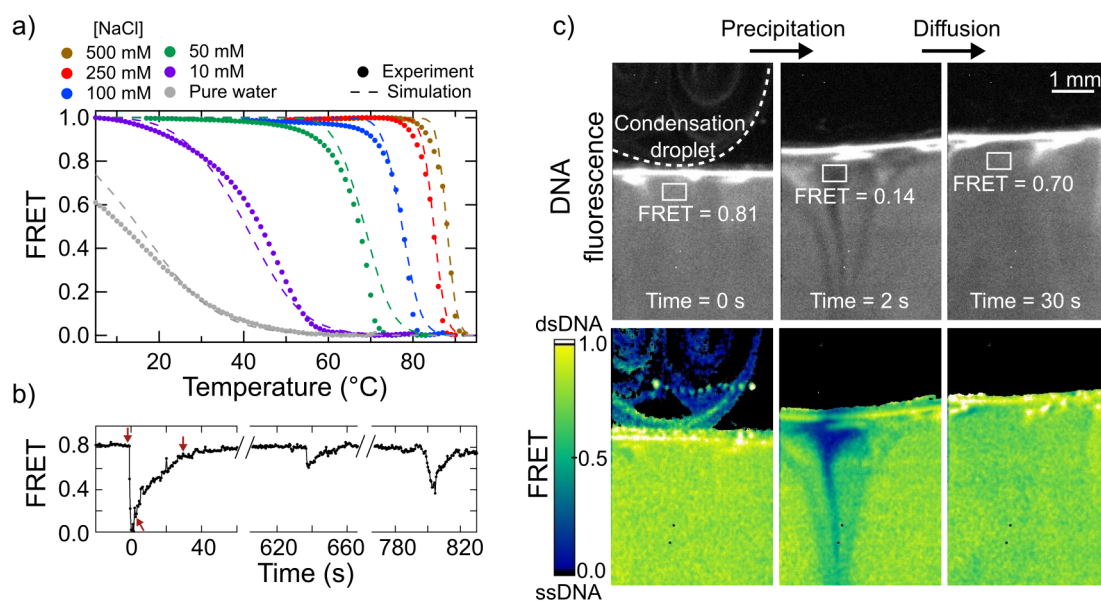
Figure 1.2: *Salts oscillations induced by raindrops denature oligonucleotides. a) DNA melting temperature is determined by the concentration of Na^+. b) Raindrops regularly fall on the bulk and dilute salts, inducing the melting of oligonucleotides. c) Images of the microscale water cycle measured by fluorescence (top) and DNA FRET (bottom). The raindrop leaves a trace of DNA melting (i.e. low DNA FRET).*

Similar results were observed in a vast range of experimental parameters (Table 1.1): DNA or RNA sequences of 24 - 51 nt, salinity of 50 - 500 mM, average temperatures between 20 - 61 °C and ΔT between 9 - 15 °C.

Oligo type	NaCl (mM)	T_m (°C)	<T> (°C)	ΔT (°C)	Initial <FRET>	Water cycle <FRET>	τ (s)
DNA 51 nt	50	67	61	12	0.81	0.14	10 ± 4
DNA 51 nt	150	82	61	12	1.00	0.21	3 ± 1
RNA 51 nt	150	88	61	12	1.00	0.41	8 ± 4
DNA 24 nt	500	43	20	9	0.98	0.21	14 ± 12
RNA 24 nt	500	45	38	15	0.76	0.29	3 ± 1

Table 1.1: The water cycle melts oligonucleotides in a wide range of salinity and temperatures, up to 20 K below the melting temperature. ΔT indicates the temperature differences of the chamber walls. τ indicates the time constant for strand reannealing.

In the microscale water cycle, the continous and slow rainfall of pure water droplets on top of the high salts bulk created a halocline at the microscale. This was particular evident when the concentration of NaCl was increased to 500 mM, since the density of water is determined by its salt concentration[18]. For example, seawater is approximately 28 kg m^{-3} denser than freshwater[19]. These density differences slow down mixing[20] and can lead to the formation of a vertical salinity gradient within a body of water, called halocline. The condensation freshwater that fell on top of the seawater-like bulk (500 mM NaCl) in fact did not mix. Over time, it created a vertical gradient in salts that translated into a vertical FRET gradient, with melted oligonucleotides at the gas-water interface and oligomer duplexes down in the bulk (Figure 1.3).
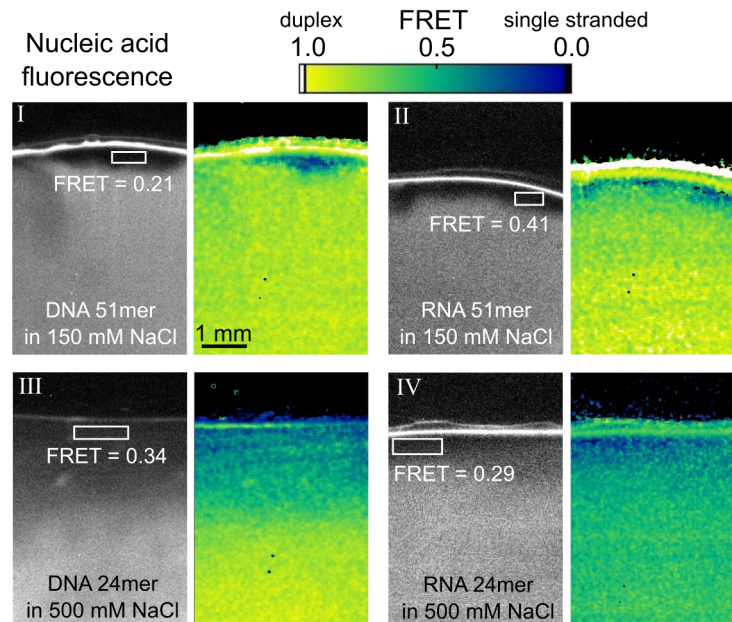
Figure 1.3: *A microscale halocline generates a persistent vertical gradient of DNA and RNA FRET. It was particularly evident in the experiments using a seawater-like solution (500 mM NaCl).*

1.3   Longer DNA accumulate at the gas-water interface

Differentially heated gas-water interfaces present numerous non-equilibrium forces. The continous evaporation at the warm side generates a capillary flow directed towards the warm side[21], the so-called coffee ring effect. Coupled to the bulk convective flow[22], DNA and RNA molecules are directed and accumulate at the gas-water interface at the warm side (Figure 1.4a-c). Oligonucleotides can up-concentrate up to 10000 fold. The effect was visible for the gas-water interface of the bulk, as well as the one of the condensation droplets shaped as a capillary bridge, as we will see in the next chapter.

The accumulation is balanced out by the back-diffusion of molecules from the concentrated area. Due to their heavier molecular weight and size, longer oligonucleotides have a lower diffusion coefficent. Therefore, they accumulate stronger than shorter oligomers (Figure 1.4d).
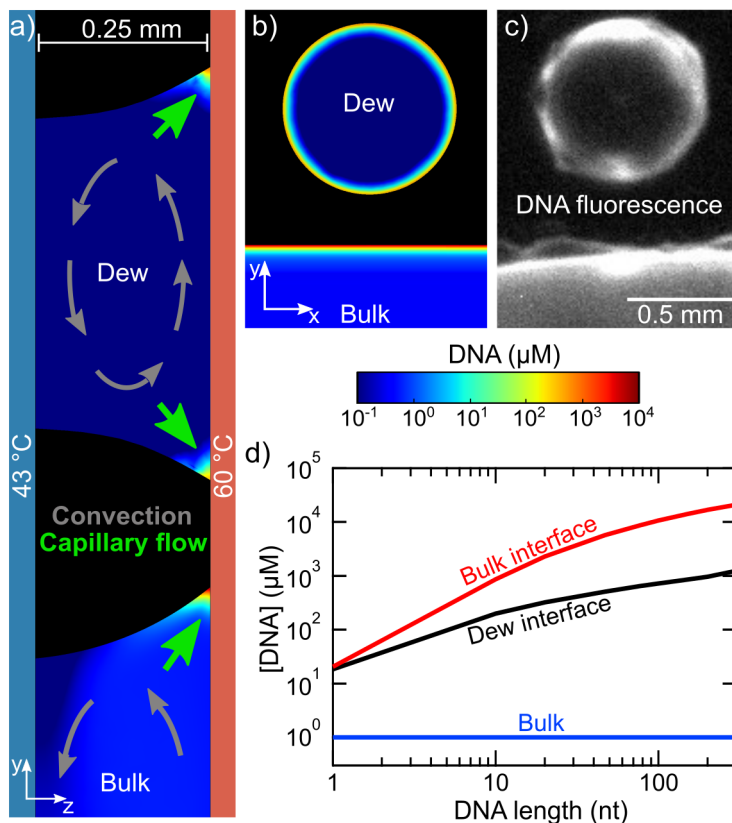
Figure 1.4: *DNA accumulates at the heated gas-water interfaces. Lateral (a) or frontal (b-c) view of the bulk (capillary meniscus) and condensation droplet (capillary bridge), here indicated as dew. As a consequence of the continuous coffee-ring effect, DNA accumulates at the contact line with the warm surface. d) Longer DNAs are preferentially accumulated, up to +10000 fold for sequences longer than 200 nt.*

This means that, given a pool of sequences of mixed lengths, the longer oligonucleotides will be preferentially selected and retained at the gas-liquid interface. This feature acts against the 'tyranny of the shortest', promoting the preferential up-concentration and survival of the longer DNAs.

1.4   Conclusions

The autonomous salt oscillations induced by the microscale water cycles in pores of rock denature double-stranded oligonucleotides under mild conditions, in a continuous and periodic manner. In our experiments, we estimated that 50% of the bulk volume is subjected to the salt dilutions every one hour.The findings provided here propose a primordial, one-pot method for the denaturation of oligonucleotides at cold temperature, eliminating the need of detrimental high temperature spikes that could damage chemical reagents and disintegrate the genetic information of the RNA world.

Moreover, the preferential accumulation of longer DNA strands retains the longer oligonucleotides, giving them a selective advantage. This phenomenon actively counteracts the 'tyranny of the shortest' sequences that would otherwise negatively stall early replication.

1.5   Methods

The microfluidic chamber

The microfluidic chamber that we used in our experiments (aka "thermal trap" or "dew chamber" or "chamber) consisted of a thin chamber (14 mm x 30 mm x 250-500 µm) made of Teflon and placed between a transparent sapphire window and a back plate made of silicon (which was eventually covered with a thin layer of Teflon to increase its hydrophobicity). The sapphire was held in place by a copper placeholder which contained rod resistors, while the silicon back plate was in contact with a Peltier element. The electric components could then be differentially heated to generate a controlled temperature gradient.

The sapphire window included four holes, where microfluidic tubings were attached. This allowed us to control the sample inflow and outflow to the chamber, to control the gaseous phase (by lowering its pressure by means of a vacuum pump or by inserting CO_2) and to measure the inner barometric pressure. A scheme and photo of the microfluidic chamber is shown in Figure 1.5.
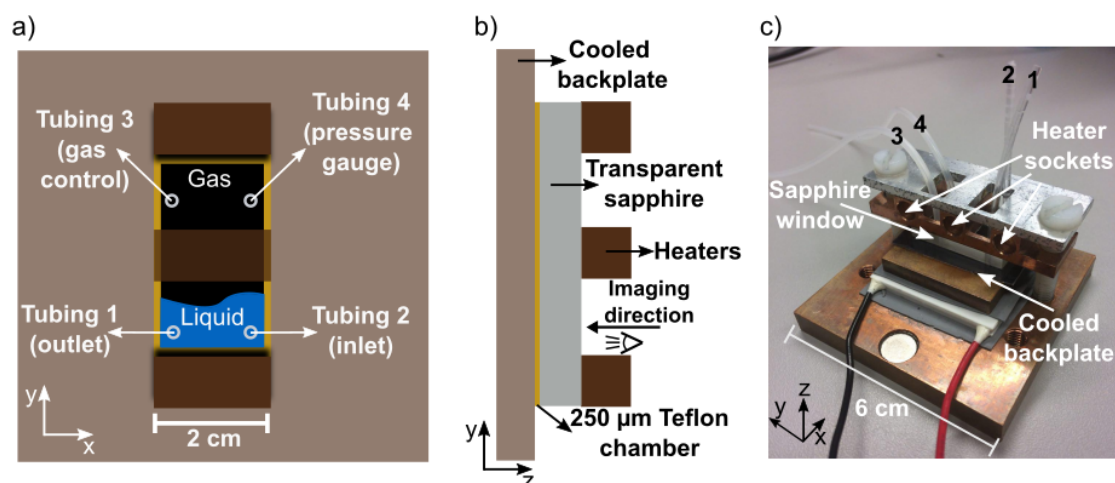

Figure 1.5: *Scheme and picture of the microfluidic chamber. Front (a), lateral (b) schemes of the chamber and a real photo (c). The rod resistors (heaters) are inserted into the three heater sockets within the copper placeholder, while the Peltier element lies below the silicon back plate.*

The imaging setup

The imaging setup consisted of a handmade standard fluorescence microscope (Zeiss Axiotech Vario) equipped with four excitation LEDs (M340L4, M385L2, M470L2, M590L2, from Thorlabs), excitation filters (BP 340/26, BP 379/34, BP 482/35, BP 588/20), beamsplitters (DC 475/40, DC 425 LP, DC 365 LP), a triple-edge dichroic mirror (DC 395/ 495/ 610), an Optosplit II with a ratiometric filter set (DC 600 LP, BP 536/40, BP 630/50), a Stingray-F145B ASG camera (ALLIED Vision Technologies GmbH) and a 1X objective (AC254-100-A-ML Achromatic Doublet). This set of filters and specifications allowed the real-time measurement of DNA FRET for a FAM-ROX pair, as well as the measurement of pH using the ratiometric fluorescent dye Lysosensor Yellow/Blue DND-160. Custom-made software was written with LabVIEW, in order to control the microscope's electronics and the electric components of the microfluidic chamber. A scheme of the whole setup is given in Figure 1.6.

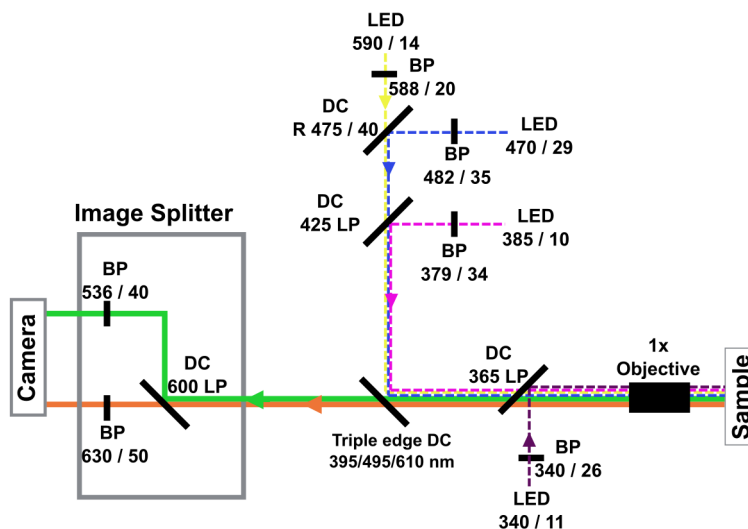***Figure 1.6:*** *Scheme of the setup for FRET and pH measurements. Four alternating LEDs have been used to excite FAM (blue LED), ROX (amber LED), and the two excitation maxima of Lysosensor (340 nm and 385 nm LEDs). Each LED was alternatively switched on for 100 ms. Therefore, the camera recorded four images per cycle. Together with the dead times, the camera frame rate was approximately 8 fps.*

Chapter 2

Hadean dew cycles drive DNA evolution

This chapter corresponds to the paper from Ianeselli *et al.* published in *Nature Physics* in March 2022 (attachment B).

We discovered that when the water cycle takes place in a confined geometry (i.e. a thin chamber ≤ 250 µm), it generates condensation droplets that rearrange as capillary bridges between the walls of the chamber. At this point, they can eventually re-dissolve the DNA or RNA that dried after the cofffee-ring effect. The droplets then start to evaporate and leave the oligonucleotides behind in the dry state (Figure 2.1). This phenomenon was a source of numerous wet-dry cycles.

We call this phenomenon 'dew cycle', in order to distinguish it from the previously described water cycle which consisted of salt dilutions by raindrops.
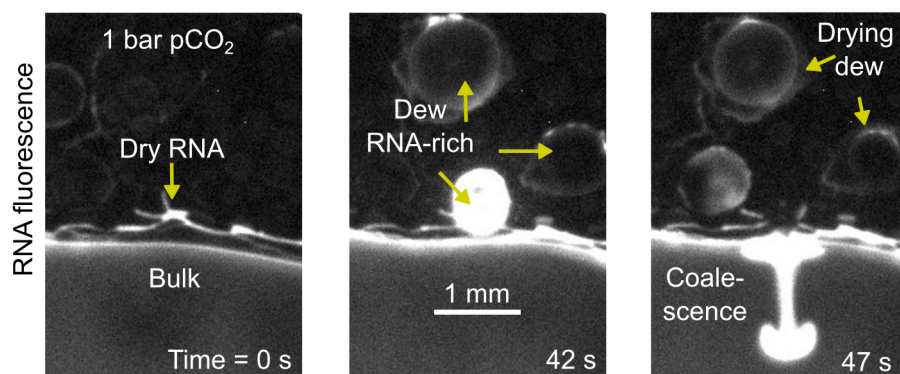

Figure 2.1: *The dew cycle generates salt, pH and wet-dry oscillations. RNA (or DNA) oligomers dry on the warm wall after the coffee-ring effect (left). Condensation droplets in a confined geometry dissolve and incorporate the oligonucleotides (center). The dew eventually coalesces with the bulk, re-transporting the RNA into it (right).*

2.1   Enhanced melting in the Hadean dew

We explored another possibility for what concerns the atmosphere of the early Earth: high concentration of gaseous CO_2 (0.1 - 1 bar)[23,24]. A CO_2-rich atmosphere has profound implications for the prebiotic chemistry. When gaseous carbon dioxide is dissolved into water, it forms carbonic acid, bicarbonate and carbonate, lowering the pH of water in a pCO_2-dependent manner[25]. Therefore, the surface waters of the early Earth likely had an acidic pH. The effect is particularly prominent for condensed water, due to the lack of salts (a pH of 4 is expected for pure water at 1 bar pCO_2).

In the microscale dew cycles under a Hadean CO_2 atmosphere, dew droplets acidify. They acidified down to pH 4, as measured by fluorescence microscopy using the pH-sensitive dye Lysosensor DND-160. The bulk instead maintained a quasi-neutral pH ($\sim$6), because of its high salts (10 mM $MgCl_2$ and TRIS) (Figure 2.2a). The salt content of the dew was estimated to be about 50 to 100-fold reduced (i.e. $\sim$0.1-0.5 mM Mg^{2+}), similar to rainwater[26]. Under these conditions, the duplex RNA fraction of a 24 nt dsRNA (T_m 66 °C) in the dew dropped to 14%, while remained close to 100% in the bulk, at temperatures 30 K below the bulk T_m (Figure 2.2b).
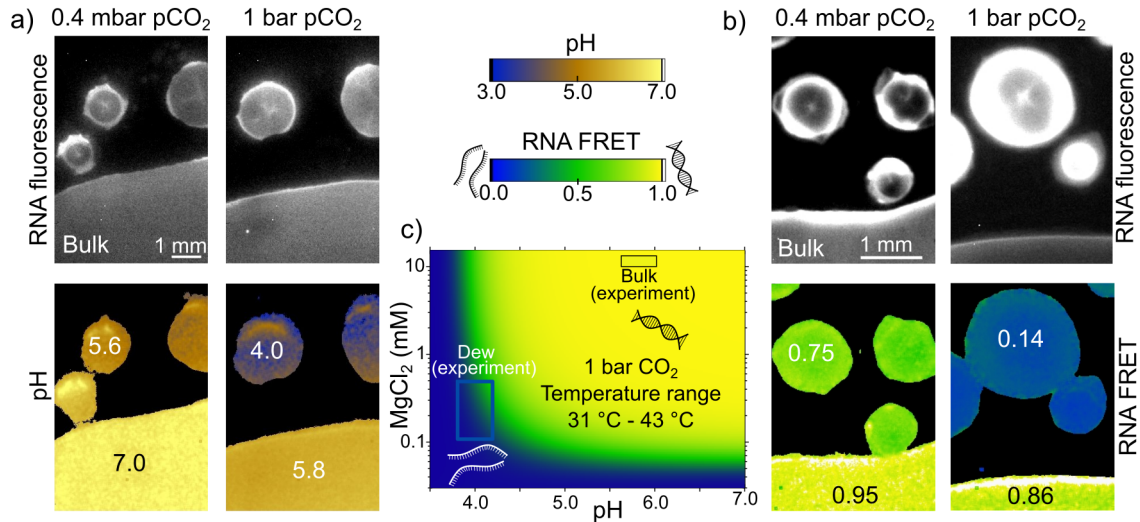
Figure 2.2: *The Hadean CO_2 atmosphere acidifies the dew droplets. a) PH drops after the absorption of CO_2 into pure water (i.e. dew), while it stays neutral in the buffered bulk. b) As a result, RNA efficently melts in the dew, but remains double-stranded in the bulk. c) A simulated RNA FRET landscape as a function of pH and salts showcases their synergistic effect on oligonucleotide stability.*

Bivalent ions, like Mg^{2+}, stabilize duplex oligonucleotides much more than monovalent ions (e.g. Na^+). The salt fluctuations alone (what we showed in the previous chapter) were not be able to remarkably denature dsRNA in the presence of high Mg^{2+} concentrations: they could only denature $\sim$25% of the total DNA. For enhanced melting, the synergistic effect of low salts and low pH in the dew was necessary (Figure 2.2c).

2.2 The Hadean dew cycles are a molecular replicator

The CO_2 dew chamber shows essential characteristics for a molecular replicator in the context of the RNA world:

- Enhanced melting of oligonucleotides in the dew at low temperatures. This maintains low hydrolysis rates to RNA while allows long RNA sequences to cyclically melt and re-anneal. In the bulk, the high salts promote prebiotic replication chemistries.

- Preferential accumulation of longer oligonucleotides at the evaporating gas-water interfaces. This feature gives an advantage to the longer strands, avoiding the detrimental kinetic race towards the shortest oligomers.

We mimicked the yet-to-be-discovered replication mechanisms of the RNA world, assuming they existed, by using a DNA replicating protein: the *Taq* polymerase. We used it to amplify a 51nt DNA template at 30 K below its bulk T_m. The replication reaction was monitored using SYBR Green I, which fluorescently stains DNA double strands, and showed the classical sigmoidal increase in fluorescence. Replication was possible only when the atmosphere was enriched in CO_2 (Figure 2.3a-b). Again, this means that the synergistic effect between low-salts and acidity induced by CO_2 was necessary to trigger substantial DNA melting to continue the replication cycles. Without CO_2 enrichment, the strands could not separate and replication stalled.
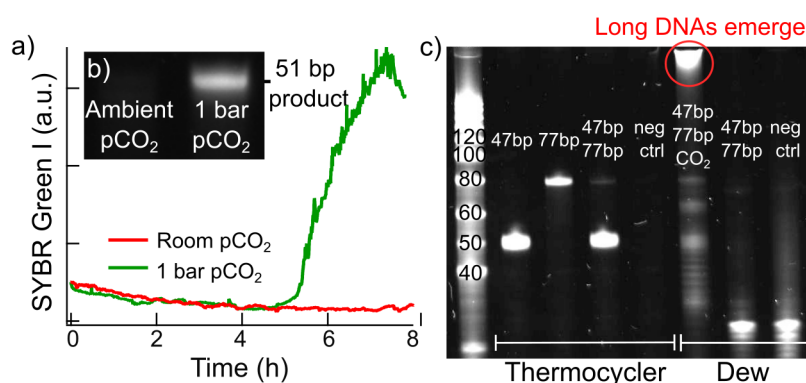
Figure 2.3: *The dew cycles allow DNA replication at $T \ll T_m$ and favor the longer strands. a-b) The synergistic combination of low salts and low pH induced by the Hadean CO_2 atmosphere provides DNA melting to continue the replication. Without CO_2 enrichment, replication stalls and the DNA template is not amplified. c) The CO_2 dew cycles avoid the 'tyranny of the shortest' and create new longer sequences by unspecific replication.*

When two DNA templates of different lengths (a 47 nt and a 77 nt) are replicated under equilibrium conditions (e.g. the standard thermocycling protocols), the shorter DNA sequence has a kinetic advantage and prevails over the longer one, which cannot be replicated and dies out (Figure 2.3c, 4th lane). This is the 'tyranny of the shortest' that we previously discussed.

However, when the replication reaction was performed in the non-equilibrium of the CO_2 dew chamber at T « T_m, not only could both DNA templates be replicated with comparable efficiency, but additional longer DNAs unexpectedly emerged. The length-selective features of DNA accumulation at the gas water interfaces promoted the survival and the replication of the longer strands. The longer DNA products only showed up in the dew chamber enriched of CO_2, indicating that they were formed as a consequence of the combination of enhanced melting + preferential accumulation of longer DNA strands. They were likely created during the DNA wet-dry cycles. The extremely high DNA and enzyme concentrations forced unspecific annealing and polymerization and led to elongation and shortening processes (as shown in Figure 2.4a), creating new mixed DNA sequences of increased complexity. But what are those long DNA products?

2.3   DNA sequences adapt to the dew

We sequenced the replication products using the Nanopore technique MinION, detecting 2856 reads with lengths between 140 - 1300 nt. They could be divided into two populations. One population in the length range of 140 - 300 nt, made of reads that contained numerous repetitions of primers and templates attached one after the other multiple times. The second population was made of reads between 300 - 1300 nt, which had a nucleotide composition rich in AT (AT fraction > 80 %), while the the primer/template repetitions were lost. But how is it possible that their nucleotide composition is so rich towards AT (> 80 %)? To obtain such a composition bias in the immense sequence space of long oligonucleotides is entropically very unfavorable. The answer lies in the adaptation of the sequences to the melting conditions of the dew cycles.

The AT:GC fraction is a determinant for the stability of DNA duplexes[27]. We therefore plotted the reads according to their AT and CG counts (Figure 2.4b-c). The background of the figure corresponds to the duplex DNA fraction (i.e. DNA FRET) under the conditions of the CO_2 dew. The long, AT rich reads follow a region of low DNA FRET (0.14 ± 0.12). No reads are found in the yellow area to the right or at the very left blue extreme of the map.
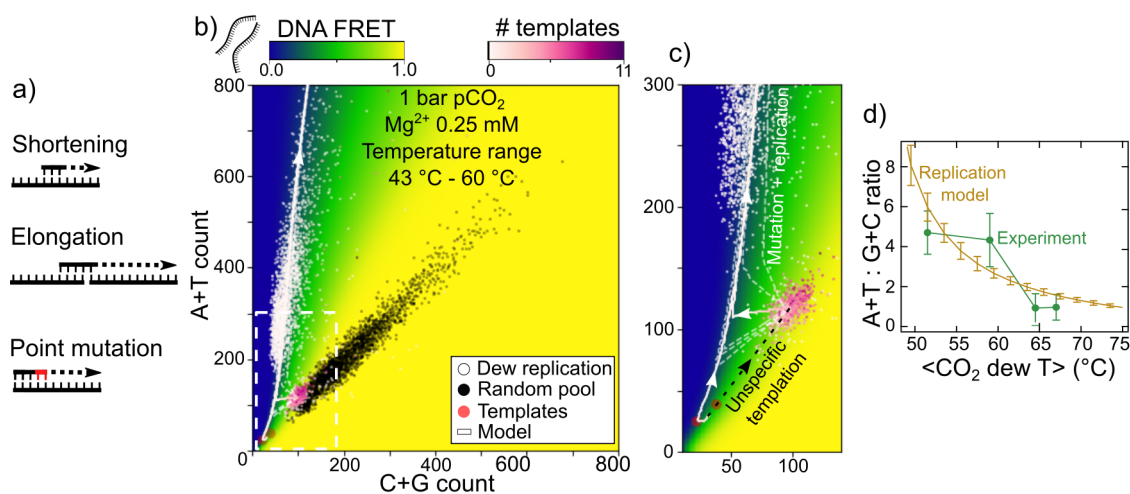
Figure 2.4: *The dew cycles drive DNA evolution. a) Unspecific polymerization reactions such as shortenings, elongations and mutations, that were triggered by the DNA wet-dry cycles. b-c) DNA replicate and evolve following a region of intermediate stability (i.e. low DNA FRET), elongating towards long strands enriched in AT. d) The denaturing conditions of the dew can be tuned to modulate the final AT:GC fraction of the replicated pool. For example, stronger denaturing conditions (e.g. higher temperatures) drive the evolution of strands that are richer in CG.*

This results indicate that the sequences with a low stability, which are more prone to undergo multiple cycles of denaturation and reannealing, are the ones preferentially replicated. DNA sequences with a too high or too low melting temperature stall, since they struggle to be cyclically melted and to template. In this sense, the DNA FRET landscape of the CO_2 dew selects which sequences will be replicated and which ones will die out. As the sequence length grew, only those with a biased AT fraction ($\sim 80\%$) showed an adapt stability and survived.

The DNA stability landscape of the CO_2 dew determines the final ATGC composition of the evolved sequences, which is synergistically determined by its salt content (< 0.5 mM Mg^{2+}), its pH (< 4) and its temperature. At moderate temperatures, we observed the formation of long strands (up to 1300 nt) rich in AT. At higher temperatures (i.e. stronger denaturing conditions), the resulting strands were richer in GC (Figure 2.4d).

2.4 Conclusions

Given the necessary out-of-equilibrium conditions, which could be found in the Hadean CO_2 dew, we demonstrated that a molecular replicator of oligonucleotides can exist and is compatible with an RNA world: melting at low temperatures in the dew to maintain low hydrolysis rates; high salts in the bulk for the prebiotic replication chemistries and for the catalytic activity of RNAs. As a consequence of the DNA wet dry cycles and the DNA length-selective accumulation, the sequences recombined with increasing length and

complexity, overtaking the "tyranny of the shortest" dilemma and building new genetic information. In this primordial molecular replicator, the new DNA sequences adapted to the melting conditions of the environment, and evolved in a subpart of the sequence space towards a biased ATGC composition of reduced entropy.

Our results show an important missing link between the geophysics of the early Earth and the chemistry required for life to form. Early life would not be harbored inside the equilibrium of lipid vesicles, but rather in the non-equilibrium of the heated pores of volcanic rock, oscillating between condensation droplets of dew under intense wet-dry, pH and salt cycles.

2.5   Methods

Protocol for DNA replication in the dew chamber

For the replication reactions we used the Taq PCR Master Mix (QIAGEN), with primers fw and rv at 0.25 µM, SYBR Green I 2x, BSA 0.1 %, DNA template 0.5 nM. The protocol for the replication in the thermocycler was: initial heat activation 95 °C for 3 minutes, 25 cycles of 90 °C for 5 seconds, 40 °C for 15 seconds and 60 °C for 15 seconds, then 4 °C for storage. For the replication in the dew chamber, the same mixture was inserted after an initial activation step at 95 °C for 3 minutes. Then, the temperature gradient was applied and the gas phase was eventually enriched with 1 bar of CO_2. For the replication of the 51bp DNA, we used the following sequences (5' – 3'): template DNA 51 nt, TTA GCA GAG CGA GGT ATG TAG GCG GGA CGC TCA GTG AAA CGA AAA CTC ACG, primer forward TTA GCA GAG CGA GGT ATG TAG GCG G, primer reverse CGT GAG TTT TCG TTC CAC TGA GCG T. For the replication of the 47 nt DNA and 77 nt DNA, we used the following sequences (5' – 3'): template DNA 47 nt AGG AGG CGG ATA AAG TAG GAC CAC GGG AGT CAG GCA ACT ATG GAT GA, template DNA 77 nt TCA TCC ATA GTT GCG AGT GTA GAT ACG AGG GCT TAC CAG CGA GAC CCC AGT AAC CAA GTC TAC TTT ATC CGC CTC CT, primer forward TCA TCC ATA GTT GC, primer reverse AGG AGG CGG ATA AAG T.

To observe the replication products, the samples were run on a 12.5 % denaturing (50% urea) polyacrylamide gel, with acrylamide: bis-acrylamide ratio of 29:1, solidified with TEMED and APS (ammonium persulfate). The replicated DNA samples were mixed with the gel loading dye blue (BioLabs, final concentration 2x) and loaded onto the gel wells. The samples were run in an electrophoretic chamber at 50 V for 5 minutes (alignment step) followed by 300 V for 15-20 minutes. The gel was then taken out and stained with SYBR Gold in TBE 1x for 5 minutes, and then imaged at the ChemiDOC MP (Bio-Rad) imaging station.

Unspecific replication model

Starting from a defined sequence pool (e.g. the initial DNA templates), each individual sequence has a probability of being replicated based on their duplex fraction under the condition of the CO_2 dew (acidic pH and low salts), calculated through a Van´t Hoff model generated from experimental DNA melting curves. This introduced a selection pressure resulting in the preferential replication of sequences with intermediate stability (FRET 0.14 ± 0.12, as determined experimentally).The algorithm is shown in Figure 2.5.
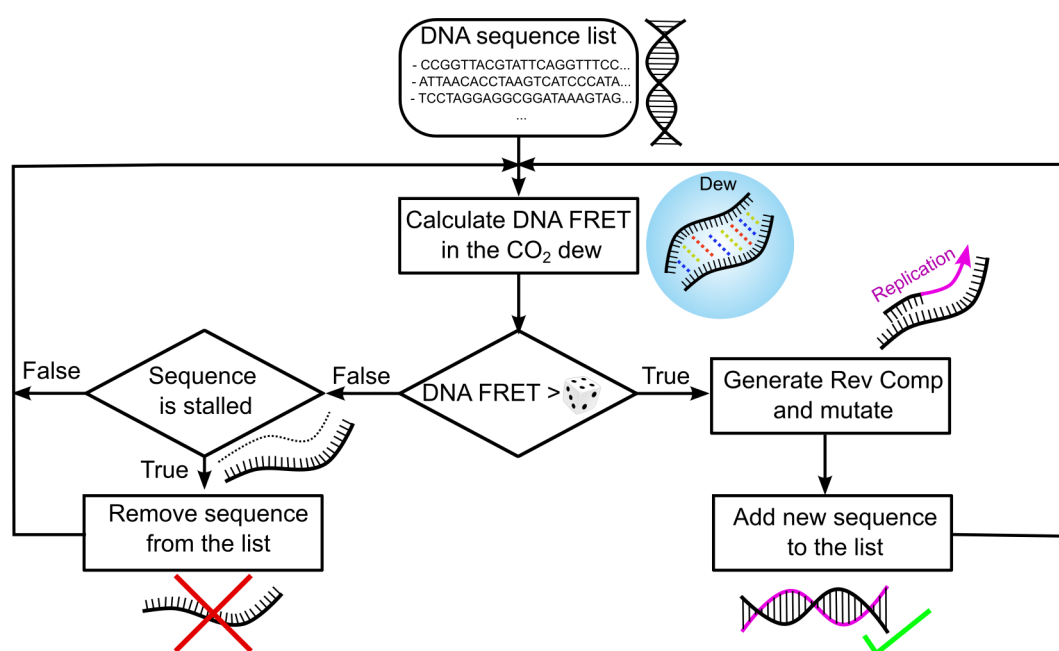

Figure 2.5: *Algorithm of the stochastic replication model.*

When a replication step is iniated, the reverse complement (RC) of the strand is created and a sequence modification takes place: it can whether be elongated or shortened, with a probability of *p* or *1-p*, respectively. The probability of being elongated (p) vs being shortened (1-p) was screened in Figure 2.4c (p from high to low: 1.0, 0.9, 0.84, 0.8, 0.7, 0.6), and yields results similar to the experiment for $1.0 \geq p > 0.5$. We modeled an elongation step as the insertion of a random subsequence of random length (between 0 and 15 nt, chosen uniformly) at a random position in the sequence. A shortening step was modeled as the deletion of a random part of the sequence of random length (again, between 0 and 15 nt, chosen uniformly). In reality. the insertion or deletion of nucleotides occurs via processes such as unspecific annealing, hairpin formation and other self-templating processes. Lastly, the mutation rate of the *Taq* polymerase was introduced (1e-4 mutations/nt).

Chapter 3

Protocells grow and divide inside microscale water cycles

This chapter corresponds to the paper from Ianeselli *et al.* published in *Nature Chemistry* in December 2021 (attachment C).

Compartmentalization is an essential feature in modern biology and it has been hypothesized to play a key role on early Earth during the origin of life, to localize molecules and facilitate chemical reactions[28, 29]. One primordial route to compartmentalization is coacervation[30]: a liquid-liquid phase separation of oppositely charged polyelectrolytes in aqueous solution, for example, poly-sugars, poly-peptides and oligonucleotides. Coacervate microdroplets are intriguing protocell models that exhibit interesting features for the prebiotic chemistries. They can localize and concentrate a broad range of molecules[31–33], enhance RNA catalysis[34, 35], promote the assembly of fatty acid bilayers[36], and support many types of catalytic reactions[37].

Coacervate protocells must also be able to evolve.

- Fusion processes are necessary for the exchange of molecules and genetic material[38]. Under standard conditions, the coacervate droplets tend to irreversibly coalesce and form a single bulky coacervate macrophase[39], which has a limited role as protocell.

- Division is essential to transfer evolutionary advantages to the succeding daughter protocells. To date, there has been no experimental realization of the fission of coacervate protocells, and what can drive it remains unclear.

Microscale water cycles present many physical non-equilbrium forces, such as convection, capillary and perturbative flows, that can induce the fusion, fission and fragmentation of coacervate protocells (Figure 3.1).
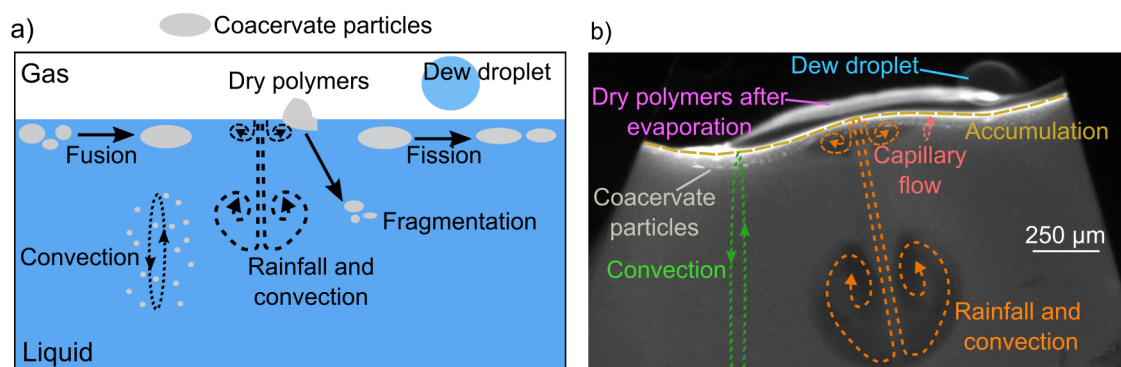
Figure 3.1: *Microscale water cycles perturb the coacervate microdroplets: scheme (a) and real photo (b). Convection transports the microdroplets at the gas-water interface. The capillary flow pushes them towards the warm side and makes them fuse. Perturbations induced by water raindrops promote fragmentation and stretching of coacervate droplets, triggering their division.*

3.1 Facilitated fusion at the gas bubble

A coacervate mixture of poly-sugars (CM-Dex, negatively charged) and positively charged electrolytes (PDDA, polydiallydimethylammonium), was inserted into the thermal chamber. It was half-filled in order to create a gas-water interface, similar to the chamber showed in the previous chapters. The microdroplets were observed by fluorescence microscopy, as 0.1 % of the coacervates has been doped with (fluorescein isothiocyanate) FITC-labeled CM-Dex.

Upon differential heating of the two sides of the trap (for example, warm side 49 °C, cold side 20 °C), the initially small droplets (< 15 µm) circulated in the bulk transported by convection (Figure 3.2a). Over time, they were transported at the gas-water interface, where they accumulated. Parallel movements and capillary flows made the microdroplets contact and fuse to each other. An individual fusion process between two coacervate droplets required a few seconds (from 1 to 10 seconds) and resulted in elliptically-shaped coacervates. The fusion process reached steady state after tens of minutes, up to a size of ~ 100 µm, depending on the coacervate mixture that has been used (Figure 3.2b-c).
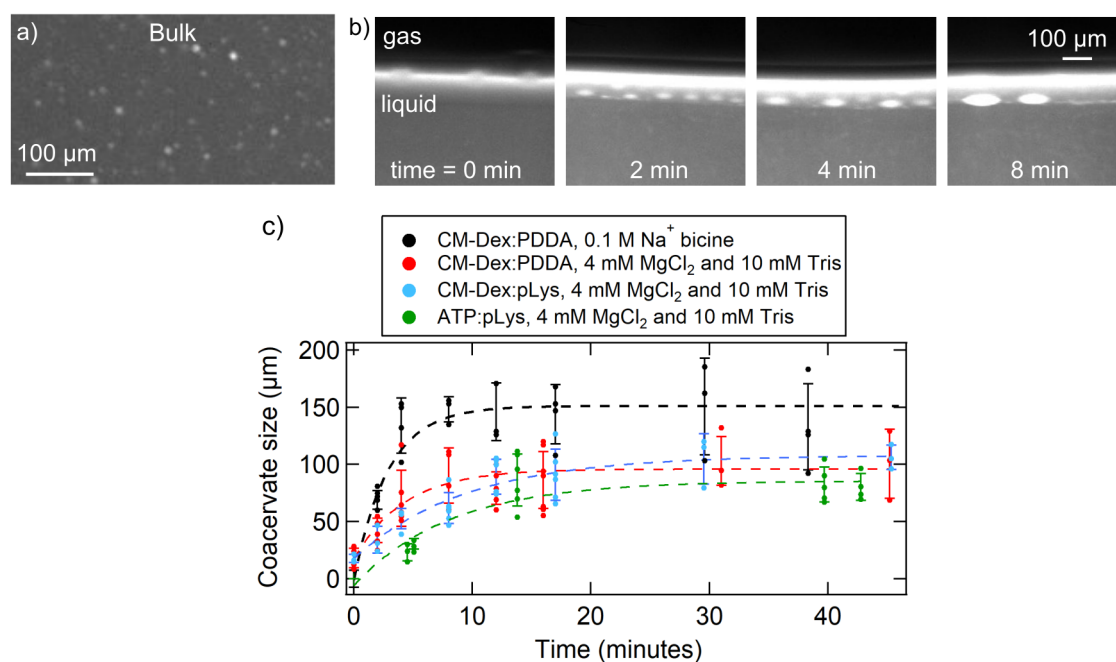
Figure 3.2: *Microdroplets accumulate at the gas-water interface and fuse to create larger droplets. The small droplets in the bulk (a) are transported by capillary flows at the gas-water interface and fuse over time, up to a size of 100 - 150 μm (b). The phenomenon is general for many coacervate mixtures.*

Between the different experiments, the variability between the droplets' size was large. This is attributed to the oscillatory salt fluctuations and flow perturbations induced by the microscale water cycle, as well as the intrinsic stochastic nature of droplet fusion. Even though salts are known to have a major impact on coacervation[40, 41], the salts oscillations in the thermal trap did not seem to adversely affect the stability of the droplets.

Moreover, the thermal trap avoided the sedimentation of the particles. Under isothermal conditions, 100 % of the particles would sediment at the bottom to form a single bulk coacervate macrophase. In the presence of a thermal gradient this was limited: the droplets were retained at the gas-water interface by capillary flows or kept in movement by the convection circulation in the bulk.

3.2 The water cycle promotes protocells' division

The coacervate droplets at the gas-water interface are subject to many forces that elongated and deformated them into an elliptical shape. An elliptical shape is associated with the initial stages of vesicle or droplet division[42], and was therefore possible that the coacervate droplets could undergo spontaneous division under the continuous forces and perturbations of the microfluidic water cycle. Indeed, we could observe spontaneous division events driven by two different mechanical forces:

- Division by stretching (Figure 3.3a). The opposing forces at the gas-water interface progressively stretched one coacervate droplet until it divided into two. The two daughter protocells then remained at the gas-water interface and eventually fused again.

- Division by fragmentation (Figure 3.3b). The rainfall of condensation water rehydrated the coacervates droplets that had dried on the warm wall, and induced strong perturbative fluxes that rapidly mixed and fragmented them. The fragments then started circulating into the bulk following the convection flow.
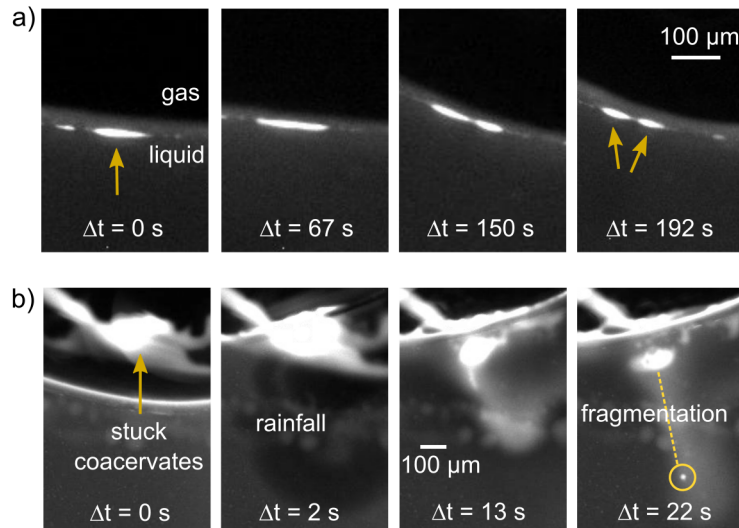

Figure 3.3: *Division of coacervate droplets in the water cycle. a) Opposing forces at the gas-water interface progressively stretch the droplet until it divides. b) The rainfalls create perturbative flows that rapidly mix and fragment coacervates.*

The fission events were only rarely observed. Out of a total of ~ 50 experiments, which explored many experimental parameters such as polymer types, concentrations, temperature gradients, buffers and trap geometries, we only observed 12 division events. Of which 10 of them corresponded to the type of division by fragmentation. In all cases however, the general properties of accumulation, fusion and division, wet-dry cycling were always observed. This provides a robust evidence that the phenomena that we observed could have taken place within the rocky environments of the early Earth, which had pores of different sizes subject to variable temperatures.

3.3 Coacervate phenotypes are separated by the gas bubble

RNA can be selectively enriched into the coacervate droplets, while the other coacervate components (e.g. CM-Dex and pLys) are known to enhance and regulate its catalysis[43]. But how does the non-equilibriun of the microscale water cycle influence the distribution of RNA in a multi-component coacervate system?

A dispersion of three components, CM-Dex, pLys and RNA, differentially labeled, was placed into the thermal pore and studied by multi-channel fluorescence. The fluorescence images showed that prior to the termal gradient, the droplets were enriched in RNA and pLys, with only a weak signal attributed to CM-Dex. Upon inducing a thermal gradient (for example, hot side 34 °C, cold side 15 °C), the droplets grew larger at the gas-water interface and were seen to be enriched in all three coacervate components (Figure 3.4a).
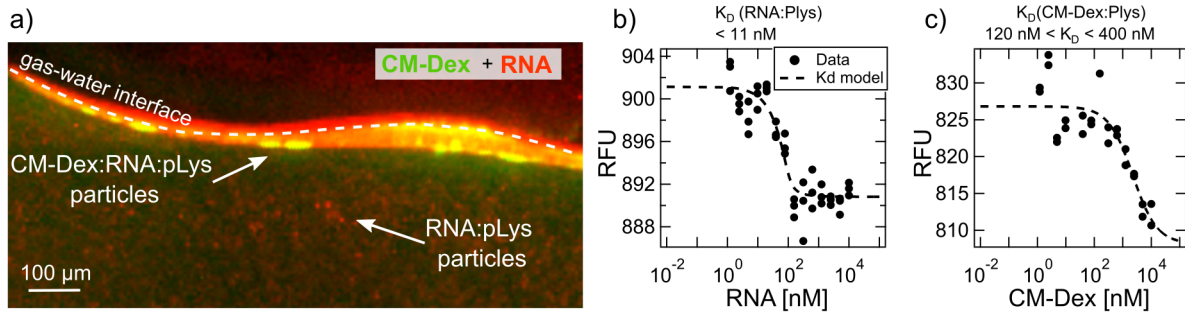

Figure 3.4: *The thermal trap creates and separates two populations of coacervate droplets. a) Large droplets enriched in all components (CM-Dex:RNA:pLys) grow at the gas-water interface, while K_D-driven smaller ones made of RNA:pLys form in the bulk. Thermophoresis measurements indicate that the RNA:pLys (b) has a smaller K_D (i.e. stronger affinity) than the CM-Dex:pLys system (c).*

This characteristic is likely a consequence of the different binding constants (K_D) between the cationic (pLys) and anionic (RNA and CM-Dex) species. Thermophoretic measurement to obtain the binding constants between RNA:pLys or CM-Dex:pLys revealed a higher affinity of RNA to pLys compared to CM-Dex. By fitting the dose-response curve (Figure 3.4b), we found a $K_D < 11$nM for the RNA:pLys complex, while 120 nM $<K_D<$ 400 nM for CM-Dex:pLys. The RNA:pLys complex has therefore higher affinity, likely due to the higher charge density of RNA. The strong accumulation at the gas-water interface could overcome the individual binding constants, and drove the growth of large coacervate droplets enriched in all the coacervate components. On the other hand, in the bulk the concentrations remained relatively low, and coacervation was driven by the individual K_D, preferentially forming RNA:pLys particles.

The thermal pore could generate and select for two different populations of coacervate droplets, with different chemical composition and phenotype. This would likely lead to different activities between the droplets. The ones at the gas-water interface would ben-

efit from additional variability and non-equilibrium properties: preferential enrichment of longer oligonucleotides; enhanced strand separation at lower temperatures; enhanced RNA catalysis induced by the presence of an additional polyanionic component.

3.4   Conclusions

Experimental primordial conditions - millimiter-sized rock pores in a temperature gradient - apply mechanical forces on coacervate droplets to drive their growth, division, and introduce chemical selectivity differentiating droplet phenotypes and genotypes.

The heated gas-water interfaces accumulate coacervate microdroplets and drive their fusion into larger droplets, while at the same time hindering their sedimentation and permitting their survival for indefinite time. The larger droplets were stretched by capillary forces and underwent division. Moreover, water precipitations induced rapid mixing and fragmentation of the coacervates. The primordial pore also had interesting effects on the chemistry of coacervation. Under equilibrium isothermal conditions the K_D is the major determinant for coacervation, favoring the stronger binders. By means of accumulation, the thermal trap instead is able to overcome the individual binding preferences and enhance the heterogeneity of the coacervate composition.

3.5   Methods

Preparation of the coacervate soutions

The coacervate components that we used in our experiments have been purchased by Sigma Adrich Germany: CM-Dex sodium salt (10-20 kDa or 150-300 kDa, monomer 191.3 g/mol), pLys hydrobromide (4-15 kDa or 150 kDa, monomer: 208.1 g/mol), PDDA chloride (8.5 kDa, monomer: 161.5 g/mol), FITC-labelled pLys (15-30 kDa), FITC-labeled CM-Dex (15 kDa or 150 kDa), ATP (507.2 g/mol). The stock solutions of each component were prepared to 1 M in milliQ-water and stored at -20 °C until use. RNA oligonucleotides were purchased from biomers.net Gmbh and dissolved to 100 µM in nuclease-free water. The sequence was (51 bases): 5´- UUA GCA GAG CGA GGU AUG T^{ROX}AG GCG GGA CGC UCA GUG GAA CGA AAA CUC ACG (ROX labeled).

The coacervate components were mixed together to the final concentration (2 to 20 mM) and immediately loaded into the microfluidic chamber: CM Dex:PDDA or CM-Dex:pLys or CM-Dex:pLys:RNA in either 0.1 M Na$^+$ Bicine buffer (pH 8.5) or 10 mM Tris and 4 mM MgCl$_2$ (pH 8.0).

Measurement of the binding constants

We measured the binding constant K_D of the RNA:pLys and of the CM-Dex:pLys complexes using a Nanotemper NT.115 Pico machine, which measures a binding dependent

fluorescence signal upon local heating with IR laser. To this end, we prepared serial dilutions of CM-Dex (15 kDa) or RNA (single stranded 51 nt) mixed together with a constant amount (20 nM) of FITC-labeled pLys (15-30 kDa). The CM-Dex and RNA concentrations were serially changed to span many orders of magnitude (from 0.1 nM to 1 µM). The solutions were inserted into thin glass capillaries and put on an aluminium holder, and then positioned inside the Nanotemper NT.115 Pico machine. Their fluorescence intensity was then measured over time upon a spike of the IR laser beam which locally heated the solution (more than 20 °C).

To calculate the K_D, the obtained data have been fitted with the following model:

$$f(Conc) = U + \frac{(B - U)(C + T_C + K_D - \sqrt{(Conc + T_C + K_D)^2 - 4 \cdot C \cdot T_C})}{2 \cdot T_C} \qquad (3.1)$$

where U and B indicate the fluorescence response values of the unbound (after IR heating) and bound (no IR heating) states, respectively. T_C (Target Concentration) corresponds to the concentration of the labeled species (pLys), and K_D corresponds to the binding constant. C (Concentration) indicates the concentration of CM-Dex or RNA.

Instead of estimating a single value for the binding constant, we estimated its likely range by means of the NRMSD (Normalized Root Mean Squared Deviation) between the data and the model. The NRMSD threshold was arbitrarily chosen to 15% in order to estimate the range. NRMSD was defined as:

$$NRMSD = \frac{RMSD}{RFU_{max} - RFU_{min}} \qquad (3.2)$$

where $RMSD$ corresponds to the root mean squared deviation of the data. $RFU_{\max}$ and $RFU_{\min}$ are the maximum and minimum values of the RFU data

Appendix A

Paper 1: Water raindrops denature RNA and DNA

Periodic Melting of Oligonucleotides by Oscillating Salt Concentrations Triggered by Microscale Water Cycles Inside Heated Rock Pores

Alan Ianeselli, Christof B. Mast, and Dieter Braun*

Abstract: *To understand the emergence of life, a better understanding of the physical chemistry of primordial non-equilibrium conditions is essential. Significant salt concentrations are required for the catalytic function of RNA. The separation of oligonucleotides into single strands is a difficult problem as the hydrolysis of RNA becomes a limiting factor at high temperatures. Salt concentrations modulate the melting of DNA or RNA, and its periodic modulation would enable melting and annealing cycles at low temperatures. In our experiments, a moderate temperature difference created a miniaturized water cycle, resulting in fluctuations in salt concentration, leading to melting of oligonucleotides at temperatures 20°C below the melting temperature. This would enable the reshuffling of duplex oligonucleotides, necessary for ligation chain replication. The findings suggest an autonomous route to overcome the strand-separation problem of non-enzymatic replication in early evolution.*

Introduction

The strand separation of oligonucleotides remains a major challenge for the continuous non-enzymatic genomic replication on the prebiotic Earth.[1] Without a simple means of DNA/RNA denaturation, the conversion of single strands to double strands by chemical replication leads to a dead-end. Moreover, the fast reannealing of separated strands can prevent template copying, since the timescale of reannealing can be orders of magnitude faster than the timescale of chemical replication.[2,3]

Salts like NaCl, KCl or MgCl$_2$ modulate the melting temperature of oligonucleotides over a wide range. By screening the interactions between the phosphate charges, ions have a direct role in stabilizing DNA or RNA double strands. Conversely, low salt concentrations have a significant destabilizing effect.[4,5]

A natural cause for the modulation of various salt concentrations comes from the terrestrial hydrological cycle powered by solar irradiation.[6] We found that at smaller

scales, for example in a porous rock, a microscale analogue of the water cycle is implemented by a moderate temperature difference (Figure 1 a,b). In our experiments, the evaporation on the warm side released salt-free water vapor into the gas void already at moderate temperatures. Instead of generating rain, snow or hail, we found submillimeter-sized water droplets that grew and precipitated at the colder side of the chamber. They fused by surface tension and gravitated stochastically into the original salt solution. This generated spikes of low salt concentration. In this setting, we studied the melting of DNA and RNA by fluorescence.

Results and Discussion

We reconstructed a heated rock pore on the millimeter scale (Figure 1 c,d). An applied temperature difference was used to drive the microscale water cycle, reconstructing a ubiquitous setting on the early Earth.[7] The salt-rich solution of NaCl and DNA evaporated pure water predominantly at the warm side. The condensation dynamics of water-vapor droplets on the cold side was imaged with both white light and fluorescence (Figure 1 e,f and Supporting Information, Movie 1). In the closed-pore setting, this process ran continuously with a stochastic characteristic.

The highly pure water droplets fell back into the bottom salt solution and were mixed into the bulk solution by surface tension, convection, and diffusion. This led to locally diluted salt and nucleic acid at the gas–liquid interface. Our experiments showed that they are sufficient for the denaturation of RNA or DNA well below their melting temperature.

Interestingly, the dynamics was found to slow down for higher salt concentrations due to the enhanced density difference between the lighter pure water and the denser bulk solution. This led to significantly slower mixing times and kept double-stranded oligonucleotides separated for longer times in a metastable salt gradient. Furthermore, the frequency of the salt oscillations was enhanced by reducing the ambient pressure in the experiments. This simulated possible barometric conditions on higher regions of the Early Earth[9,10] and was attributed to increased evaporation rates.[11]

We investigated the effect of the water cycle on the conformation of duplex DNA or RNA using Förster resonance energy transfer (FRET) under the alternating laser excitation (ALEX)[12] illumination protocol. Complementary strands were labeled with FRET-compatible probes: FAM (Carboxy-fluorescein) as the donor fluorophore and ROX

[*] A. Ianeselli, C. B. Mast, Prof. Dr. D. Braun
Systems Biophysics, Department of Physics,
Ludwig-Maximilians-Universität München,
Nanosystems Initiative Munich and Center for NanoScience
Amalienstraße 54, 80799 München (Germany)
E-mail: dieter.braun@lmu.de

Supporting information and the ORCID identification number(s) for
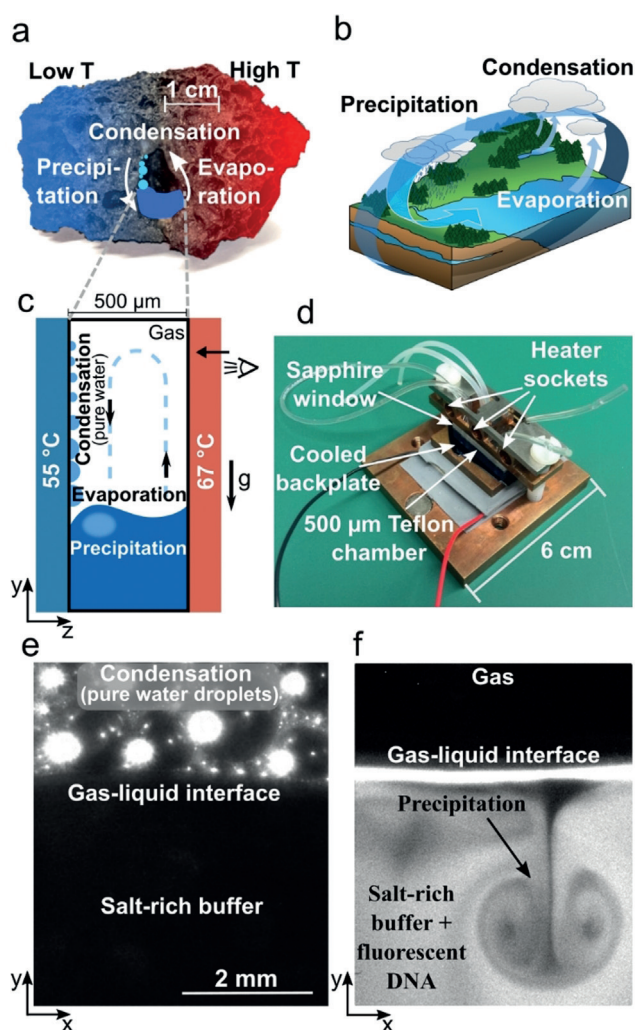the author(s) of this article can be found under:
https://doi.org/10.1002/anie.201907909.

a

Low T   High T

1 cm

Condensation

Precipi-   Evapo-
tation   ration

b

Condensation

Precipitation

Evaporation

c

500 μm

Gas

55 °C   67 °C

Condensation
(pure water)

Evaporation

Precipitation

y
z

g

d

Sapphire
window

Heater
sockets

Cooled
backplate

500 μm Teflon
chamber

6 cm

e

Condensation
(pure water droplets)

Gas-liquid interface

Salt-rich buffer

2 mm

y
x

f

Gas

Gas-liquid interface

Precipitation

Salt-rich
buffer +
fluorescent
DNA

y
x

Figure 1. Water cycle at the microscale. a) A microscale water cycle between water and gas is driven by a thermal gradient in a porous rock. b) The process can be compared to the global-scale hydrological cycle on Earth that is driven by solar radiation. c) Experimental geometry with the phase changes of water. A temperature difference between 67 °C and 55 °C is applied across a 500 μm gap that is filled with water and air. The black arrows indicate the direction of the microfluidic water cycle: water evaporates at the warm side, condenses into droplets at the cold side where they fall back into the water by gravity. d) Photo of the microfluidic setup. The temperature difference was created by a transparent, heated sapphire here shown on top of a cooled silicon back plate. The chamber volume (30 mm×14 mm) was cut out of a 500 μm thin spacer foil made from Teflon. e) A bright field image through the sapphire revealed the droplets of pure condensed water on the cold wall above the gas–water interface. The bottom remained dark. f) The fluorescence image showed the labeled DNA right after a condensed water droplet fell into the solution. The vortexes are created by diffusion and convection. Also seen is the characteristic accumulation of DNA at the gas–water interface caused by the evaporation dynamics studied recently.[8] At the top part, the condensed droplets are not seen since DNA did not evaporate in the water cycle.

(Carboxy-X-Rhodamine) as the acceptor fluorophore.[13] The two fluorescent dyes (FAM and ROX) were positioned on opposite strands (Supporting Information, Figure S2a).

Two excitation alternating light-emitting diodes (LEDs, blue and amber) were associated with an optical image splitter and provided access to the emission channels of FAM and ROX. By exciting the acceptor ROX, we measured the DNA concentration. The FRET intensity measured the separation of strands and was calculated from all three spectral images after correcting for the crosstalk between the channels. A detailed explanation of the FRET calculation and setup is given in the Section 2 of the Supporting Information. A high FRET occurred when oligonucleotides were double strands. When the oligonucleotides denatured and the strands separated, the FRET signal decreased.

FRET imaging was initially used to measure a melting curve in the water phase of the chamber (Figure 2a). The front and back plates of the chamber were heated simultaneously. This also allowed the calibration of the maximal and minimal FRET levels. We started with a 51mer (51 bp) dsDNA that revealed a melting temperature of $T_m \approx 67\,°C$ in 50 mm NaCl solution. The following experiments were performed at an average chamber temperature of 61 °C with a temperature difference between the warm and cold side of 12 °C. The mixing dynamics, which we will describe in the following, were imaged at the cold side where the condensation droplets are localized. There, the temperature was 55 °C, which is 12 °C lower than the melting temperature of the observed DNA.

As shown in Figure 2b and in Movie 2 in the Supporting Information, the falling of a microfluidic raindrop created a diluted area at the gas–water interface, where the FRET signal dropped from an initial value of 0.81 down to 0.14 and reannealed with a time constant of 16 s (Figure 2c). In the absence of a water cycle, a FRET value of 0.14 could be achieved only for a temperature greater than or equal to 71 °C (Figure 2a), indicating that the salt cycling was decreasing the DNA melting curve by 16 °C. As shown in the time traces of the FRET signal, averaged over the shown white rectangles (Figure 2c), this occurred periodically in our system and with different magnitude, depending on the size of the precipitating droplet.

The size of the condensation droplets could be estimated from low levels of fluorescence (Figure 2b, broken sphere). Especially later in the experiments, droplets revealed a small amount of DNA fluorescence. This could have been picked up from DNA that dried at the cold walls. It was likely deposited there when the water–air interface moved up and down, leaving traces of dried DNA at the moving interface. As seen in Figure 2b, the upward motion correlated with the enhanced water phase volume after dissolution of the droplet.

This remaining fluorescence in the condensation droplet also allowed us to calculate its internal FRET signal. We found a FRET < 0.2, reporting a continuously denatured DNA in its low salt condition. To speed up the droplet dynamics, the experiment was performed at reduced pressure ($P_{atm} = 0.2 \pm 0.1$ bar), as described later.

To understand the impact of salt on the hybridization of DNA, we determined melting curves with FRET for the aforementioned 51mer dsDNA for varying NaCl concentrations. By reducing the salt concentration, the T_m could be tuned widely from 88 °C down to 11 °C. It is therefore easy to
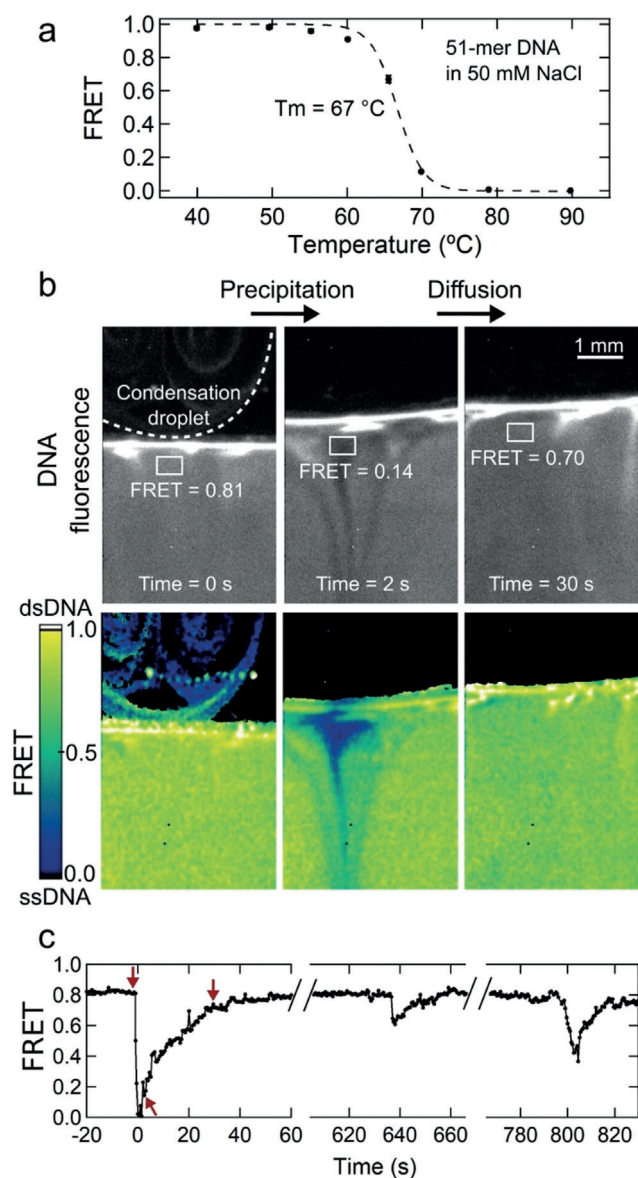
Figure 2. DNA denaturation at the gas–liquid interface by droplet precipitation. a) Melting curve of 51mer dsDNA in 50 mM NaCl measured by FRET inside the reaction chamber. The dashed line is a sigmoidal fit. b) Series of images showing the microfluidic precipitation of a pure water droplet at the gas–water interface. Top: DNA fluorescence (acceptor fluorescence), bottom: FRET signal. The white square indicates the region where the FRET signal was averaged. The uncertainty of the FRET signal was estimated to 0.08. c) Averaged FRET signal at the gas–water interface over time. Experimental conditions were: 50 mM NaCl, 10 mM Tris, 1 mM EDTA, pH 7.5, 5 μM DNA, temperature gradient of 12°C (hot and cold temperatures 67°C and 55°C, respectively), average $T = 61$°C, $P_{atm} = 0.2 \pm 0.1$ bar.

imagine how fluctuations in the concentration of solutes could impact the hybridization of oligonucleotides.

To provide an additional control, melting curves were measured in a standard thermocycler (Figure 3a and Supporting Information, Figure S4). Since here the oligonucleotide concentration remained constant, FRET could be monitored simpler by the fluorescence of the donor fluorophore. In the duplex form, the donor fluorescence is quenched
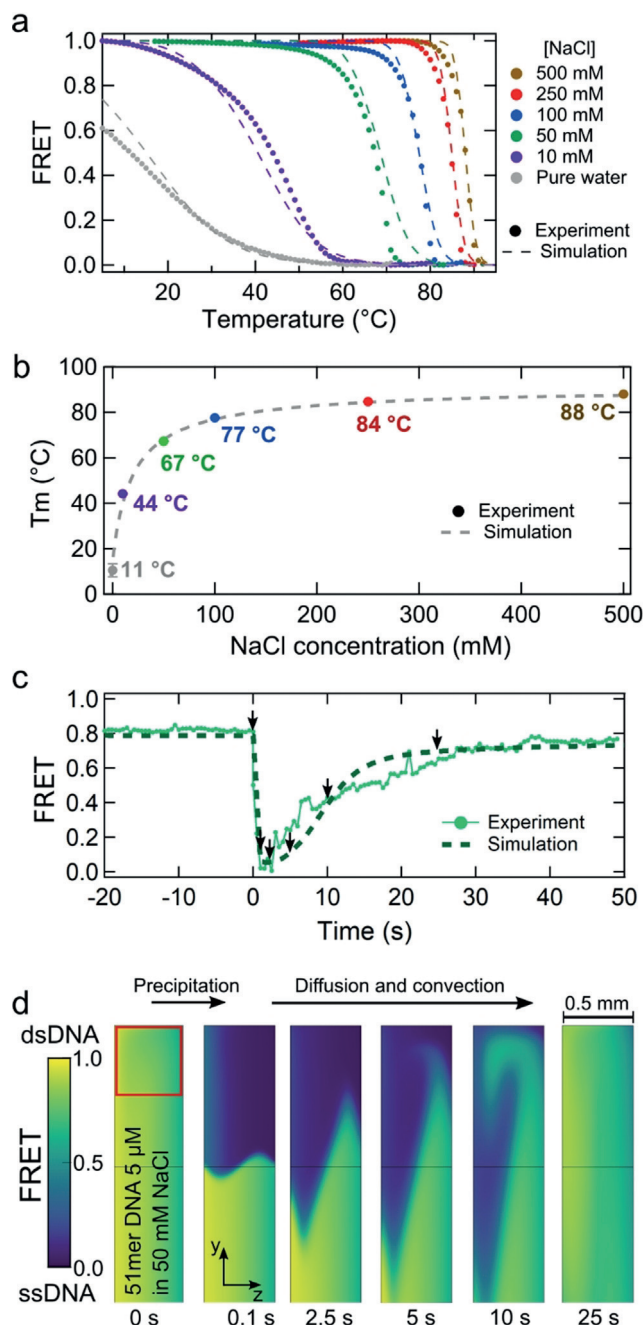

Figure 3. DNA melting by NaCl concentration variation. a) Denaturation curves of the 51mer DNA at different NaCl concentrations measured by FRET in the thermocycler. Buffer concentrations were: 10 mM Tris and 1 mM EDTA for 500, 250, 100, 50 mM NaCl with DNA at 5 μM. At 10 mM NaCl, we used 1 mM Tris and 0.1 mM EDTA. No salt buffer was used for the pure water condition (Milli-Q water). b) Melting temperature T_m versus NaCl concentration. Dashed lines are fitted curves using a hybridization model. c) An experimental FRET time trace was compared to a simulation of the droplet dissolution. d) Snapshots of the simulation at different times are shown, demonstrating how convection and diffusion leads to fast melting dynamics of the DNA. The full simulation is provided as Movie 3 in the Supporting Information.

by FRET, and increases when the two strands separate. As seen, the melting curves in the thermocycler confirmed the measurements inside the gradient chamber.

We obtained a deeper insight into the strand-separation dynamics by finite element simulations (COMSOL Multiphysics). The melting curves were used to fit the steady state of a salt-dependent kinetic hybridization model of DNA. On and off rates were calculated assuming a salt-independent and temperature-independent annealing rate (k_{on}) of 0.4 $\mu M^{-1} s^{-1}$ measured by hybridization experiments.[14] The strand separation rate (k_{off}) was calculated through the Van't Hoff relationship:

$$\ln K_{eq} = -\frac{\Delta H}{RT} + \frac{\Delta S}{R} \qquad (1)$$

where $K_{eq} = k_{on}/k_{off}$ and R is the gas constant. ΔH (the enthalpy change) and ΔS (the entropy change) have been estimated in function of NaCl concentration, based on the Van't Hoff plots (Supporting Information, Figure S5) obtained from the experimental melting curves of Figure 3a.

This reaction kinetics was inserted into the simulation as a diffusion equation of both complementary strands and subjected to the laminar convection flow of the water due to the temperature difference. For simplicity, details of the gas–water interface were not modeled. A precipitation event was simulated as a 2.5-fold dilution of solutes over a 0.5 mm² area at the top of the chamber, according to our experiments. We have modeled the water properties to account for the NaCl-dependence of the water density.[15] Details of the simulation are provided in Section 5 of the Supporting Information.

Figure 3c,d show the chamber in its cross-section. It is seen how the incoming droplet diluted the salts and melted the DNA. As the species are subsequently mixed by convection and diffusion, the strands slowly re-annealed. The simulation was in good agreement both in magnitude and recovery timescale with the experiments. This demonstrated how the speed of oligonucleotide hybridization and diffusion is fast enough to be affected by the salt concentration spike.

To probe the generality of the findings, we investigated the effects of the water cycle for double-stranded RNA and DNA of two different lengths (24 or 51 bp, termed 24mer and 51mer, respectively) and at various NaCl concentrations from 50 mM to 500 mM. Typical FRET signals are shown in Figure 4 with parameters collected in Table 1. This shows how a microscale water cycle could periodically melt oligonucleotides under various salt conditions. A peculiar, slower mixing was observed for the case of 500 mM NaCl, which we attributed to the enhanced density difference between the pure water droplet and the high salt concentration in the water phase
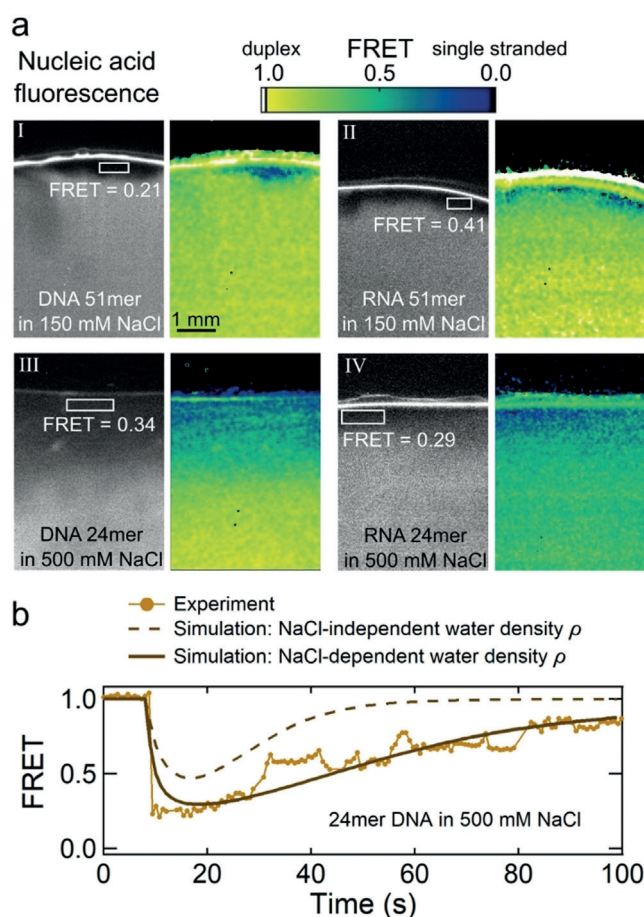

Figure 4. Investigation of different oligonucleotides and NaCl concentrations. a) Representative snapshots (DNA or RNA fluorescence and FRET) for various NaCl concentration, nucleic acid type, length, and temperatures. The roman numbers link to Table 1. White squares indicate the region where the FRET signal was averaged. If not otherwise reported, the buffer contained 10 mM Tris, 1 mM EDTA, at pH 7.5. Oligonucleotide concentration was 10 μM for I and II, 5 μM for III, and 2 μM for IV. Atmospheric pressure in all experiments was 0.2 bar to enhance the probability of observing spikes in the experiment. b) FRET time traces, simulations, and experiment. The NaCl dependency of water density (ρ) plays a significant role in our microfluidic denaturation system. This is confirmed by the agreement between our experiment (points) and the simulation (solid line). When the NaCl dependency of water density was not accounted (broken line), the reannealing time scale reduced and the agreement between simulation and experiment diminished. The conditions studied here correspond to the 24mer dsDNA, 5 μM in 500 mM NaCl (T_m 43°C) in the following temperature gradient: 15°C (cold side) and 24°C (warm side).

Table 1: Measurement parameters for experiments in Figure 2 and Figure 4 (roman numerals) such as oligonucleotide type, length, NaCl concentration, melting temperature T_m, the average chamber temperature $\langle T \rangle$ and the temperature difference ΔT. For each experiment, the average FRET signal in the water phase is reported as well as after the dissolution event of a droplet. The last column contains the time constant for reannealing.

ID		Oligo type	Length (bp)	[NaCl] [mM]	T_m [°C]	$\langle T \rangle$ [°C]	ΔT [°C]	Initial $\langle FRET \rangle$	Minimal $\langle FRET \rangle$	τ [s]
Figure 2b		DNA	51	50	67	61	12	0.81	0.14	10±4
	I	DNA	51	150	82	61	12	1.00	0.21	3±1
Figure 4a	II	RNA	51	150	88	61	12	1.00	0.41	8±4
	III	DNA	24	500	43	20	9	0.98	0.21	14±12
	IV	RNA	24	500	45	38	15	0.76	0.29	3±1

below. For example, seawater is on average 28 kg m^{-3} denser than freshwater,[16] leading to the thermohaline circulation between water masses that occurs in the ocean.[17] Due to the density difference, the lower FRET signal persisted significantly longer. Indeed, when the finite element model was fed with the salt-dependent density of water, it described this effect very clearly (Figure 4 b, dashed line). Additional details on the effects of the salinity gradient in our system can be found in the Section 6 of the Supporting Informatinon.

We studied the effects of atmospheric pressure on the dynamics of the microfluidic water cycle and compared the microscale water cycle between 1 bar and 0.2 bar in Figure 5.
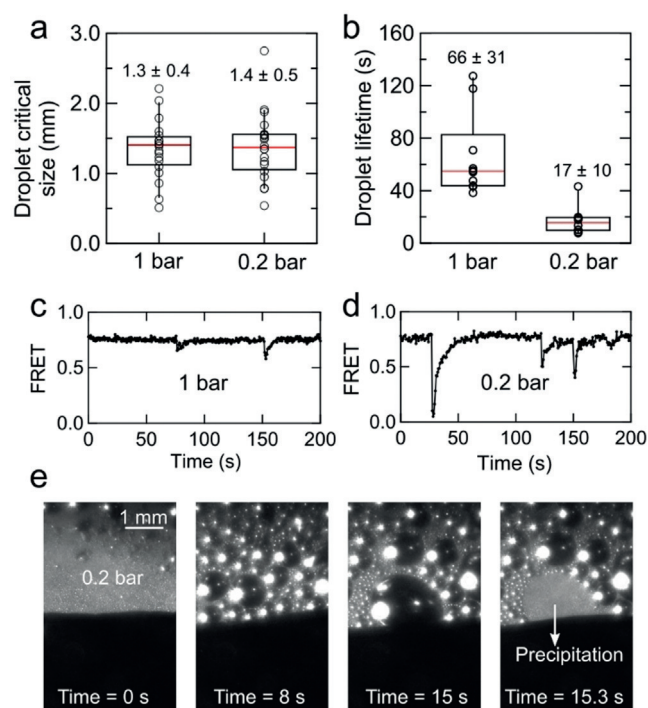

Figure 5. Faster water cycle at reduced pressure. Comparison of the critical droplet size (a) defined by the maximal size achievable by a condensation droplet before precipitation is observed. The lifetime (b) was measured by the time between a droplet nucleation and its precipitation into the water phase. Both (a) and (b) were measured at ambient pressure (1 bar) or 0.2 bar. c) and d) Kinetics of FRET over time at the gas–water interface over similar time span at ambient pressure (c) or 0.2 bar (d). Experimental conditions were: 50 mᴍ NaCl, 10 mᴍ Tris, 1 mᴍ EDTA, pH 7.5, DNA 5 μᴍ, a temperature gradient of 12 °C between 55 °C and 67 °C. e) Representative snapshots of the microscale water cycle at 0.2 bar. Condensation droplets were seen as shiny spheres above the gas–liquid interface. A comparison with ambient pressure is shown in Movie 4 in the Supporting Information.

The lower pressure did not significantly alter the average size of the condensing droplets (Figure 5 a). Rather, it increased their growth speed by a factor of about 4. This effect was exploited in our experiments before to obtain more frequent strand separation events. The statistics was obtained from analyzing white light movies shown in Figure 5 e.

Conclusion

Our study demonstrates autonomous salt oscillations denature double-stranded oligonucleotides under mild conditions. Microscale water cycles in pores of rock, subjected to a temperature difference are ubiquitous conditions to implement continuous salt oscillations. As water evaporates on the warm side continuously and drops back from precipitated pure water droplets, DNA at the water–air interface is molten periodically. Under these conditions, DNA (or RNA) denaturation was observed at temperatures well below the T_m of the initial solution. For the conditions of Figure 2, we estimated that about 50% of the water volume is subjected to the salt dilution per one hour of the experiment.

The finding is significant for the emergence of molecular evolution in the context of non-enzymatic chemical reactions for DNA or RNA. They often do not tolerate high temperatures due to hydrolysis, but require cyclic strand separation events for exponential replication. For example, ligation activated by EDC- or imidazole-activated polymerization reactions do not tolerate high temperatures[18,19] but at the same time require DNA or RNA strands to be separated to reshuffle the strands for the next replication cycle. Future experiments will focus on combining the setting with the possibility to perform non-enzymatic replication or ligation reactions at moderate temperatures, so that the separation of the DNA or RNA strands will not be induced by heat but will be provided by salt fluctuations at the gas–water interface.

Acknowledgements

Conflict of interest

The authors declare no conflict of interest.

[1] J. W. Szostak, *J. Syst. Chem.* **2012**, *3*, 2.
[2] R. Bruick, M. Koppitz, G. F. Joyce, L. E. Orgel, *Nucleic Acids Res.* **1997**, *25*, 1309–1310.
[3] R. Maggini, F. Secco, M. Venturini, H. Diebler, *J. Chem. Soc. Faraday Trans.* **1994**, *90*, 2359.

[4] C. Schildkraut, S. Lifson, *Biopolymers* **1965**, *3*, 195–208.

[5] D. W. Gruenwedel, C.-H. Hsu, *Biopolymers* **1969**, *7*, 557–570.

[6] R. H. Waring, S. W. Running, R. H. Waring, S. W. Running, *For. Ecosyst.* **2007**, 19–57.

[7] E. Agerschou, C. Mast, D. Braun, *Synlett* **2016**, *28*, 56–63.

[8] M. Morasch, J. Liu, C. F. Dirscherl, A. Ianeselli, A. Kühnlein, K. Le Vay, P. Schwintek, S. Islam, M. K. Corpinot, B. Scheu, D. B. Dingwell, P. Schwille, H. Mutschler, M. W. Powner, C. B. Mast, D. Braun, *Nat. Chem.* **2019**, 1.

[9] S. M. Som, R. Buick, J. W. Hagadorn, T. S. Blake, J. M. Perreault, J. P. Harnmeijer, D. C. Catling, *Nat. Geosci.* **2016**, *9*, 448–451.

[10] B. Marty, L. Zimmermann, M. Pujol, R. Burgess, P. Philippot, *Science* **2013**, *342*, 101–104.

[11] E. Özgür, K. Koçak, *Acta Geobalcanica* **2015**, *1*, 17–24.

[12] A. N. Kapanidis, N. K. Lee, T. A. Laurence, S. Doose, E. Margeat, S. Weiss, *Proc. Natl. Acad. Sci. USA* **2004**, *101*, 8936–8941.

[13] V. V. Didenko, *Biotechniques* **2001**, *31*, 1106–1116, 1118, 1120–1121.

[14] T. E. Ouldridge, P. Šulc, F. Romano, J. P. K. Doye, A. A. Louis, *Nucleic Acids Res.* **2013**, *41*, 8886–8895.

[15] F. J. Millero, A. Poisson, *Deep-Sea Res. Part A* **1981**, *28*, 625–629.

[16] D. M. Considine, *Van Nostrand's Scientific Encyclopedia*, Van Nostrand Reinhold, New York, **1989**.

[17] S. Rahmstorf, *Nature* **2003**, *421*, 699–699.

[18] O. Taran, O. Thoennessen, K. Achilles, G. von Kiedrowski, *J. Syst. Chem.* **2010**, *1*, 9.

[19] G. von Kiedrowski, *Angew. Chem. Int. Ed. Engl.* **1986**, *25*, 932–935; *Angew. Chem.* **1986**, *98*, 932–934.

Supporting Information

Periodic Melting of Oligonucleotides by Oscillating Salt Concentrations Triggered by Microscale Water Cycles Inside Heated Rock Pores

Alan Ianeselli, Christof B. Mast, and Dieter Braun*

anie_201907909_sm_miscellaneous_information.pdf

Content:

0. General experimental procedures

The experiments have been carried out in a microfluidic chamber (500 µm × 30 mm × 14 mm) made of Teflon, put on a silicon wafer and then placed between a transparent sapphire and a copper back plate. A temperature gradient was then produced by differentially heating the sapphire with rod resistors, and the silicon back plate with a Peltier element. We applied a temperature gradient ranging from 9 to 15 °C between the warm and the cold side. The average temperature inside of the chamber has been estimated through calibrations with temperature-sensitive dyes or through numerical calculations based on measurements of the outside temperatures. The software LabVIEW was used to create a PID loop and control the output voltage to the heaters and to the Peltier, in order to maintain a constant and precise target temperature. The input temperatures were provided with temperature sensors. Microfluidic tubings were connected to the chamber and provided the possibility to control the inflows, outflows, and the inner barometric pressure. The fluorescent microscope pointed toward the transparent sapphire. A detailed scheme of the microfluidic setup is shown in the supporting information, section 3.

The FRET setup consisted of a standard fluorescence microscope (Zeiss Axiotech Vario microscope) equipped with two LEDs (M470L2, M590L2, Thorlabs), excitation filters (BP 482/35, BP 588/20), a dualband beamsplitter (DC 505-606 T), an Optosplit II with a ratiometric filter set (LP DC 600, BP 536/40, BP 630/50), a Stingray-F145B ASG camera (ALLIED Vision Technologies Gmbh) and a 1X objective (AC254-100-A-ML Achromatic Doublet). The software LabVIEW was used to control the camera and the output voltage to the LEDs. A cartoon scheme of the setup is shown in figure S2b.

The chamber was filled with 30µl of solution which corresponded to ~1/4 of the total volume of the chamber. The remaining volume remained empty to leave enough space for evaporation, condensation and precipitation processes to occur. We applied a final pressure of ~0.2 (± 0.1 bar) with a vacuum pump (TRIVAC D 2.5 E, Leybold Gmbh) through microfluidic tubings. A handmade pressure regulator was placed on the tubing that connected the vacuum pump to the chamber, allowing for an accurate control of the final pressure. A manometer was attached to the chamber through another microfluidic tubing. A valve controlled the air flux between the vacuum pump and the chamber. This valve consisted of a microscope stage connected to a motor (TDC001 T-Cube DC Servo Motor Controller), which was used to physically press the tubing and close it. The cyclic opening and closing of the valve allowed to maintain a constant pressure inside of the chamber and, at the same time, limit unwanted sample uptake by the vacuum pump. The software LabVIEW was used to cyclically control the movement of the motorized stage, opening the valve for 10s every 30s.

DNA oligonucleotides were purchased from biomers.net Gmbh, with HPLC purification. The sequences were as follows. For the 51bp DNA: strand 1 TTA GCA GAG CGA GGT ATG T^{FAM}AG GCG GGA CGC TCA GTG GAA CGA AAA CTC ACG, strand 2 CGT GAG TTT TCG TTC CAC TGA GCG TCC CGC CT^{ROX}A CAT ACC TCG CTC TGC TAA. For the 24bp DNA: strand 1 TTT ATT ATT TTA T^{FAM}AT TAT TTA TTT, strand 2 AAA TAA ATA ATA T^{ROX}AA AAT AAT AAA. The 24mer or 51mer RNAs that we used have the same sequence of the corresponding DNA of the same length. The two labeled complementary strands were diluted from the stock solution (100 µM in nuclease-free water) and mixed together to a final concentration of 2-10 µM in salt-rich buffer (Tris 1-10 mM, EDTA 0.1-1 mM, NaCl 10-500 mM, pH 7.5). To favor the annealing of the two complementary strands, prior to every experiment the solution has been heated and slowly cooled down from 95°C to 4°C (ramp rate -1°C/10s) in a standard thermocycler (Bio-Rad CFX96 Real-Time System). The annealing process was monitored by measuring the emission intensity of the donor fluorophore. The emission of the donor is quenched by FRET when the two DNA complementary strands anneal.

1. Determination of the reannealing time constant τ

The reannealing process has been assumed to follow an exponential growth of the form[1]:

$$N(t) = a - b \cdot e^{-\lambda t}$$

where $N(t)$ is the FRET efficiency (i.e. duplex fraction) at time t, a and b account for the initial and plateau values, and λ corresponds to the growth rate, which is directly related to the reannealing time constant τ:

$$\tau = -\frac{1}{\lambda}$$

τ corresponds to the time at which the FRET value is at ~63% of its steady state level. Figure S1 shows a representative FRET experiment obtained from our microfluidic experiment (black dots) together with the exponential growth fit (red dashed line).
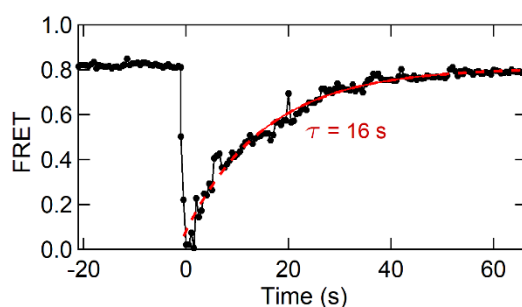

Figure S1. Determination of τ. Representative example of the calculation of the time constant. The experiment depicted here is a condition of 5 µM dsDNA (51 bp) in 50 mM NaCl, 10 mM Tris and 1 mM EDTA, average temperature 61 °C, temperature gradient of 12 °C (warm side 67 °C, cold side 55 °C), pressure 0.2 bar. The annotation entry indicates the reannealing time constant after the precipitation at time = 0 s.

2. Calculation of the FRET signal and setup details

The principle of the ALEX technique (Alternating Laser EXcitation)[2] has been applied to get a quantitative measurement of the separation between the two complementary DNA strands. The first LED excites the donor (FAM) directly and the acceptor (ROX) can be excited only if the two dyes are within the FRET range. The second LED excites the acceptor only. The spatial-averaged, temperature-dependent and crosstalk-corrected FRET signal is calculated as following[3]:

$$FRET(T) = \frac{DA(T) - dd(T) \cdot DD(T) - aa(T) \cdot AA(T)}{AA(T)}$$

where $aa(T)$ and $dd(T)$ correct for non-FRET associated signals in the DA channel and are defined as:

$$dd(T) = \frac{DA_D(T)}{DD_D(T)} \qquad aa(T) = \frac{DA_A(T)}{AA_A(T)}$$

All channels are defined according to table S1.

Channel	Excitation	Emission	Labelling
DA	FAM 470 nm	ROX 630 nm	FAM, ROX
DD	FAM 470 nm	FAM 536 nm	FAM, ROX
AA	ROX 590 nm	ROX 630 nm	FAM, ROX
AA$_A$	ROX 590 nm	ROX 630 nm	ROX
DD$_D$	FAM 470 nm	FAM 536 nm	FAM
DA$_D$	FAM 470 nm	ROX 630 nm	FAM
DA$_A$	FAM 470 nm	ROX 630 nm	ROX

Table S1: Definition of all used channels for the calculation of the FRET signal and the crosstalks. The letters N(M) denote the excitation (emission) wavelength. The index indicates which dyes are used (no index = both dyes are used). D = Donor (FAM), A = Acceptor (ROX).

Then, the coefficients α=min(FRET(T)) and β=max(FRET(T))-α are used to normalize the FRET signal between 1 and 0:

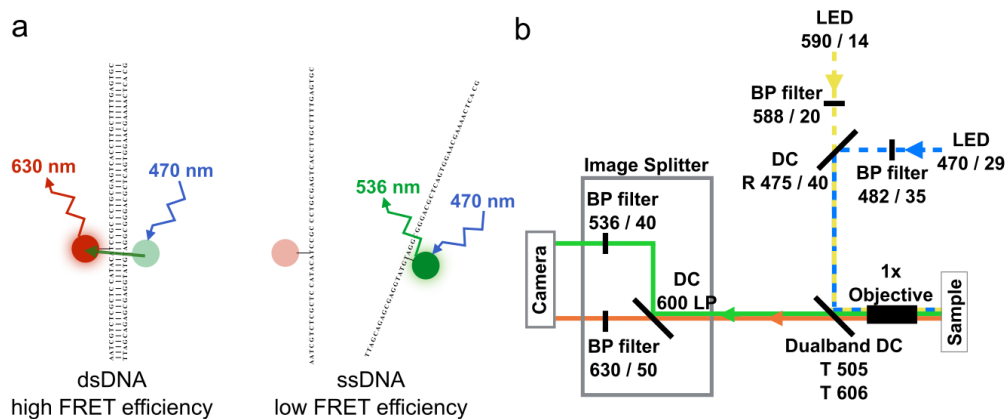$$FRET(T) = \frac{FRET(T) - \alpha}{\beta}$$

Figure S2. FRET schematics: a) Cartoon illustration of the labeled DNA, whose strands have been labeled with FAM and ROX. In the duplex form, the two DNA strands are in close proximity and the FRET signal is high. When the DNA denaturates and the two strands separate, the FRET signal decreases. b) Detailed scheme of our setup for FRET analysis. A standard fluorescence microscope has been equipped with two LEDs and an image splitter. Alternating illumination gives access to the emission channels of FAM and ROX.

3. Details of the microfluidic chamber

The experiments were run in a chamber (500 µm x 30 mm x 14 mm) made of Teflon which was placed between a transparent sapphire and a silicon back plate. A temperature gradient was produced by differentially heating the sapphire with rod resistors and the silicon back plate with a Peltier element. Microfluidic tubings were connected to the chamber and provided the possibility to control the inflows, outflows, and the inner barometric pressure. Our microfluidic chamber was formed by two parts (tubing numbering according to figure S3a, c):

-the *control chamber*, where the microfluidic tubing 1 was connected to the vacuum pump, tubing 2 to the analogical pressure gauge and tubing 3 communicated with the reaction chamber and was used as a pressure valve.

-the *reaction chamber*, where two microfluidic tubings (4 and 5) acted as inlet and outlet for the insertion and removal of the liquid sample, and the tubing 3 was connected to the control chamber.
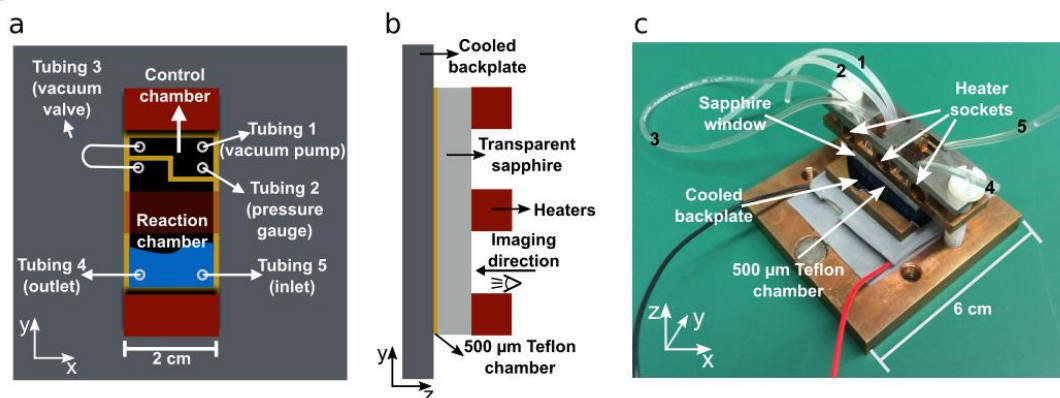

Figure S3. Scheme of the microfluidic chamber: a) and b) Cartoons showing the front view and the side view, respectively, of our microfluidic chamber. Imaging occurs through the transparent sapphire and photographs approximately one fourth of the reaction chamber. c) Photo of the microfluidic chamber.

A remote-controlled motorized stage was used as a valve acting on tubing 3, which was specifically opened at the desired time point to apply the low pressure inside the reaction chamber and closed right afterwards to limit sample loss due to evaporation and sample sucking from the vacuum pump. During the experiment, the vacuum valve was cyclically opened for 10 s every 30 s, in order to prevent excessive sample loss and, at the same time, maintain a constant P_{atm} inside the reaction chamber.

4. Variation of DNA 24-mer melting by NaCl variation

Melting temperatures for the 24mer DNA have been calculated in function of NaCl concentration, in a standard thermocycler by monitoring the fluorescence of the donor fluorophore, which is quenched by FRET when the nucleic acid is in the duplex form. The results show a high influence of NaCl on the stability of duplex DNA, as already observed for the 51mer DNA of figure 3. In the range between 500 mM NaCl and 50 mM, the melting temperature dropped from 43 °C to 18 °C. In pure water, the solution did not show a clear melting curve, as DNA probably became too unstable under such conditions.
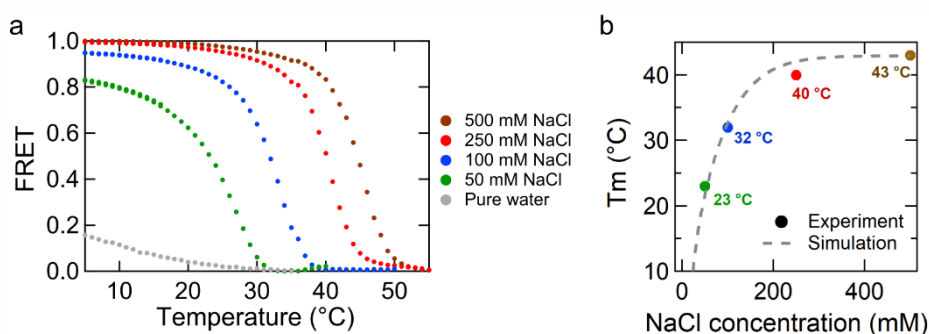

Figure S4. Melting curves of the 24mer DNA at different salt conditions: a) Denaturation curves at different NaCl concentrations, shown as FRET vs temperature. b) T_m vs NaCl concentration as determined from a). Buffer concentrations were 10 mM Tris and 1 mM EDTA for the conditions of 500, 250, 100 and 50 mM NaCl. The last condition corresponds to pure Milli-Q water.

5. Finite element simulation of DNA denaturation, transport and NaCl fluctuations

To gain deeper insights into the effects of a rain-like precipitation on the dynamics of DNA denaturation and transport, we performed finite element simulations with the software COMSOL Multiphysics®.

The temperature profile within the chamber has been calculated through partial differential equations for transient heat transfer, given the temperatures at the warm and cold sides (67 °C and 55 °C respectively), while insulating the top and the bottom of the chamber. The convectional flow profile has been calculated through Navier-Stokes equations for incompressible fluids. The resulting flow profile is superimposed by thermophoretic and diffusive movement of the molecules using PDEs. The overall molecular flux j is given by [4]:

$$j = \underbrace{-(D \cdot \nabla c)}_{Diffusion} - \underbrace{D \cdot S_T \cdot \nabla T \cdot c}_{Thermodiffusion} + \underbrace{\vec{v}\,(\alpha, w) \cdot c}_{Convection}$$

where D is the molecule's diffusion coefficient, S_T its Soret coefficient, c its concentration, T is the temperature, v is the convective flow profile, w is the width of the chamber and α corresponds to the angle between the chamber and the direction of gravity. The values for the diffusion coefficient of NaCl (D_{NaCl} = 1.6e-5 cm^2 s^{-1}) and its Soret coefficient ($S_{T\,NaCl}$ = 0.771e-3 °C^{-1}) have been taken from experimental measurements found in the literature[5,6]. The values for the diffusion coefficient of DNA (D_{DNA} = 105 µm^2 s^{-1}) and its Soret coefficient (S_T $_{DNA}$ = 0.106 °C^{-1}) have been calculated through fit of experimental data for a 51mer DNA[3].

Fluid properties have been corrected to take into account the density of water in function of salinity. We applied the international one-atmosphere equation of state of seawater[7], which relates water density (ρ) to salinity (S) and temperature:

$$\rho = \rho_0 + A\,S + B\,S^{1.5} + C\,S^2$$

where ρ_0 is the density of pure water (in units of kg m^{-3}), S is the salinity of the solution (in ppt) and A, B and C are parameters that take into account the temperature dependency of water density.

The DNA denaturation and annealing dynamics have been approximated by a first order reaction kinetics of the form:
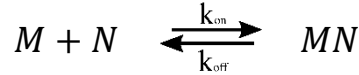
$$M + N \quad \underset{k_{off}}{\overset{k_{on}}{\rightleftharpoons}} \quad MN$$

where M and N corresponded to the single strand and its corresponding reverse complement, and MN indicated the double strand form. Differential equations have been solved as following:

$$\frac{d[M]}{dt} = -k_{on}[M][N] + k_{off}[MN]$$

$$\frac{d[N]}{dt} = -k_{on}[M][N] + k_{off}[MN]$$

$$\frac{d[MN]}{dt} = k_{on}[M][N] - k_{off}[MN]$$

The value of k_{on} = 0.4 µM^{-1} s^{-1} has been used as a temperature-independent and salt-independent constant, estimated from measurements of DNA hybridization kinetics[8]. The value of k_{off} has been calculated through the Van 't Hoff relationship:

$$\ln K_{eq} = -\frac{\Delta H}{RT} + \frac{\Delta S}{R}$$

where K_{eq} = k_{on}/k_{off}. -ΔH/R and ΔS/R have been derived from the Van 't Hoff plots obtained from the experimental melting curves of the 51mer DNA (figure 3a). The plots have been calculated at various NaCl concentrations, and the values of -ΔH/R and ΔS/R have then been fitted accordingly with an exponential function. In this way, we have been able to calculate temperature-dependent and salt-dependent k_{off} rates, given a constant k_{on}. Results are shown in figure S5.
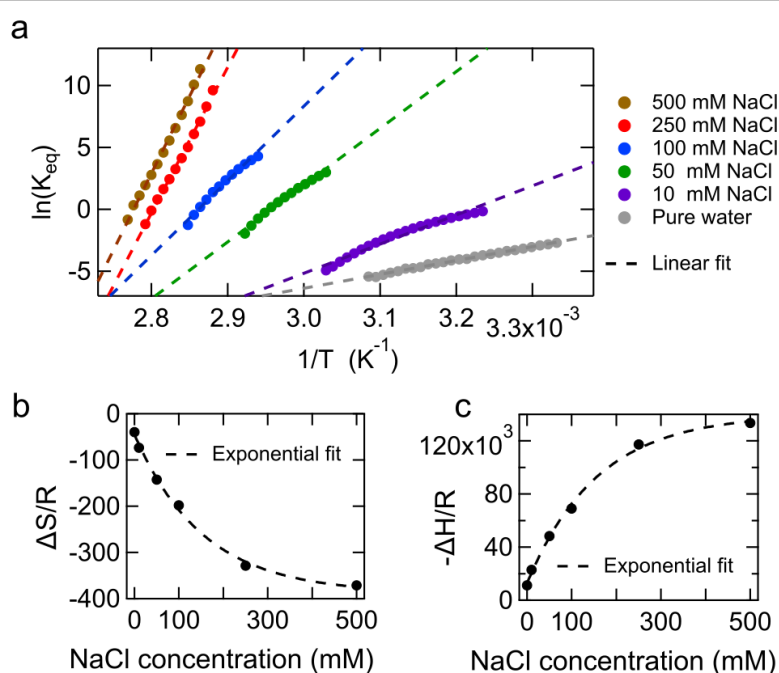
Figure S5. Determination of the NaCl dependency of ΔH and ΔS. a) Van 't Hoff plots for our 51mer DNA at various NaCl concentrations. The dashed lines indicate the linear fit. b) and c) Exponential fit of -ΔH/R and ΔS/R obtained from the Van 't Hoff plots. The fits obtained here have been used in the simulation to estimate the values of k_{off} in function of the temperature and salt concentration of the solution.

6. Investigation of a halocline by finite element simulation and experiments

A halocline, a vertical salinity gradient within a body of water, can have a significant influence on the convective-diffusive dynamics that occurs in our system, slowing down the mixing process between the species. When a droplet of condensing water falls on the top of the salt-rich solution, the water density difference due to the different salinity has been shown to create a layer of purified water floating on the salt-rich solution. In this section, we investigate the microscopic behavior of a halocline within a thermal gradient, and a static halocline under isothermal conditions.

We simulated a raindrop as a 10x fold dilution of a 1 mm^2 area at the top of a salt-rich solution containing 500 mM NaCl and 5 µM dsDNA (24mer). We applied a temperature gradient of 9 °C between the sides of the chamber (24 °C at the right left side, 15 °C at the left side). Figure S6.1 shows the pattern of the convection flow and NaCl concentration of the chamber. At t = 0 s (the initial equilibrium state), the convective laminar flow circularly transports the material throughout the whole chamber, with a speed up to 45 µm s^{-1}. After the precipitation, the halocline clearly disrupts the laminar flow between the compartments of different salinity. Therefore, the diluted species are not able to cross the salt gradient by convection, but they have to rely on their diffusion coefficient. The convective laminar flow induced by the temperature gradient is significantly faster than the mere diffusion of the species. For example, in our system, to travel a 1 mm distance, the convection flow only needs about 22 s. This is much faster than the mere diffusion of DNA and NaCl, which would need approximately 55 minutes and 5 minutes, respectively, to travel 1 mm. Therefore, we propose that the disruption of the convection flow induced by the halocline is the cause of the slow mixing that we observe.

The phenomenon can be understood in terms of buoyancy The laminar convective flow in our chamber arises from water compartmentalization, vertical gravitation and differential thermal expansion of the fluid induced by the temperature gradient across the sides of the chamber. The result is a circular motion of the water, which constantly transports the diluted species all around the chamber.

In the presence of a halocline, the difference in the water density due to different salinity is now greater than the difference in water density due to the temperature gradient. In the first tens of seconds after the precipitation, until NaCl diffusion is still very limited, this results in the formation of separated convection patterns in the compartments with different salinity. Later on, when NaCl diffusion slowly smooths out the salt gradient, the convection pattern at the top is fully disrupted. The phenomenon is reversible, and the convective flow is restored when the NaCl is homogenized by diffusion.

Though the gradient in NaCl concentration can persist for many minutes, this does not necessarily translate into a long-lasting DNA denaturation. As shown in figure S6.1c,d the DNA strands are able to reanneal before the salt concentration is fully restored. This is attributed to the fact that, at this average temperature, the 24mer DNA only needs a fraction of the total NaCl concentration to be fully stable as a duplex oligonucleotide.
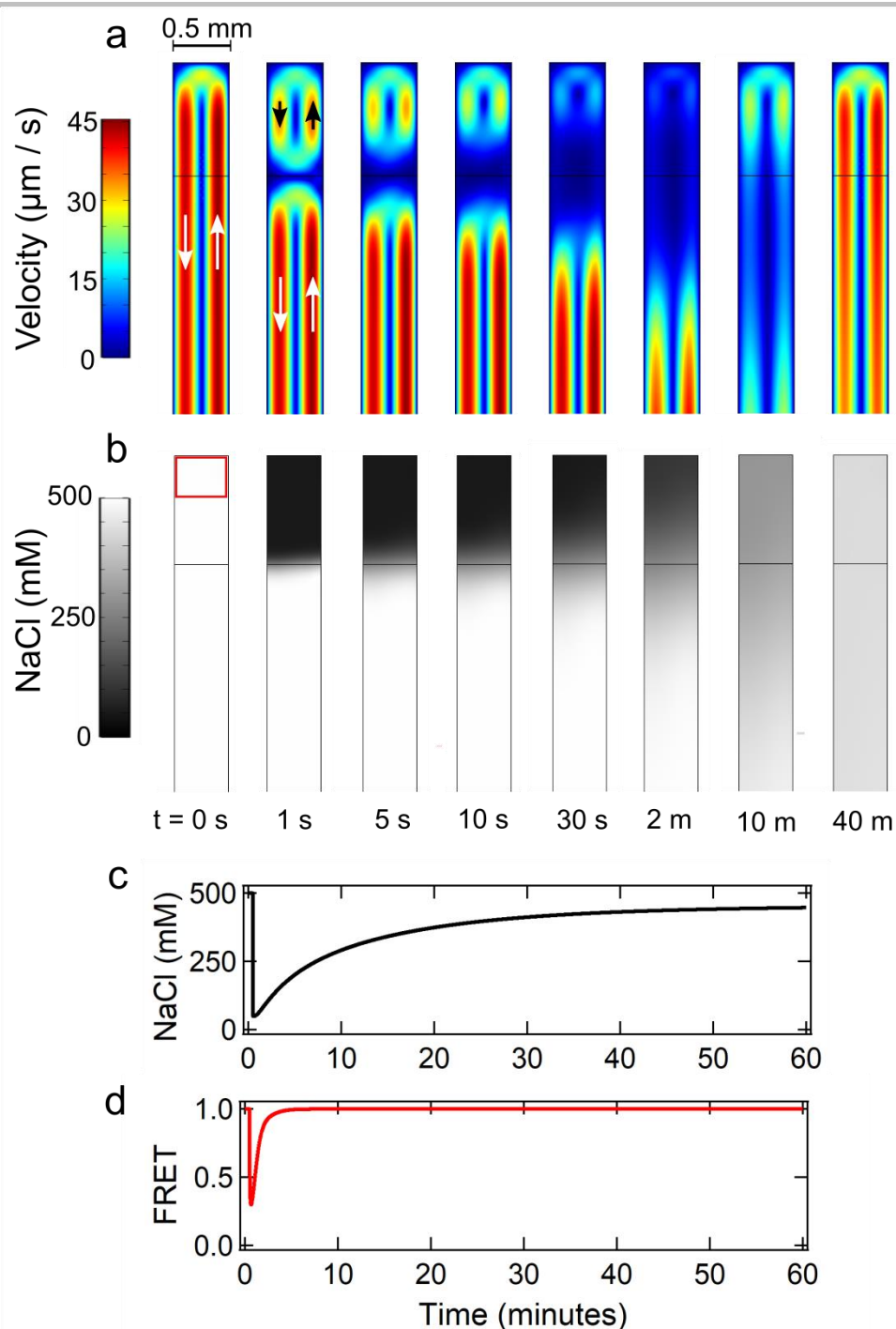
6

Figure S6.1 Convection and diffusion of the species in the presence of a halocline. a) Convection maps of the chamber in function of time. Time has been normalized such that t = 0 s corresponds to the moment right before the dilution event. The arrows indicate the direction of the convection flow. b) NaCl concentration maps in function of time. c) and d) Time trace of NaCl concentration and FRET, respectively. The values show the average signal corresponding to the red box shown in b).

We experimentally investigated the effects of a static halocline (no convection due to thermal gradient and no turbulence induced by precipitating droplets), on the diffusion of a 24mer DNA. To address this question, we used a small cuvette (1 mm of thickness, 10 mm of width), filled with 100 µl of solution containing 5 µM of FAM–labeled ssDNA, and 500 mM NaCl or pure MilliQ water. The experiment took place at room temperature (no temperature gradient) and room pressure. Then, we added 20 µl of pure MilliQ water directly on top of the solution, carefully to minimize the turbulence induced by the addition of the liquid, and we then monitored the fluorescence signal at the gas-water interface over time.

SUPPORTING INFORMATION

As shown in figure S6.2, in a halocline (blue line) the pure diffusion of DNA is significantly slowed down.
In the absence of the halocline (red line, i.e. when freshwater is added to the freshwater solution), the DNA homogeneously re-diffuses to half of its final concentration already after approximately 12 minutes of diffusion. On the other hand, in the presence of a halocline, the DNA takes much longer time to re-diffuse homogeneously at the air-water interface (the half value is reached after about 35 minutes).
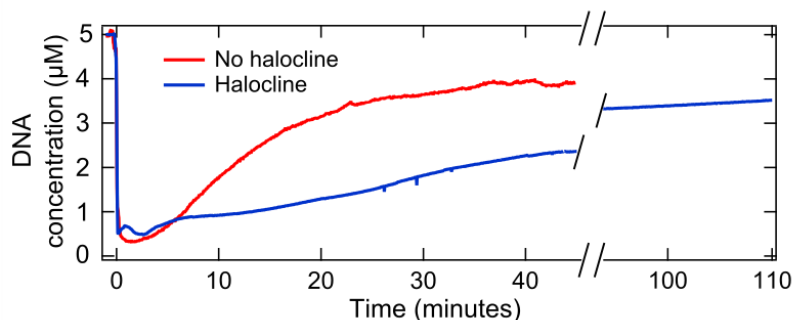

Figure S6.2 Diffusion of the species in a static halocline. DNA concentration over time at the air-water interface measured by fluorescence, in the presence (blue line) or absence (red line) of a halocline. Note that the final plateau value cannot reach 5 µM anymore, because the addition of pure water lowered the overall maximal concentration to 4.2 µM.

This experiment elucidates another aspect on how a halocline can influence the mixing times. Not only the convection, but also the diffusion of the DNA alone seems to be significantly impaired by a salinity gradient (diffusion resulted to be about 3 times slower in the presence of a salt gradient). The diffusion timescales observed in the static halocline experiment (figure S6.2) are longer than the ones observed in our microfluidic water cycle. First of all, in this experiment, the perturbations were reduced to the minimum by eliminating the thermal gradient (and therefore the precipitating droplets) and by adding the salt-free liquid very carefully. Second, the volume of the liquid added on top of the salt-rich solution was now much larger than the volume of a precipitating droplet (20µl against approximately 1µl), thus significantly increasing the necessary diffusion times.
Taken together, these observations help understanding the dynamics of the halocline present in our system, clarifying the reasons of the long mixing times between differentially salted waters that have been observed in our experiments and simulations.

7. List of movies

supplementary_movie_1_water_cycle.avi
supplementary_movie_2_denaturation.avi
supplementary_movie_3_simulation.avi
supplementary_movie_4_pressure_comparison.avi

8. References

[1]   A. Leike, *Eur. J. Phys.* **2002**, *23*, 21–26.
[2]   A. N. Kapanidis, N. K. Lee, T. A. Laurence, S. Doose, E. Margeat, S. Weiss, *Proc. Natl. Acad. Sci.* **2004**, *101*, 8936–8941.
[3]   C. B. Mast, S. Schink, U. Gerland, D. Braun, *Proc. Natl. Acad. Sci. U. S. A.* **2013**, *110*, 8030–5.
[4]   L. Keil, M. Hartmann, S. Lanzmich, D. Braun, *Phys. Chem. Chem. Phys.* **2016**, *18*, 20153–20159.
[5]   E. A. Guggenheim, *Trans. Faraday Soc.* **1954**, *50*, 1048.
[6]   D. R. Caldwell, S. A. Eide, *Deep Sea Res. Part A. Oceanogr. Res. Pap.* **1981**, *28*, 1605–1618.
[7]   F. J. Millero, A. Poisson, *Deep Sea Res. Part A. Oceanogr. Res. Pap.* **1981**, *28*, 625–629.
[8]   T. E. Ouldridge, P. Šulc, F. Romano, J. P. K. Doye, A. A. Louis, *Nucleic Acids Res.* **2013**, *41*, 8886–8895.

9. Author Contributions

A.I. performed the experiments, the simulations and analyzed the data. A.I., C. B. M. and D.B. conceived, designed the experiments and simulations, and wrote the manuscript.

Appendix B

Paper 2: Hadean dew cycles drive DNA evolution

Check for updates

OPEN

Water cycles in a Hadean CO$_2$ atmosphere drive the evolution of long DNA

Alan Ianeselli[1,2], Miguel Atienza[1], Patrick W. Kudella [1,2], Ulrich Gerland [2,3], Christof B. Mast [1,2] and Dieter Braun [1,2] ✉

Dew is a common form of water that deposits from saturated air on colder surfaces. Although presumably common on primordial Earth, its potential involvement in the origin of life in early replication has not been investigated in detail. Here we report that it can drive the first stages of Darwinian evolution for DNA and RNA, first by periodically denaturing their structures at low temperatures and second by promoting the replication of long strands over short, faster replicating ones. Our experiments mimicked a partially water-filled primordial rock pore in the probable CO$_2$ atmosphere of Hadean Earth. Under heat flow, water continuously evaporated and recondensed as acidic dew droplets that created the humidity, salt and pH cycles that match many prebiotic replication chemistries. In low-salt and low-pH regimes, the strands melted at 30 K below the bulk melting temperature, whereas longer sequences preferentially accumulated at the droplet interface. Under an enzymatic replication to mimic a sped-up RNA world, long sequences of more than 1,000 nucleotides emerged. The replication was biased by the melting conditions of the dew and the initial short ATGC strands evolved into long AT-rich sequences with repetitive and structured nucleotide composition.

The autonomous replication, mutation and selection of genetic information is central to the origin of life and the onset of Darwinian evolution. It is necessary for RNA or DNA to periodically separate their strands to start a successive replication cycle. Without a denaturation mechanism, the replication encounters a dead-end[1]. Melting by heat has limitations because high temperatures can induce damaging side reactions and lead to the hydrolysis of chemical reagents[2] as well as the RNA[3] itself. Moreover, the temperature required to separate RNA strands can become higher than 100 °C and therefore impossible to reach in aqueous solution.

Low salt concentrations can destabilize double strands and facilitate denaturation[4]. However, many replication reactions and catalytic RNAs require elevated concentrations of ions to function[5]. For example, Mg^{2+} strongly stabilizes oligonucleotides in the duplex form. It thus seems that the physico-chemical conditions that favour replication reactions are, at the same time, incompatible with the melting of oligonucleotides. Many studies suggest other denaturation methods, such as Na$^+$ oscillations[6], low pH[7,8] or chaotropic agents (for example, urea[9] or formamide[10]). However, how any of these methods could be integrated in a primordial autonomous replication remains unclear.

A replicative system must also drive the evolution of the sequence information. It is known that the longer oligonucleotides are quickly lost, because the shorter oligomers are replicated with faster kinetics and quickly outcompete them. This means that, in a pool of sequences, shorter sequences will prevail and longer ones will progressively die out. Mutations in the replication process cause changes in the sequence length and thus start an evolutionary race towards the shortest oligomers, leading to a progressive loss of genetic information. This phenomenon, first demonstrated by Spiegelman[11], is known as the 'tyranny of the shortest' and is a problem for the onset of Darwinian evolution.

The sequence space of long oligonucleotides is immense. In this vast entropic land, the spontaneous emergence of sequences that contain particular motifs, secondary structures or that are enriched in specific nucleotides becomes rare. Without a selective mechanism that can reduce the sequence space, any sequence bias is likely to remain unexplored and not emerge[12]. For example, the assembly of short oligomers into active ribozymes requires the presence of particular sequences that can assemble by complementarity to build a ribozyme with catalytic activity[13,14].

The composition of Earth's atmosphere has changed substantially over geological time[15]. High CO$_2$ pressure (between 0.1 and 10 bar) was likely in the Hadean eon[16]. Such an atmosphere could have drastically affected the prebiotic chemistry—when gaseous CO$_2$ is dissolved in water, it leads to the formation of carbonic acid, bicarbonate and carbonate, lowering the pH of the water (Supplementary Section 1). The pH is a direct function of the partial pressure of CO$_2$ (p_{CO_2})[17] and the surface waters of early Earth probably had an acidic pH. Condensed water can reach particularly low pH (~4) due to its high purity and thus lack of pH-buffering salt molecules.

We developed a laboratory model of a heated rock pore[18] to cyclically generate dew droplets at the microscale level. This consisted of a thin rock-like pore containing gas and liquid. The gas was enriched with Hadean levels of CO$_2$ (0.1–1 bar) and the pore was heated by a temperature gradient to imitate the heat sources of the Early Earth[18]. Water evaporated and condensed to form salt-free dew droplets that absorbed CO$_2$ and became acidified (pH of ~4), then induced RNA and DNA melting by means of their acidity and low salt levels. The bulk retained high salt levels and neutral pH, preserving conditions ideal for reannealing and replication. The dew chamber allowed for DNA replication at 30 K below the bulk melting temperature.

Moreover, oligonucleotides accumulated at the gas–liquid boundaries at up to 10,000-fold (where fold indicates the increase in concentration relative to the starting concentration). The accumulation favoured the longer strands, which were then preferentially replicated. The DNA wet–dry cycles induced unspecific annealing of the strands, which recombined into sequences of increasing

[1]Systems Biophysics, Ludwig Maximilian University Munich, München, Germany. [2]Center for NanoScience (CeNS), Ludwig Maximilian University Munich, München, Germany. [3]Physics of Complex Biosystems, Technical University of Munich, Garching, Germany. ✉e-mail: dieter.braun@lmu.de
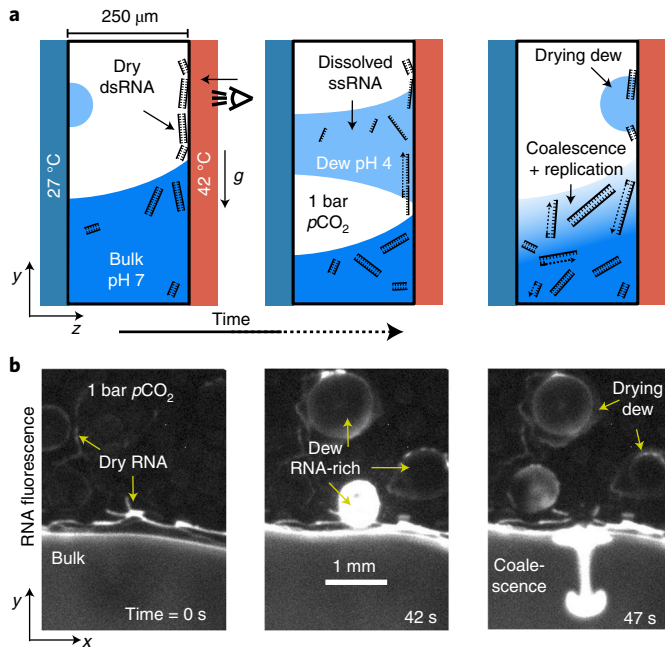
Fig. 1 | A heated rock pore at Hadean CO$_2$ levels generates acidic dew cycles. The continuous formation of dew in a rock pore at Hadean p_{CO_2} generates cycles of RNA melting, as well as RNA wet–dry cycles. **a**, Scheme of the dew cycle at Hadean CO$_2$ levels. The water that evaporates condenses as acidic dew droplets that contain low salt. The dew droplets grow and create a capillary bridge between the pore surfaces. RNA oscillates between the dry and the wet states and denatures in the dew. The salt-rich bulk maintains a neutral pH that allows reannealing and replication of the oligonucleotides. **b**, Fluorescence images (FAM-labelled (carboxyfluorescein) single-stranded RNA (ssRNA), 51 nt) of the dew cycle, imaged through the z axis.

complexity and length. As the sequences grew longer, their stability against denaturation increased. It is known that the stability of double-stranded DNA (dsDNA) is also determined by the fraction of AT versus GC[19]. We found that the replication by CO$_2$ fog cycles modulated the selection of oligonucleotides with an ATGC composition compatible with the melting conditions of the dew, drastically reducing the sequence space. At the same time, the length of the DNAs increased by more than 25×, but, to ensure their melting, they were strongly enriched in AT (AT fraction >80%). This showed that fog cycles avoid Spiegelman's dominance of the shortest sequence, promote the Darwinian evolution of long DNAs and allow low-entropy sequence biases to emerge.

Results and discussion

Figure 1a presents a scheme of the microfluidic CO$_2$ dew chamber, viewed laterally (Supplementary Section 2). The temperature gradient across the thin chamber (250 μm), half-filled with a Mg^{2+}-rich solution and RNA (or DNA), creates a dew cycle at the microscale level. Evaporation at the warm side is balanced by condensation on the cold side, where acidic dew droplets of purified water are formed. Oligomers accumulate at the evaporating gas–liquid interfaces[20] (coffee-ring effect) and periodically dry out on the warm wall during the evaporation–condensation–coalescence cycles. Besides condensation, the dew droplets also grow by fusion with other droplets. When the droplet radius exceeds the chamber thickness (250 μm), surface tension rearranges the dew droplets into a capillary bridge between the chamber walls. At this point, the dew redissolves the dry oligomers on the warm wall. The low pH and low salt concentration efficiently denature the oligonucleotides.

Figure 1b shows the process via fluorescence, using fluorescently labelled RNA, imaged through the warm side (viewed perpendicular with respect to Fig. 1a; Supplementary Video 1). The dew either dries out and redeposits oligonucleotides on the warm side or grows large by fusion then coalesces with the bulk, where the oligonucleotides can be promptly replicated and elongated (Supplementary Section 3).

We expected the dew droplets to have a reduced concentration of buffers and salts and thus be particularly susceptible to the acidification induced by CO$_2$ absorption. On the other hand, the bulk would remain buffer-rich and maintain a quasi-neutral pH. The result would be pH and salt oscillations that lead to periodic melting of RNA in the dew and reannealing in the bulk. The pH and RNA conformation were measured by fluorescence microscopy. pH was measured with the ratiometric dye Lysosensor Yellow/Blue DND-160. RNA conformation was measured by fluorescence resonance energy transfer (FRET), using FRET-pair fluorophores positioned centrally on opposite strands[21] (Supplementary Section 4).

The pH of the dew and bulk during the dew cycle was measured at a range of CO$_2$ pressures. The bulk contained 10 mM MgCl$_2$ and 10 mM Tris (initial pH 7.0), to which Lysosensor Yellow/Blue DND-160 was added at 20 μM for pH imaging. A temperature gradient of 5 °C was applied (hot side 27 °C, cold side 22 °C). Fluorescence images are presented in Fig. 2a. At room p_{CO_2} levels (0.4 mbar), the pH of the bulk was neutral (7.0 ± 0.2)(mean ± standard deviation). In the dew droplets we found slightly acidic pH (5.6 ± 0.3), as expected for very low salt water at room CO$_2$. At higher pCO$_2$ (1 bar), the bulk pH dropped to 5.8 (±0.2), even though it contained Tris buffer. The dew acidified down to pH 4.0 (±0.4). The experimental data were compared to a theoretical model based on the rate equations of CO$_2$ absorption into water or into a buffered solution (Fig. 2b). In the dew droplets, the pH drastically dropped with increasing p_{CO_2}. In the bulk, the buffer molecules neutralized the carbonic acid and dampened the pH change.

Prebiotically, the pH of an aqueous solution is probably buffered by the minerals in contact with the liquid by means of mineral dissolution, ion exchange and surface complexation reactions[22]. Silicate minerals—ubiquitous rock-forming minerals[23]—can act as a buffer and maintain neutral pH in the long term[24]. The process of pH buffering by minerals requires several days[25], much slower than dew cycles (which require seconds). Accordingly, dew cycles can plausibly create local and temporary acidic spikes on top of a buffered bulk, similar to what we are showing.

We expected the acidity and the low salt content of the dew to be strongly denaturing conditions. The bulk, instead, retained high salt levels and quasi-neutral pH, ideal for stabilizing duplexes. We studied the conformation of a 24-bp dsRNA (33% GC, melting temperature (T_m) = 66 °C) in a solution of 12.5 mM MgCl$_2$ and 10 mM Tris (initial pH of 7.0). The chamber walls were differentially heated at 31 °C and 43 °C (ΔT = 12 °C). The temperature of the chamber was, on average, 29 °C below the RNA T_m. In the dew, the dsRNA fraction decreased proportionally with increasing p_{CO_2} (Fig. 2c), from 0.78 (±0.05) at ambient CO$_2$ down to 0.17 (±0.08) for $p_{CO_2} \geq 0.8$ bar. In the bulk, the dsRNA fraction remained close to 100%. Fluorescence images are shown in Fig. 2d and Supplementary Video 2.

The RNA FRET experiments were compared to a hybridization model based on the Van 't Hoff equation (Supplementary Section 5). The model was created by fitting experimental RNA melting curves measured at different pH values, Mg^{2+} concentrations and for different RNA sequences. The best agreement between experiments and the model was for a Mg^{2+} concentration in the dew of between 0.5 and 0.1 mM (Fig. 2c), which corresponds to an ~50–100× reduction compared to the bulk. This concentration agrees well with measurements of the salt content of rainwater[26]. With the same hybridization model we calculated the duplex RNA fraction (RNA FRET) as a function of pH and Mg^{2+} concentration (Fig. 2e).
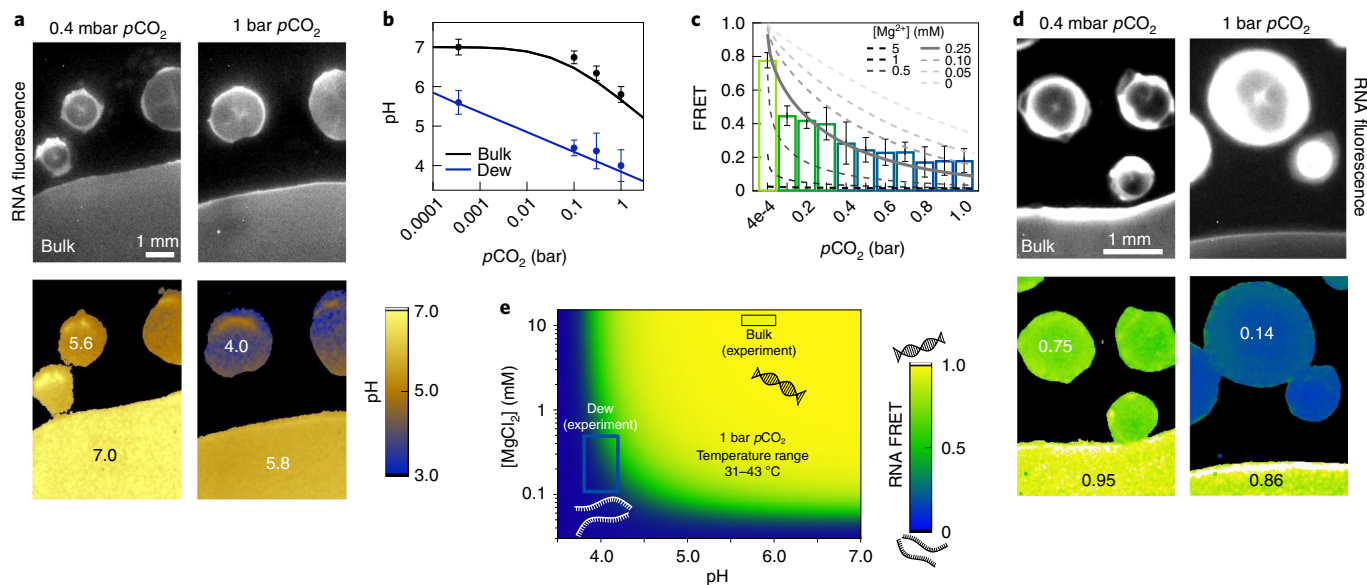
Fig. 2 | RNA melts at low temperature in the acidic low-salt dew at a p_{CO_2} of 1 bar. A synergistic combination of low salts, low pH and temperature is necessary to generate strong denaturing conditions for RNA melting at low temperatures. **a**, Dew and bulk viewed by RNA fluorescence (top) and corresponding pH (bottom). Dew droplets at a p_{CO_2} of 1 bar acidify to pH 4, while the bulk remains almost pH-neutral. **b**, Model (lines) and experimental (points) bulk and dew pH as a function of p_{CO_2}. Error bars represent the standard deviation ($n \approx 3$). The dew pH drops with increasing p_{CO_2}, whereas the bulk is buffered by the salts. **c**, Model (lines) and experiments (bars) of RNA FRET in the dew as a function of p_{CO_2}. Error bars represent the standard deviation ($n \approx 4$). RNA melts with increasing p_{CO_2} inside dew droplets that contain low salts (0.25 mM Mg^{2+}). **d**, Dew and bulk viewed by RNA fluorescence (top) and corresponding RNA FRET (bottom). RNA melts in the acidic, low-salt dew (RNA FRET = 0.14). In the salt-rich bulk, the RNA remains double-stranded (RNA FRET = 0.86). **e**, Surface plot (model) showing how pH and Mg^{2+} cooperatively affect the duplex RNA fraction (RNA FRET). Experimental RNA FRET values for bulk and dew droplets are shown as rectangles.

The relationship between Mg^{2+}, pH and RNA FRET was nonlinear. We observed a sharp drop in RNA FRET at certain values of pH and Mg^{2+}, suggesting that pH, Mg^{2+} and temperature are acting synergistically.

It is important to note that, due to the technical limitations of the pH-imaging method, the pH measurements of Fig. 2a were performed at 27 °C (warm side). However, the FRET measurements of Fig. 2d or the later replication experiments of Fig. 4a–d were instead performed at a higher temperature (warm side: 43 °C, 67 °C and 60 °C, respectively). Increasing the temperature can affect the pH of aqueous solutions[27,28]. The pH of CO_2-saturated buffer-free water (that is, the dew) at a p_{CO_2} of 1 bar undergoes negligible changes with increasing temperature ($\Delta pH/20 °C = +0.1$)[29]. The dew's pH is supposed to remain at ~4.0 up to 80 °C. On the other hand, we determined that the bulk could retain annealing conditions (duplex fraction >0.8) down to a pH of ~4.3 (Supplementary Section 5). A pH acidification of this magnitude is, however, not observed for neutral buffered solutions at a p_{CO_2} of 1 bar, which tend to remain more neutral[30,31]. Hence, the main features of the water–dew cycles are stable across the different temperatures: acidic low-salt dew for the denaturation of oligonucleotides, and salt-rich and moderate pH in the bulk for annealing.

The dual combination of low salt content and low pH in the dew created a strong denaturing microenvironment that efficiently melted RNA at temperatures 30 K below the bulk T_m. No high-temperature spikes were needed to induce melting, maintaining a low RNA hydrolysis rate and therefore preserving sequence integrity for a longer time. However, selection pressure towards the survival of the longer RNA (or DNA) strands must be present in the system to overcome the 'tyranny of the shortest'.

By simulation, we studied whether the non-equilibrium conditions of the dew chamber could host selective mechanisms for oligonucleotide length. We performed a three-dimensional (3D) finite-element

simulation of an evaporating dew droplet and bulk, using the software COMSOL Multiphysics. The simulation was performed for DNA so as to simulate the DNA accumulation that takes place during the replication reactions that will follow. The diffusion coefficients (D) of DNA and RNA are in fact very similar ($D_{ssDNA}/D_{ssRNA} = 1.15$)[32]. The capillary flow, diffusion, thermophoresis and transport of dissolved DNA in a temperature gradient of 17 °C (hot side 60 °C, cold side 43 °C) were simulated. The size and shape of the simulated dew and bulk were geometrically identical to those in our experiments, as was the shape of the meniscus at the gas–water boundaries (Supplementary Section 6). The thermal gradient induced convection in the bulk and in the dew, with an average speed of 25 μm s⁻¹. The differential evaporation rates at the warm and cold sides created a capillary flow with an average speed of 50 μm s⁻¹ directed towards the hot side (Fig. 3a). The result was a net transport of DNA, driven by a continuous coffee-ring effect, that strongly accumulated DNA (up to 10,000+ fold for a 77-nt DNA) at the gas–liquid interface on the warm side. Our observations by fluorescence microscopy compared qualitatively well with the simulation results (Fig. 3b,c).

The accumulation favoured longer DNA sequences (Fig. 3d). Because the diffusion coefficient of DNA decreases with length[33], longer DNA molecules accumulated more strongly, as they had a slower back-diffusivity. The effect was more pronounced at the gas–water interface of the bulk, where it reached an accumulation factor of 20,000+ for a 300-nt DNA (versus 1,200+ at the dew's interface).

So far, the CO_2 dew chamber has shown characteristics that are essential for a molecular replicator in the RNA world:

- Melting of oligonucleotides in the dew at 30 K below the bulk T_m. This provides low thermal stress to RNA while allowing long RNA sequences to cyclically melt and reanneal. The bulk also retains the high salt concentrations that are necessary for prebiotic replication chemistries.
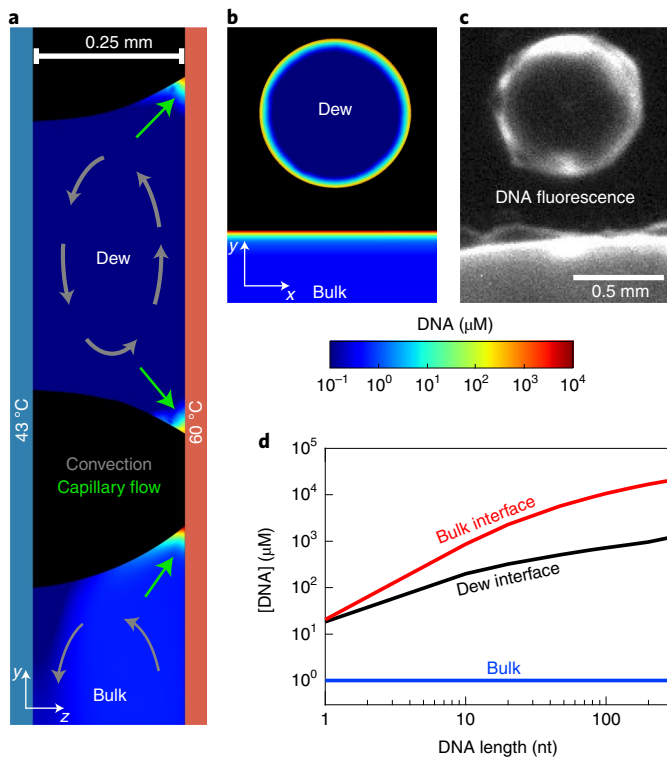
Fig. 3 | Simulations predict the accumulation of longer DNA at gas–water interfaces. The preferential accumulation of longer DNA strands counteracts the tyranny of shorter sequences. **a**, Lateral distribution of DNA (77 nt) in the dew and bulk at steady state. Surface tension dictates the shape of the dew droplets (capillary bridge) and of the bulk (concave meniscus). Owing to a continuous coffee-ring effect, DNA accumulates at the gas–water boundaries. **b**, The same simulation viewed frontally (resized). **c**, Fluorescence image of DNA accumulation. **d**, Accumulation as a function of DNA length (1–300 nt). Owing to their lower diffusion coefficient, longer DNA strands are favoured and accumulate more strongly. Each data point corresponds to a simulation performed with a given DNA length.

- Preferential accumulation of longer oligonucleotides at the evaporating gas–water interfaces. This feature can promote replication of the longer sequences, avoiding the detrimental kinetic race towards the shortest oligomers, as we have shown in the past for a bulk DNA replication in an open pore under thermal cycling[34].

To mimic the yet-to-be-discovered replication mechanisms of the RNA world, assuming they existed, in the experiment we used a DNA replicating protein. First, we wanted to confirm that our CO_2 dew chamber was able to perform DNA replication at temperatures much less than T_m. The *Taq* DNA polymerase enzyme has been used to amplify a 51-bp DNA (54% GC, T_m 88 °C) by templated polymerization. The mixture (QIAGEN Master Mix) consisted of 10 mM Tris (starting pH 8.2 ± 0.1), KCl and $(NH_4)_2SO_4$ (concentration not specified), 1.5 mM $MgCl_2$, nucleotides (200 μM each), DNA polymerase (2.5 U μl^{-1}), to which we added the DNA template (0.5 nM) and complementary primers (forward and reverse, each at 0.25 μM). The solution was inserted inside the dew chamber in a temperature gradient of 15 °C (warm side 67 °C, cold side 52 °C). The average chamber temperature was 28 °C lower than the template T_m. After ~5 h of experiment, SYBR Green I fluorescence (a dsDNA fluorescent stain) started increasing in the bulk in the classical exponential manner (Fig. 4a,b and Supplementary Video 3). The replication

product was confirmed on a 15% denaturing polyacrylamide gel (Fig. 4c). No replication was observed without CO_2 enrichment, because no substantial DNA melting could occur in the dew and the whole replication could not continue further.

We studied whether the preferential accumulation of longer DNAs at the evaporating gas–water interfaces could actually prevent the 'tyranny of the shortest' sequences during replication. Under standard replication conditions (for example, standard thermocycling protocols), shorter DNA sequences have a kinetic advantage and prevail over the longer ones. This can be seen in the polyacrylamide gel electrophoresis (PAGE) results in Fig. 4d, fourth lane. In this experiment, two DNA templates of different lengths were used—47 nt (53% GC, T_m = 78 °C) and 77 nt (51% GC, T_m = 89 °C)—which shared the same primer binding sites. The replication of the shorter sequence (47 nt) prevailed and completely hindered the longer strand (77 nt).

The replication reaction was then performed in the CO_2 dew chamber. We applied a temperature gradient of 17 °C (hot side 60 °C, cold side 43 °C) and enriched the gas with 1 bar of pCO_2. After ~12 h, the reaction was stopped and the product was measured on the gel. As shown in Fig. 4d (sixth lane), not only could both DNA templates be replicated with comparable efficiency, but additional longer DNAs unexpectedly emerged in the CO_2 dew replication. This indicated that the length-selective features of DNA accumulation at the gas–water interfaces promoted the survival and replication of the longer strands. The longer DNA products were observed only in the dew chamber enriched in pCO_2, suggesting that they arose as a combination of enhanced DNA melting + preferential accumulation of long DNAs. In an ambient atmosphere (lane 7), only primer dimers were observed (similar to the negative control experiment without DNA templates, lane 8). The longer DNAs were probably created during the DNA wet–dry cycles, where the extremely high DNA and enzyme concentrations forced unspecific annealing and polymerization, leading to elongation and shortening processes. This created novel and mixed DNA sequences of increasing complexity. Also the formation of hairpins and other forms of self-priming can drive the formation of long replication strands[35]. But what are those long DNA products?

The products were sequenced using the Nanopore technique MinION (Methods). The sequencing machine yielded 2,856 reads with lengths between 140 and 1,300 nt. Reads shorter than 140 nt were not detected. In the length range of 140–300 nt, the reads contained numerous repetitions of primers and templates, attached one after the other multiple times, in a mixed and repetitive manner (Supplementary Section 7). With increasing lengths (up to 1,300 nt), the nucleotide composition of the reads was revealed to be biased towards AT (AT fraction >80%) and the primer/template repetitions were lost and could only rarely be found. The question is why the nucleotide composition of the sequences is so biased towards AT (>80%). To obtain such a bias in the immense sequence space of long oligonucleotides is entropically unfavourable. The answer lies in the adaptation of the sequences to the melting conditions of the dew, as we will demonstrate in the following sections.

The reads are plotted in Fig. 5a,b according to their AT and CG counts. This was done because the AT:GC ratio is one major factor that determines the stability of DNA duplexes[19]. The background of Fig. 5a,b corresponds to the duplex DNA fraction (indicated as DNA FRET) computed as a function of the AT and GC counts under the conditions of the CO_2 dew (pCO_2 of 1 bar, pH 4, Mg^{2+} 0.25 mM, temperature range 43–60 °C). The longer AT-rich reads (white circles) lie in a region of low-DNA FRET (0.14 ± 0.12), far away from what is expected from a pool of randomized sequences (black circles). No reads were found in the yellow area to the right or at the left blue extreme of the map. This suggests that the sequences with low stability, which were more prone to undergo multiple cycles of denaturation and reannealing, were the ones preferen-
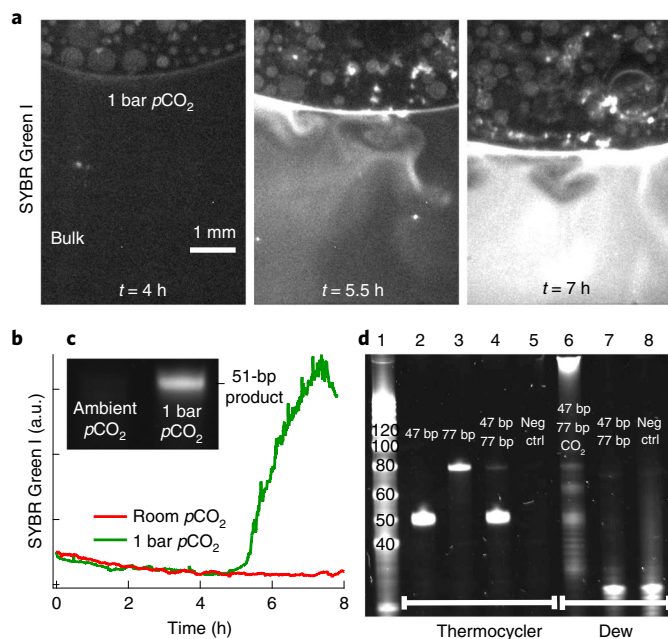
Fig. 4 | Dew cycles at 1-bar CO$_2$ drive the replication of long DNAs. The dew chamber enables DNA replication at cold temperatures and drives molecular evolution towards longer strands. **a–c**, Replication of a single DNA template (51 nt). In **a**, fluorescence (SYBR Green I) images are shown of the replication reaction at different times. DNA accumulates and replicates at the gas–water interfaces and undergoes repeated wet–dry cycles. Dry replicative spots can be seen above the gas–water interface. In **b**, SYBR Green I fluorescence over time is shown for the CO$_2$ dew chamber replication, showing classic exponential behaviour. In **c**, PAGE (15% denaturing, SYBR Gold staining) of the reaction products is shown. DNA replication is only possible at 1-bar pCO$_2$. **d**, Replication with two DNA templates (47 and 77 nt), shown by PAGE of the reaction. The numbers at the top indicate the lanes. In contrast to the replication in the thermocycler, the CO$_2$ dew chamber avoids the 'tyranny of the shortest' sequences and favours longer DNAs.

tially replicated. DNA sequences with a too high or too low melting temperature replicated more slowly, because they struggled to be cyclically melted and to template. In this sense, the DNA FRET landscape of the CO$_2$ dew selected which sequences were replicated and which ones died out.

To prove the generality of this concept—sequence adaptation to the melting conditions—we emulated an unspecific replication process via a stochastic model (Supplementary Section 8). Starting from an initial pool of DNAs, at every step the model calculated the probability of each sequence to be replicated according to its stability on the DNA FRET landscape of the dew. When a sequence was replicated, its reverse complement was created and a mutation introduced. The mutation consisted of the insertion or deletion of a random subsequence at a random position (Fig. 5c). This was done to mimic the unspecific templation characteristics seen in the CO$_2$ dew replication experiments. Finally, at every step, random single-point mutations in the sequences were introduced with the frequency of the *Taq* polymerase error rate (1×10^{-4})[36]. The results are shown in Fig. 5a,b.

The simulation was started from the initial templates or from the sequences rich in template/primer repetitions. In both cases, the sequences replicated and randomly mutated. The DNA FRET landscape preferentially replicated the mutated sequences that best matched the denaturing conditions of the CO$_2$ dew (that is, low FRET). The DNA sequences that were too stable or too unstable

could not replicate further and were discarded. As a consequence, the DNA evolved towards longer sequences rich in AT. The ATGC content was thus adapting to the melting conditions of the environment. The simulation also highlighted a progressive loss of the intact templates within the sequence (pink gradient in Fig. 5a,b), similar to what has been observed experimentally, and a consequence of the progressive mutations at every replication step. The dashed lines (in Fig. 5a,b) correspond to other simulations using different parameters.

A similar sequence evolution was also observed for starting templates rich in GC (Fig. 5b, orange line), as is often the case in many non-enzymatic primer extension chemistries[37,38].

To understand the nucleotide sequence of these long AT-enriched reads, we counted the frequency of every 4-nt submer combination that could be found within the reads. As shown in Fig. 5d, the most frequent submers were those rich in AT (AT fraction ≥ 0.75), with some of the most abundant ones being ATAT, AATA (experiment) and AAAA, TTAT (model). Both the experiment and the model showed similar fingerprints, with small differences in the most abundant combinations. The frequency distribution was also very different from a random pool.

The difference from a random pool could also be seen in terms of the relative reduction of Shannon entropy, as shown in Fig. 5e. This indicates the average decrease in the level of information encoded in the replicated sequences, relative to a random pool (the latter contains the maximum possible amount of information)[39]. Calculated as a function of the submer length, the relative entropy reduction in our experiments and model was <1 overall and reached a minimum of 0.56 (experiment) and 0.66 (model). In other words, the replicative constraint introduced by the DNA FRET landscape drove a selection of sequences that reduced the informational entropy by 44% (experiment) and 34% (model). This drastic reduction in entropy allowed the sequences to replicate and evolve in a subset of the sequence space that would be otherwise too immense to be explored[12].

The model reproduced the key features and fingerprints that were measured in the experiments. Owing to its simplicity and purely stochastic nature, the model confirmed the hypothesis of the sequence adaptation to the melting conditions of the environment.

In a molecular replicator where DNAs evolve and adapt to the environment, it should be possible to modulate the final ATGC composition of the sequences by varying the melting conditions of the setting. Higher temperatures facilitate the melting of more stable DNA sequences (those richer in GC), moving the region of low DNA FRET towards higher GC fractions. We varied the average temperature of the dew chamber while maintaining a fixed temperature gradient of 17 °C (Fig. 5f). In the range from 50 to 75 °C, the AT:GC ratio of the replicated sequences changed from 8.0 ± 1.0 to 0.9 ± 0.1, respectively (model). A similar trend was observed in the experiments, where it dropped from 4.7 ± 1.1 to 0.9 ± 0.6 when the average chamber temperature was increased from 51 to 67 °C. The final ATGC composition was driven by the DNA stability landscape of the dew droplets, which was synergistically determined by their Mg^{2+} concentration (<0.25 mM), their pH (pH 4 at a p_{CO_2} of 1 bar) and the temperature.

Starting with an out-of-equilibrium condition, we have demonstrated an autonomous molecular replicator of oligonucleotides that is compatible with an RNA world: low-temperature melting minimized the hydrolysis rates, and high salt levels were provided for prebiotic replication chemistries and for the catalytic activity of RNAs.

Conclusions

A CO$_2$ dew chamber could accommodate the essential features of a molecular replicator in the context of the origin of life on Earth and the RNA world. It mimics the ubiquitous setting of a heated
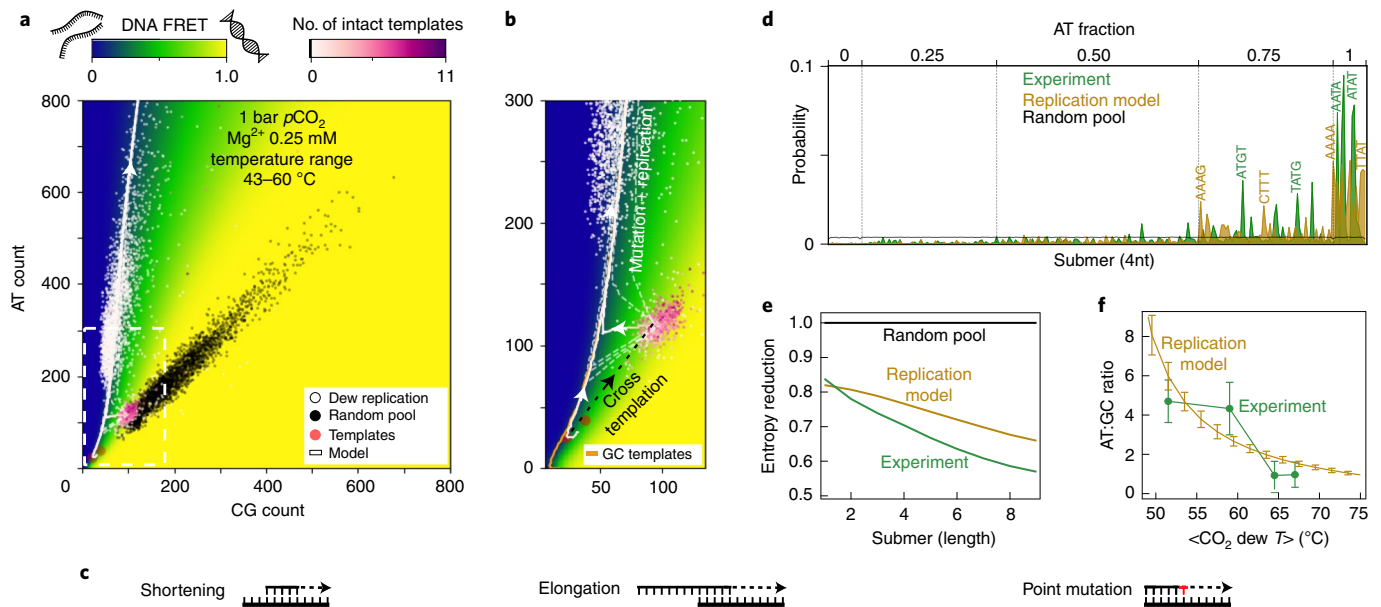
Fig. 5 | New DNA sequences rich in AT emerge during the CO_2 dew cycles. The CO_2 dew chamber triggers the emergence of long DNA strands, the ATGC compositions of which correlate with the denaturing conditions of the dew. **a**, Reads (white circles) are plotted according to their AT (y axis) and CG (x axis) count. The background colour corresponds to the simulated duplex fraction (DNA FRET) in the CO_2 dew. Denaturing conditions (DNA FRET = 0.14 ± 0.12) correlate with the sequence composition of the reads and drove the evolution of the sequences. The purple colourmap indicates the number of intact templates found in the read. **b**, Zoomed subsection (dashed box in **a**) of the surface plot. Starting from the initial templates, the DNA sequences, whether directly evolved towards the long AT-rich strands by means of mutations or into templates-rich strands, are driven by cross-templation. Similar results were observed when starting with a pool of 6–30-nt short templates rich in GC (orange line). **c**, Shortening, elongation and mutation processes modify the sequences during the replication in the dew cycles. **d**, Probability of every 4-nt subsequence combination (ordered by AT fraction) that were found in the experimental reads (green), in the model (gold) or in a random pool (black). The replication in the dew drove the evolution of sequences that frequently contain AT-rich motifs. **e**, DNA replication in the CO_2 dew drastically reduces the informational entropy. The model (gold) and the experiment (green) show a similar entropy reduction. **f**, The average ($<>$) temperature of the dew can be modulated to drive the final AT:GC composition of the replicated DNA pool, with higher temperatures leading to strands richer in GC. Error bars indicate standard deviation.

rock pore in a CO_2-rich Hadean atmosphere. The acidic dew leads to strand displacement of oligonucleotides at 30 K below the melting temperature. At the same time, the closed rock pore maintains a pH-neutral bulk solution rich in salts that promotes strand reannealing and replication. The low temperatures offer a moderate hydrolysis rate for RNA, allowing for extended survival of the genetic information. As a consequence of the DNA wet–dry cycles and the DNA length-selective accumulation at the gas–water interfaces, the sequences recombine with increasing length and complexity, overcoming the 'tyranny of the shortest' dilemma and building new genetic information. In this primordial molecular replicator, the new DNA sequences adapt to the melting conditions of the environment and evolve towards a biased ATGC composition of reduced entropy.

Hadean water cycles in a CO_2 atmosphere present adequate physico-chemical conditions to host the first reactions of molecular evolution during the origin of life. The non-equilibrium properties of the dew droplets boost chemical reactions that have limited efficiency under standard conditions. They provide a strong increase in concentrations at gas–water interfaces and during wet–dry cycles, fluctuations between low and high salt concentration and a periodic change between acidic and neutral pH. As shown here, the combination of the above processes enhances the replication of oligonucleotides with increasing lengths, opening the door to open-ended Darwinian evolution.

Online content
Any methods, additional references, Nature Research reporting summaries, source data, extended data, supplementary infor-

mation, acknowledgements, peer review information; details of author contributions and competing interests; and statements of data and code availability are available at https://doi.org/10.1038/s41567-022-01516-z.

References
1. Szostak, J. W. The eightfold path to non-enzymatic RNA replication. *J. Syst. Chem.* **3**, 2 (2012).
2. Taran, O., Thoennessen, O., Achilles, K. & von Kiedrowski, G. Synthesis of information-carrying polymers of mixed sequences from double stranded short deoxynucleotides. *J. Syst. Chem.* **1**, 9 (2010).
3. AbouHaidar, M. G. & Ivanov, I. G. Non-enzymatic RNA hydrolysis promoted by the combined catalytic activity of buffers and magnesium ions. *Z. Naturforsch. C.* **54**, 542–548 (1999).
4. Schildkraut, C. & Lifson, S. Dependence of the melting temperature of DNA on salt concentration. *Biopolymers* **3**, 195–208 (1965).
5. Hampel, A. & Cowan, J. A. A unique mechanism for RNA catalysis: the role of metal cofactors in hairpin ribozyme cleavage. *Chem. Biol.* **4**, 513–517 (1997).
6. Ianeselli, A., Mast, C. B. & Braun, D. Periodic melting of oligonucleotides by oscillating salt concentrations triggered by microscale water cycles inside heated rock pores. *Angew. Chem. Int. Ed.* **58**, 13155–13160 (2019).
7. Bunville, L. G., Geiduschek, E. P., Rawitscher, M. A. & Sturtevant, J. M. Kinetics and equilibria in the acid denaturation of deoxyribonucleic acids from various sources. *Biopolymers* **3**, 213–240 (1965).
8. Mariani, A., Bonfio, C., Johnson, C. M. & Sutherland, J. D. pH-driven RNA strand separation under prebiotically plausible conditions. *Biochemistry* **57**, 6382–6386 (2018).
9. Yoon, J., Thirumalai, D. & Hyeon, C. Urea-induced denaturation of PreQ₁-riboswitch. *J. Am. Chem. Soc.* **135**, 12112–12121 (2013).

10. Blake, R. D. & Delcourt, S. G. Thermodynamic effects of formamide on DNA stability. *Nucleic Acids Res.* **24**, 2095–2103 (1996).
11. Mills, D. R., Peterson, R. L. & Spiegelman, S. An extracellular Darwinian experiment with a self-duplicating nucleic acid molecule. *Proc. Natl Acad. Sci. USA* **58**, 217–224 (1967).
12. De Duve, C. The onset of selection. *Nature* **433**, 581–582 (2005).
13. Wachowius, F. & Holliger, P. Non-enzymatic assembly of a minimized RNA polymerase ribozyme. *ChemSystemsChem* **1**, 1–4 (2019).
14. Zhou, L., O'Flaherty, D. K. & Szostak, J. W. Assembly of a ribozyme ligase from short oligomers by nonenzymatic ligation. *J. Am. Chem. Soc.* **142**, 15961–15965 (2020).
15. Kasting, J. F. Earth's early atmosphere. *Science* **259**, 920–926 (1993).
16. Walker, J. C. G. Carbon dioxide on the early earth. *Orig. Life Evol. Biosph.* **16**, 117–127 (1985).
17. Byck, H. T. Effect of dissolved CO_2 on the pH of water. *Science* **75**, 224 (1932).
18. Agerschou, E. D., Mast, C. B. & Braun, D. Emergence of life from trapped nucleotides? Non-equilibrium behavior of oligonucleotides in thermal gradients. *Synlett* **28**, 56–63 (2017).
19. Wada, A. & Suyama, A. Local stability of DNA and RNA secondary structure and its relation to biological functions. *Prog. Biophys. Mol. Biol.* **47**, 113–157 (1986).
20. Morasch, M. et al. Heated gas bubbles enrich, crystallize, dry, phosphorylate and encapsulate prebiotic molecules. *Nat. Chem* **11**, 779–788 (2019).
21. Didenko, V. V. DNA probes using fluorescence resonance energy transfer (FRET): designs and applications. *Biotechniques* **31**, 1106–1116 (2001).
22. Seibert, S. et al. Identification and quantification of redox and pH buffering processes in a heterogeneous, low carbonate aquifer during managed aquifer recharge. *Water Resour. Res.* **52**, 4003–4025 (2016).
23. Appelo, C. & Postma, D. *Geochemistry, Groundwater and Pollution* (CRC Press, 2004).
24. Lacroix, E., Brovelli, A., Holliger, C. & Barry, D. A. Evaluation of silicate minerals for pH control during bioremediation: application to chlorinated solvents. *Water Air Soil Pollut.* **223**, 2663–2684 (2012).
25. Lacroix, E., Brovelli, A., Holliger, C. & Barry, D. A. Control of groundwater pH during bioremediation: improvement and validation of a geochemical model to assess the buffering potential of ground silicate minerals. *J. Contam. Hydrol.* **160**, 21–29 (2014).
26. Carroll, D., Udall, S. L. & Nolan, T. B. *Rainwater as a Chemical Agent of Geologic Processes: A Review. Chemical Composition of Rainwater and Its Probable Relation to Soil Water and Exchangeable Cations in Weathering Processes* (US Department of the Interior, 1962).
27. Langelier, W. F. Effect of temperature on the pH of natural waters. *J. Am. Water Works Assoc.* **38**, 179–185 (1946).
28. Gieskes, J. M. Effect of temperature on the pH of seawater. *Limnol. Oceanogr.* **15**, 329–329 (1970).
29. Peng, C., Crawshaw, J. P., Maitland, G. C., Martin Trusler, J. P. & Vega-Maza, D. The pH of CO_2-saturated water at temperatures between 308 K and 423 K at pressures up to 15 MPa. *J. Supercrit. Fluids* **82**, 129–137 (2013).
30. Liu, Q. & Maroto-Valer, M. M. Investigation of the effect of brine composition and pH buffer on CO_2-brine sequestration. *Energy Procedia* **4**, 4503–4507 (2011).
31. Holmes, J. D. et al. Buffering the aqueous phase pH in water-in-CO_2 microemulsions. *J. Phys. Chem. B* **103**, 5703–5711 (1999).
32. Baaske, P. et al. Extreme accumulation of nucleotides in simulated hydrothermal pore systems. *Proc. Natl Acad. Sci. USA* **104**, 9346–9351 (2007).
33. Mast, C. B., Schink, S., Gerland, U. & Braun, D. Escalation of polymerization in a thermal gradient. *Proc. Natl Acad. Sci. USA* **110**, 8030–8035 (2013).
34. Kreysing, M., Keil, L., Lanzmich, S. & Braun, D. Heat flux across an open pore enables the continuous replication and selection of oligonucleotides towards increasing length. *Nat. Chem.* **7**, 203–208 (2015).
35. Park, D., Ellington, A. D. & Jung, C. Selection of self-priming molecular replicators. *Nucleic Acids Res.* **47**, 2169–2176 (2019).
36. Potapov, V. & Ong, J. L. Examining sources of error in PCR by single-molecule sequencing. *PLoS ONE* **12**, e0169774 (2017).
37. Duzdevich, D. et al. Competition between bridged dinucleotides and activated mononucleotides determines the error frequency of nonenzymatic RNA primer extension. *Nucleic Acids Res.* **49**, 3681–3691 (2021).
38. Blain, J. C., Ricardo, A. & Szostak, J. W. Synthesis and nonenzymatic template-directed polymerization of 2'-amino-2'-deoxythreose nucleotides. *J. Am. Chem. Soc.* **136**, 2033–2039 (2014).
39. Shannon, C. E. A mathematical theory of communication. *Bell Syst. Tech. J.* **27**, 623–656 (1948).

Methods

The experiments were carried out in a microfluidic chamber ($250\,\mu m \times 30\,mm \times 14\,mm$) made of Teflon, placed on a silicon wafer and then between a transparent sapphire and a copper back plate. The silicon wafer was covered with a thin ($50\,\mu m$) Teflon foil to increase the hydrophobicity. The liquid volume of every experiment was ~20 μl, corresponding to one-third of the chamber volume. The remaining two-thirds of the volume was left for the gas. A temperature gradient was produced by differentially heating the sapphire with rod resistors and the silicon back plate with a Peltier element. The temperature gradients applied in the experiments ranged from 5 to 17 °C. The software LabVIEW was used to maintain a constant target temperature with an accuracy of ±1 °C. Microfluidic tubings were connected to the chamber for the inflows and outflows of liquid, to control the flux of CO_2 and to measure the barometric pressure within the chamber. The fluorescent microscope pointed towards the transparent sapphire and was focused on the cold wall.

The set-up for FRET and pH imaging consisted of a custom-built fluorescence microscope (with the body of a Zeiss Axiotech Vario microscope) equipped with four excitation light-emitting diodes (M340L4, M385L2, M470L2, M590L2; Thorlabs), excitation filters (BP 340/26, BP 379/34, BP 482/35, BP 588/20), beamsplitters (DC 475/40, DC 425 LP, DC 365 LP), a triple-edge dichroic mirror (DC 395/495/610), an Optosplit II with a ratiometric filter set (DC 600 LP, BP 536/40, BP 630/50), a Stingray-F145B ASG camera (ALLIED Vision Technologies) and a ×1 objective (AC254 100-A-ML Achromatic Doublet). The specifications for the light-emitting diodes, filters, beamsplitters and dichroic mirrors are given in nanometres (average/full-width at half-maximum). A schematic of the set-up is provided in Supplementary Section 4.

RNA oligonucleotides were purchased from biomers.net, with high-performance liquid chromatography purification. The sequences used for the FRET experiments were as follows (5′–3′)—24-bp RNA 33% GC: strand forward CGU AGU AAA UAT *FAM* CUA GCU AAA GUG, strand reverse CAC UUU AGC UAG AT*ROX*A UUU ACU ACG; 24-bp RNA 0% GC: strand forward AAA UAA AUA AUA T*FAM*AA AAU AAU AAA, strand reverse UUU AUU AUU UUA T*ROX*AU UAU UUA UUU. The two labelled complementary strands were diluted from stock solution (100 μM in nuclease-free water) and mixed together to a final concentration of 5 μM in salt-rich buffer (Tris 10 mM, $MgCl_2$ 10–12.5 mM, pH 7.0). To favour annealing of the two complementary strands, before every experiment the solution was heated and slowly cooled from 80 °C to 4 °C (ramp rate of −1 °C per 5 s) in a standard thermocycler (Bio-Rad CFX96 Real-Time System). Lysosensor Yellow/Blue DND-160 (stock 1 mM in anhydrous dimethyl sulfoxide) at a final concentration of 20 μM in aqueous solution was eventually added to the solution.

The replication reaction was performed using the Taq PCR Master Mix (QIAGEN) at 1× final concentration, primers forward and reverse 0.25 μM, SYBR Green I 2×, BSA 0.1%, DNA template 0.5 nM. The QIAGEN Master Mix 2× contains 3 mM $MgCl_2$, 20 mM Tris, KCl (concentration unspecified), $(NH_4)_2SO_4$ (concentration not specified), 400 μM of each dNTP and Taq DNA polymerase ($5\,U\,\mu l^{-1}$) and has a pH of 8.2 ± 0.1. For the reaction in the thermocycler, the protocol was as follows: initial heat activation at 95 °C for 3 min, 25 cycles of 90 °C for 5 s, 40 °C for 15 s and 60 °C for 15 s, then 4 °C for storage. For the reaction in the dew chamber, the same mixture was inserted after an initial activation step at 95 °C for 3 min. The temperature gradient was then applied and the gas phase was eventually enriched with 1 bar of CO_2. For replication of the 51-bp DNA, we used the following sequences (5′–3′): template DNA 51 bp, TTA GCA GAG CGA GGT ATG TAG GCG GGA CGC TCA GTG GAA CGA AAA CTC ACG, primer forward TTA GCA GAG CGA GGT ATG TAG GCG G, primer reverse CGT GAG TTT TCG TTC CAC TGA GCG T. For replication of the 47-bp and 77-bp DNA, we used the following sequences (5′–3′): template DNA 47 bp AGG AGG CGG ATA AAG TAG GAC CAC GGG AGT CAG GCA ACT ATG GAT GA, template DNA 77 bp TCA TCC ATA GTT GCG AGT GTA GAT ACG AGG GCT TAC CAG CGA GAC CCC AGT AAC CAA GTC TAC TTT ATC CGC CTC CT, primer forward TCA TCC ATA GTT GC, primer reverse AGG AGG CGG ATA AAG T.

The samples were run on a 12.5% denaturing (50% urea) polyacrylamide gel, with an acrylamide:bis acrylamide ratio of 29:1, solidified with TEMED (tetramethylethylenediamine) and ammonium persulfate. The replicated DNA samples were mixed with the gel loading dye blue (BioLabs, final concentration 2×) and loaded onto the gel wells. The samples were run in an electrophoretic chamber at 50 V for 5 min (alignment step) followed by 300 V for 15–20 min. The gel was then taken out and stained with SYBR Gold in TBE (Tris/Borate/EDTA) 1× for 5 min, and then imaged at the ChemiDOC MP (Bio-Rad) imaging station.

To prepare the replicated DNA for sequencing with Nanopore we used the following protocol. The DNA was end-repaired and 3′ A-tailed with NEBnext Ultra II repair and an A-tailing module (purchased from New England Biolabs) by incubation at 20 °C for 10 min and subsequent enzyme inactivation at 65 °C for 5 min. The DNA was then purified using magnetic beads (Beckman Coulter AMPure XP). A barcode adapter from the Oxford Nanopore barcoding kit (kit NBD104) was then ligated using the NEBnext Quick ligation module by incubation at 20 °C for 15 min. Barcode-ligated DNA was purified with Beckman Coulter AMPure XP magnetic beads. The barcoded samples were then pooled and ligated to the Oxford Nanopore sequencing adapter preloaded with a stalled motor protein. Ligation was performed with an NEBnext Quick ligation module by incubation at 20 °C for 15 min. The pooled sequencing library was purified with Beckman Coulter AMPure XP magnetic beads and eluted in elution buffer (EB) provided with the Oxford Nanopore sequencing kit. The eluted library was mixed with loading beads and sequencing fuel buffer (ONT sequencing kit LSK109) and loaded to a flowcell on a MinION sequencer. The flowcell was run for 24 h. The raw signals were converted to FASTQ sequence reads by ONT basecaller guppy v3.6.

Data availability

The data used in this paper are available in a public repository at https://doi.org/10.5282/ubm/data.258. Source data are provided with this paper.

Code availability

The analysis scripts used to analyse the data are available in a public repository at https://doi.org/10.5282/ubm/data.258.

Author contributions

A.I. performed the experiments, A.I. and M.A. performed the simulations and analysed the data. A.I. and P.W.K. analysed the sequencing data with Nanopore. A.I., M.A., U.G., C.B.M. and D.B. conceived the study, designed the experiments and the simulations and wrote the manuscript.

Competing interests

The authors declare no competing interests.

Additional information

Supplementary information The online version contains supplementary material available at https://doi.org/10.1038/s41567-022-01516-z.

Correspondence and requests for materials should be addressed to Dieter Braun.

Peer review information *Nature Physics* thanks Alexey Tkachenko, Elisa Biondi and Robert Endres for their contribution to the peer review of this work.

Reprints and permissions information is available at www.nature.com/reprints.

Supplementary information

Water cycles in a Hadean CO$_2$ atmosphere drive the evolution of long DNA

Water cycles in a Hadean CO_2 atmosphere drive the evolution of long DNA

Alan Ianeselli[1,2], Miguel Atienza[1], Patrick W. Kudella[1,2], Ulrich Gerland[2,3], Christof B. Mast[1,2] and Dieter Braun[1,2,*]

[1]Systems Biophysics, Ludwig Maximilian University Munich, Amalienstraße 54, 80799 München, Germany

[2]Center for NanoScience (CeNS), Ludwig Maximilian University Munich, Amalienstraße 54, 80799 München, Germany

[3]Physics of Complex Biosystems, Technical University of Munich, 85748 Garching, Germany

*Corresponding author: dieter.braun@lmu.de

Content:

Abbreviations

FRET, Förster Resonance Energy Transfer; T_m, temperature of melting; pCO_2, partial pressure of carbon dioxide; FAM, carboxy-fluorescein; ROX, carboxy-rhodamine; RNA, ribonucleic acid; DNA, deoxyribonucleic acid; PAGE, polyacrylamide gel electrophoresis; nt, nucleotides; bp, base pairs; A, adenine; T, thymine; C, cytosine; G, guanine; U, uracil.

1. Simulation of CO₂ absorption into dew and bulk

We simulated the dissolution of gaseous carbon dioxide into dew and bulk by solving the differential equations for the carbonate system, as well as the ones for the disodium phosphate buffering system. In our experiments, the concentration of gaseous CO_2 pressure was kept constant. Therefore, also in our simulation it was kept constant over time. Figure S1.1 shows a scheme of the carbonate and phosphate reactions.
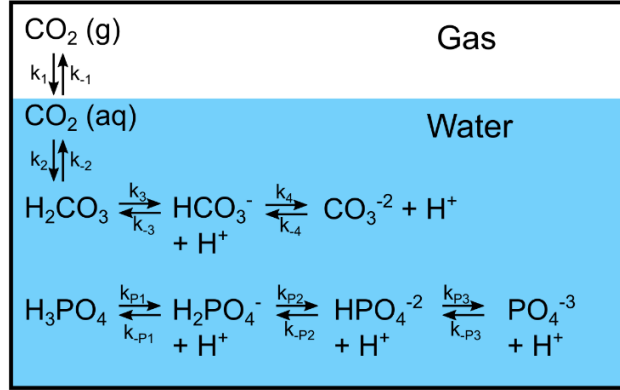

Figure S1.1: Absorption of CO₂ into water and chemical reactions of the carbonate and phosphate systems. Schematic representation of the simulated set of chemical reactions that occur when gaseous CO_2 is dissolved into an aqueous solution containing phosphate buffer. After its dissolution into water, the formation of the different carbonate species also releases protons. The phosphate species are a buffering system.

$$\frac{d[CO_2(g)]}{dt} = 0 \tag{1}$$

$$\frac{d[CO_2(aq)]}{dt} = k_1[CO_2(g)] - k_{-1}[CO_2(aq)] - k_2[CO_2(aq)] + k_{-2}[H_2CO_3] \tag{2}$$

$$\frac{d[H_2CO_3]}{dt} = k_2[CO_2(aq)] - k_{-2}[H_2CO_3] - k_3[H_2CO_3] + k_{-3}[H^+][HCO_3^-] \tag{3}$$

$$\frac{d[H^+]}{dt} = k_3[H_2CO_3] - k_{-3}[H^+][HCO_3^-] + k_4[HCO_3^-] - k_{-4}[H^+][CO_3^{--}] + k_{P1}[H_3PO_4] + k_{P2}[H_2PO_4^-] + k_{P3}[HPO_4^{-2}]$$
$$- k_{-P1}[H_2PO_4^-][H^+] - k_{-P2}[HPO_4^{-2}][H^+] - k_{-P3}[PO_4^{-3}][H^+] \tag{4}$$

$$\frac{d[HCO_3^-]}{dt} = k_3[H_2CO_3] - k_{-3}[H^+][HCO_3^-] - k_4[HCO_3^-] + k_{-4}[H^+][CO_3^{--}] \tag{5}$$

$$\frac{d[CO_3^{--}]}{dt} = k_4[HCO_3^-] - k_{-4}[H^+][CO_3^{--}] \tag{6}$$

2

$$\frac{d[H_3PO_4]}{dt} = k_{-P1}[H_2PO_4^-][H^+] - k_{P1}[H_3PO_4]$$

(7)

$$\frac{d[H_2PO_4^-]}{dt} = k_{-P2}[HPO_4^{-2}][H^+] - k_{P2}[H_2PO_4^-] + k_{P1}[H_3PO_4] - k_{-P1}[H_2PO_4^-][H^+]$$

(8)

$$\frac{d[HPO_4^{-2}]}{dt} = k_{-P3}[PO_4^{-3}][H^+] - k_{P3}[HPO_4^{-2}] - k_{-P2}[HPO_4^{-2}][H^+] + k_{P2}[H_2PO_4^-]$$

(9)

$$\frac{d[PO_4^{-3}]}{dt} = k_{P3}[HPO_4^{-2}] - k_{-P3}[PO_4^{-3}][H^+]$$

(10)

The differential equations shown above (1 – 10) were solved using the software COMSOL Multiphysics, using the rates and parameters indicated in table S1.1.

Parameter	Value	Description	Source
k_1	$1 \cdot 10^{-2}$ [s^{-1}]	CO_2 (g) $\longrightarrow$ CO_2 (aq)	Al-Hindi & Azizi[1]
k_{-1}	$12 \cdot 10^{-3}$ [s^{-1}]	CO_2 (aq) $\longrightarrow$ CO_2 (g)	
k_2	$6 \cdot 10^{-2}$ [s^{-1}]	CO_2 (aq) $\longrightarrow$ H_2CO_3	Bond et al.[2]
k_{-2}	$2 \cdot 10^1$ [s^{-1}]	$H_2CO_3 \longrightarrow CO_2$ (aq)	Pocker & Bjorkquist[3]
k_3	$1 \cdot 10^7$ [s^{-1}]	$H_2CO_3 \longrightarrow HCO_3^- + H^+$	
k_{-3}	$5 \cdot 10^{10}$ [M^{-1} s^{-1}]	$H^+ + HCO_3^- \longrightarrow H_2CO_3$	
k_4	$3 \cdot 10^0$ [s^{-1}]	$HCO_3^- \longrightarrow CO_3^{2-} + H^+$	Warneck[4]
k_{-4}	$5 \cdot 10^{10}$ [M^{-1} s^{-1}]	$CO_3^{2-} + H^+ \longrightarrow HCO_3^-$	
k_{P1}	$k_{-P1} \cdot 10^{-pK1}$ [s^{-1}]	$H_3PO_4 \longrightarrow H_2PO_4^- + H^+$	Keil et al.[5]
k_{-P1}	10^{13} [M^{-1} s^{-1}]	$H_2PO_4^- + H^+ \longrightarrow H_3PO_4$	
k_{P2}	$k_{-P2} \cdot 10^{-pK2}$ [s^{-1}]	$H_2PO_4^- \longrightarrow HPO_4^{-2} + H^+$	
k_{-P2}	10^{13} [M^{-1} s^{-1}]	$HPO_4^{-2} + H^+ \longrightarrow H_2PO_4^-$	
k_{P3}	$k_{-P3} \cdot 10^{-pK3}$ [s^{-1}]	$HPO_4^{-2} \longrightarrow PO_4^{-3} + H^+$	
k_{-P3}	10^{13} [M^{-1} s^{-1}]	$PO_4^{-3} + H^+ \longrightarrow HPO_4^{-2}$	
pK_1	2.12	1st dissociation constant	
pK_2	7.21	2st dissociation constant	
pK_3	12.67	3st dissociation constant	

Table S1.1: Parameters for the carbonate and phosphate chemical reactions.

Initial concentrations are reported in table S1.2.

Species	Initial concentrations
CO_2 (g)	$1.43 \cdot 10^{-5}$ [M] (ambient $pCO_2 = 4 \cdot 10^{-4}$ bar)
CO_2 (aq)	$1.17 \cdot 10^{-5}$ [M]
H_2CO_3	$3.52 \cdot 10^{-8}$ [M]
HCO_3^-	$2.61 \cdot 10^{-6}$ [M]
CO_3^{2-}	$5.82 \cdot 10^{-11}$ [M]
H^+	$2.69 \cdot 10^{-6}$ [M] (pH = 5.6)

Table S1.2: Initial carbonate concentrations after equilibration at room pCO_2. The concentration for each species (left column) is reported in the right column.

The following table contains the formulas to calculate the initial concentration of the phosphate species. The total phosphate concentration was 10 mM for the bulk and 0 mM for the dew.

Species	Initial concentrations
H_3PO_4	$[H_2PO_4^-] \cdot 10^{(-pH+pK_1)}$ [M]
$H_2PO_4^-$	$[HPO_4^{-2}] \cdot 10^{(-pH+pK_2)}$ [M]
HPO_4^{-2}	$[PO_4^{-3}] \cdot 10^{(-pH+pK_3)}$ [M]
PO_4^{-3}	$\frac{c_0}{(1+10^{(-pH+pK_3)})}$ [M]
c_0	0.01 (bulk) or 0 (dew) [M]

Table S1.3: Initial concentrations of the phosphate species. The formula for each species (left column) is reported in the right column.

The following Figure S1.2 shows an example of CO_2 acidification into the dew (total phosphate concentration 0 M). At an arbitrary time, the partial pressure of carbon dioxide was increased from ambient (0.4 mbar) to 1 bar, and then decreased to ambient again after the necessary equilibration time. The data that were obtained are consistent, both in terms of timescale and value, with experiments of carbon dioxide absorption and desorption[1] and equilibrium calculations based on equilibrium constants[6,7]. With a pH-sensitive fluorescent dye (Lysosensor Yellow/Blue DND-160), the pH change of pure water was measured experimentally. The data are shown in Figure S1.2a and clearly show the same behavior of the model. The slight positive slope of the experimental data is due to photo-bleaching of the Lysosensor fluorophore over time. To better visualize the data, we created the Bjerrum plot of our carbonate system model (Figure S1.3).
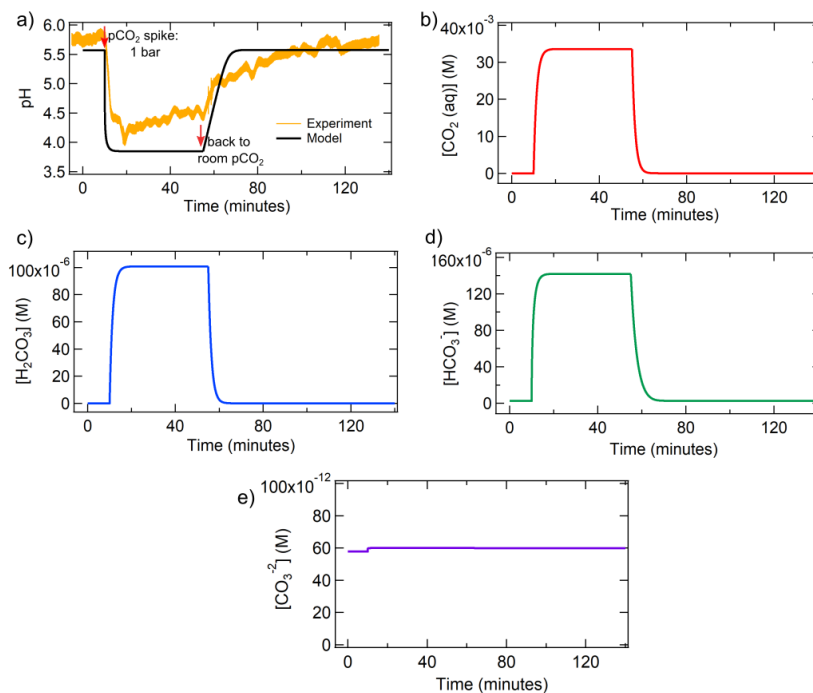
Figure S1.2: Kinetics of pH and carbonate in the dew after a CO_2 spike. pH (a), dissolved CO_2 (b), H_2CO_3 (c), HCO_3^- (d) and CO_3^{-2} (e) over time. The red arrows shown in a) indicate the moments of pCO_2 change: from ambient CO_2 to 1 bar (first arrow) and vice versa (second arrow), respectively.
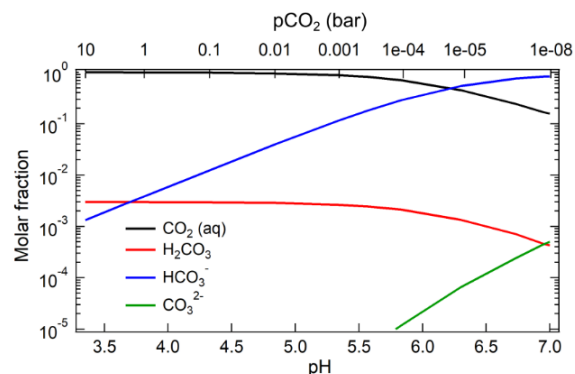
4

Figure S1.3: Simulated Bjerrum plot in the dew. a) Bjerrum plot: molar fraction of the carbonate species as a function of pH at steady state (assumed to be steady after 600 seconds of simulation). CO_2 partial pressures in the range from 10 µbar to 10 bar yielded a pH range from 7.0 to 3.3.

2. CO$_2$ dew chamber

Our reaction chamber (aka "dew chamber") consisted of a thin chamber (14 mm x 30 mm x 250 µm) made of Teflon, placed between a transparent sapphire window and a silicon back plate (the latter was covered with a thin Teflon foil). To establish a temperature gradient, we differentially heated the sapphire with rod resistors and the silicon plate with a Peltier element. The sapphire window included four holes, where microfluidic tubings were attached (see tubing numbers in Figure S2), in order to control the sample inflow and outflow to the chamber, to insert gaseous carbon dioxide and to measure the inner barometric pressure.
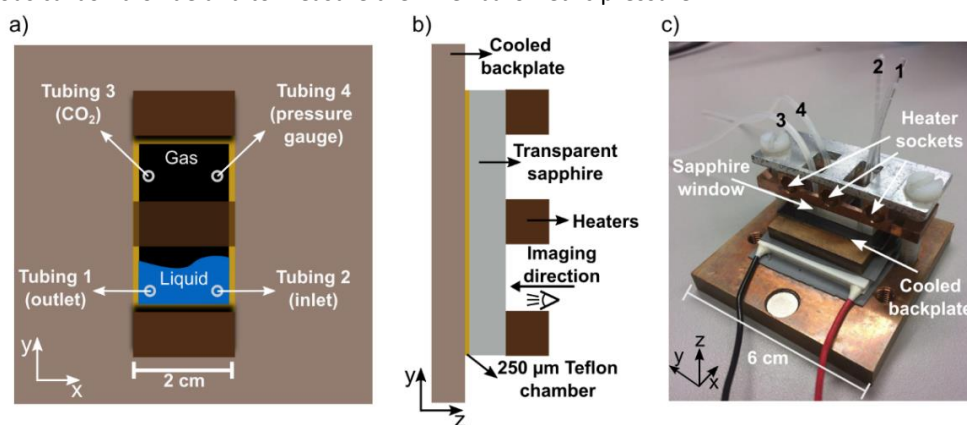

Figure S2. Scheme and photo of our microfluidic dew chamber. a) Front scheme of the chamber. b) Lateral scheme of the dew chamber. c) Photo of the dew chamber. The Peltier element can be seen below the back plate. Heaters (rod resistors) are inserted into the three heater sockets at the top of the chamber.

To produce a high pressure CO_2 atmosphere, we exploited the expansion properties of solid CO_2 upon sublimation. When dry ice changes its state from solid to gas, its volume increases about a factor of ~800. A bottle containing approximately 20 g of dry ice was connected to one of the tubings of our dew chamber. A handmade pressure regulator was connected to the bottle, which controlled an external vent and therefore the CO_2 flux inside the dew chamber. Upon sublimation, the 20 g of dry ice transformed into a volume of ~11 liters of gaseous carbon dioxide in a time span of approximately 30 minutes. The pressure was held constant to the final value, with an estimated accuracy of ± 0.05 bar. For the replication experiments, which required a carbon dioxide supply for several hours, the CO_2 gas was delivered using pressurized CO_2-containing flasks.

3. The dynamics of the RNA-rich dew

As already discussed in the main manuscript, the moving gas-water interface left RNA in the dry state on the warm sapphire, as a consequence of the so-called coffee-ring effect[8]. Fluorescent RNA in the dry state had a low quantum yield, and this was the reason why it could not be easily seen by fluorescence. When a droplet of dew, which nucleated on the cold side, became thicker than 250 µm (the thickness of our chamber) it touched the opposite warm sapphire, where the fluorescent RNA in the dry state was present. Therefore, it could re-dissolve RNA and become fluorescent again, as the quantum yield of the fluorophore increased. To get a deeper understanding of the droplet dynamics, we imaged our microfluidic dew chamber using a combination of bright field and fluorescence microscopy. The blue LED excited the FAM-labeled RNA, while a lamp homogeneously illuminated the chamber. The intensities of the light sources were adjusted in such a way to discriminate between the non-fluorescent, pure water dew on the cold side (that could be seen as dim shiny spheres) and the fluorescent dew, that re-dissolved the dry RNA on the warm side (which appeared very bright).
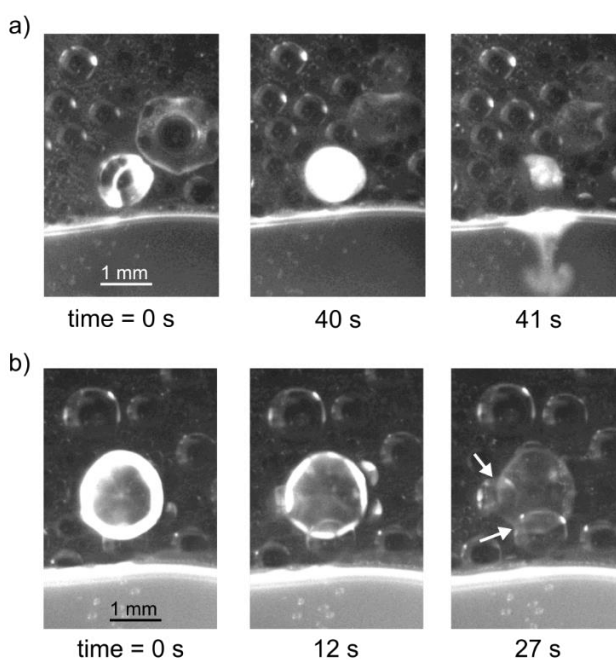

Figure S3: The two possible fates of a dew droplet. a) Growth and coalescence. The coalescence event could be seen by the fluorescent trace of the RNA left in the bulk (right picture). b) Evaporation and "jump" on the hot wall. The jump was confirmed by novel dew droplets of pure water that could be seen growing behind (indicated by the white arrows). Here, experimental conditions were the following: 250 µm (a) and 500 µm (b) chamber thickness, temperature gradient of 24 °C (cold side 15 °C, warm side 39 °C), and ambient CO_2 pressure. The solution consisted of 5 µM RNA (single stranded), 12.5 mM $MgCl_2$, 10 mM TRIS, pH 7.0.

A RNA-containing dew droplet could have two different fates:
(i) Growth and coalescence with the bulk. When other dew droplets grew in the proximity of the droplet of interest, they fused together. The size of the dew droplet increased, up to a point where it fell down or touched the bulk and coalesced with it. This transported the dissolved RNA back into the bulk solution. The dew droplets were the site of RNA denaturation. Therefore, the "coalescence fate" would periodically provide the reshuffling of RNA strands to the bulk solution where the replication reaction then could take place. The mechanism is shown in Figure S3a.
(ii) Evaporation and drying. As just discussed, when a dew droplet on the cold wall grew enough, it hit the warm sapphire. Due to the higher temperature of the sapphire, the dew droplet slowly started to evaporate, and RNA dried again. Initially, the droplet touched both the warm and cold sides (as a capillary bridge), and then eventually "jumped" on the sapphire. The dry fluorophore had a lower quantum yield. This made the RNA fluorescent signal disappear as the droplet evaporated. The mechanism is shown in Figure S3b. This mechanism was an efficient source of wet-dry cycles which were responsible for the unspecific polymerization reactions that we observed in our system.

6

4. Setup for FRET and pH measurements

To quantify the fraction of duplex RNA, we applied an alternating illumination protocol[9,10]. The two RNA strands were differentially labeled with FAM (Carboxy-fluorescein) and ROX (Carboxy-Rhodamine): a FRET pair. The first LED (blue) excited the donor (FAM) directly and the acceptor (ROX) could be excited only if the two dyes were within the FRET range. The second LED (amber) excited the acceptor only. The spatially-averaged, temperature-dependent, crosstalk- and artifact-corrected FRET signal was calculated as following[11]:

$$FRET(T) = \frac{DA(T) \cdot da(pCO_2) - dd(T) \cdot DD(T) - aa(T) \cdot AA(T)}{AA(T) \cdot aa(pCO_2)}$$

(11)

where *aa(T)*, *dd(T)*, *da(CO₂)* and *aa(CO₂)* corrected for non-FRET artifact signals in the DA and AA channels and were defined as:

$$dd(T) = \frac{DA_D(T)}{DD_D(T)} \qquad aa(T) = \frac{DA_A(T)}{AA_A(T)}$$

(12, 13)

$$da(pCO_2) = \frac{DA_D(pCO_2)}{DA_D(pCO_2^{ref})} \qquad aa(pCO_2) = \frac{DA_A(pCO_2)}{AA_A(pCO_2^{ref})}$$

(14, 15)

where *T* refers to temperature, *pCO₂* to the partial pressure of CO₂ and *pCO₂*ref indicates the reference pCO₂ condition (room pCO₂). Results are shown in Figure S4.1. All channels were defined according to table S4.
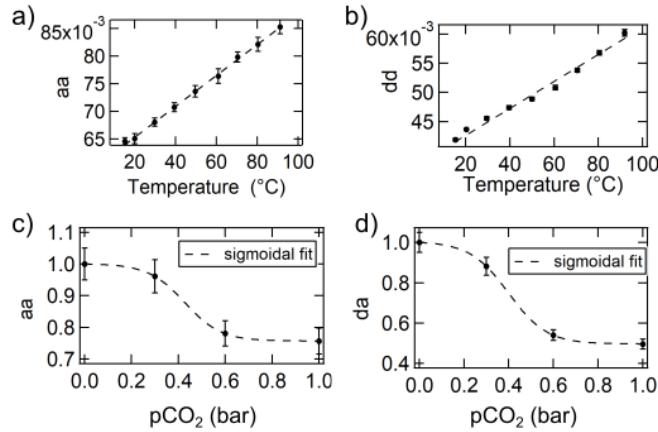
Figure S4.1: Correction of non-FRET artifacts. a-b) Crosstalk between the donor and acceptor channels calculated as a function of temperature and linearly fitted. c-d) Correction of CO₂-related artifacts in the range between 0 and 1 bar pCO₂.

Prior to every experiment, a melting curve in the bulk and at ambient pCO₂ was measured, in order to calculate the coefficients α=min(FRET(T)) and β=max(FRET(T))-α and normalize the FRET signal between 1 and 0:

$$FRET(T) = \frac{FRET(T) - \alpha}{\beta}$$

(16)

7

Channel	Excitation	Emission	Labelling
DA	FAM 470 nm	ROX 630 nm	FAM, ROX
DD	FAM 470 nm	FAM 536 nm	FAM, ROX
AA	ROX 590 nm	ROX 630 nm	FAM, ROX
AA_A	ROX 590 nm	ROX 630 nm	ROX
DD_D	FAM 470 nm	FAM 536 nm	FAM
DA_D	FAM 470 nm	ROX 630 nm	FAM
DA_A	FAM 470 nm	ROX 630 nm	ROX

Table S4: Definition of the channels for FRET calculation. The letters denote the excitation or emission wavelength. The index indicates which dyes are used (no index = both dyes are used). D = Donor (FAM), A = Acceptor (ROX).

We used the pH-sensitive ratiometric dye Lysosensor Yellow/Blue DND-160 to calculate the pH of the bulk and dew. From a stock concentration of 1 mM in DMSO, Lysosensor was diluted to a final concentration of 20 µM in aqueous solution. Through a modified Henderson-Hasselbach equation, the ratio R between the Lysosensor emission maximum at 540 nm upon alternating excitation at λ_1 = 329 nm and λ_2 = 384 nm was modeled by the following equation[12]:

$$pH = a + b \cdot \log\left(\frac{R - R_a}{R_b - R}\right)$$

(17)

where a denotes the pKa of Lysosensor, b accounts for the weighting of the emission spectra, R is defined as the ratio between fluorescence (F) emission at 540 nm upon excitation at λ_1 or λ_2 ($R=F_{\lambda 1}/F_{\lambda 2}$), and R_a and R_b account for the maximum and minimum fluorescence ratios, respectively. To correct for temperature-dependent shifts of the pH calibration curve, the parameters a, b, Ra and Rb have been fitted linearly in function of temperature, as shown in Figure S4.2. The calibration has been made in 10 mM Na⁺-citrate buffer at various pH (range 1.6 to 7), using Lysosensor at a concentration of 20 µM. 10 mM $MgCl_2$ were also added. Solutions with different pH have been created by ratiometrically mixing different amounts of powders of citric acid and sodium citrate dihydrate. Final pH has been adjusted by dripping HCl or NaOH.
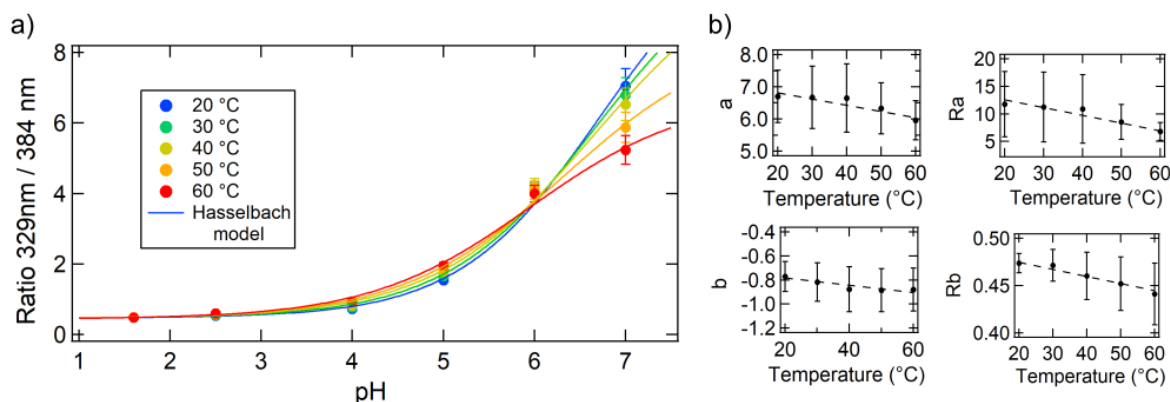
Figure S4.2: pH calibration curve of Lysosensor Yellow/Blue DND-160. a) Fluorescence ratio R measured between pH 1.6 - 7.0 and at different temperatures. The data have been fitted with the modified Handerson-Hasselbach equation (equation 17). b) The parameters *a*, *b*, *R*a and *R*b have been linearly fitted to adjust the temperature shifts of the Ratio to pH curve. Error bars in (a) indicate the standard deviation from experimental measurements (n ~ 10). Error bars in (b) indicate the standard deviation of the fit parameters.

The setup for FRET and pH consisted of a handmade standard fluorescence microscope (Zeiss Axiotech Vario microscope body) equipped with four excitation LEDs (M340L4, M385L2, M470L2, M590L2, from Thorlabs), excitation filters (BP 340/26, BP 379/34, BP 482/35, BP 588/20), beamsplitters (DC 475/40, DC 425 LP, DC 365 LP), a triple-edge dichroic mirror (DC 395/495/610), an Optosplit II with a ratiometric filter set (DC 600 LP, BP 536/40, BP 630/50), a Stingray-F145B ASG camera (ALLIED Vision Technologies GmbH) and a 1X objective (AC254-100-A-ML Achromatic Doublet). The former specifications regarding LEDs, filters, beamsplitters and dichroic mirrors were given in nanometers. The software LabVIEW was used to control the microscope's electronics. A scheme of the setup is given in the following Figure S4.3:

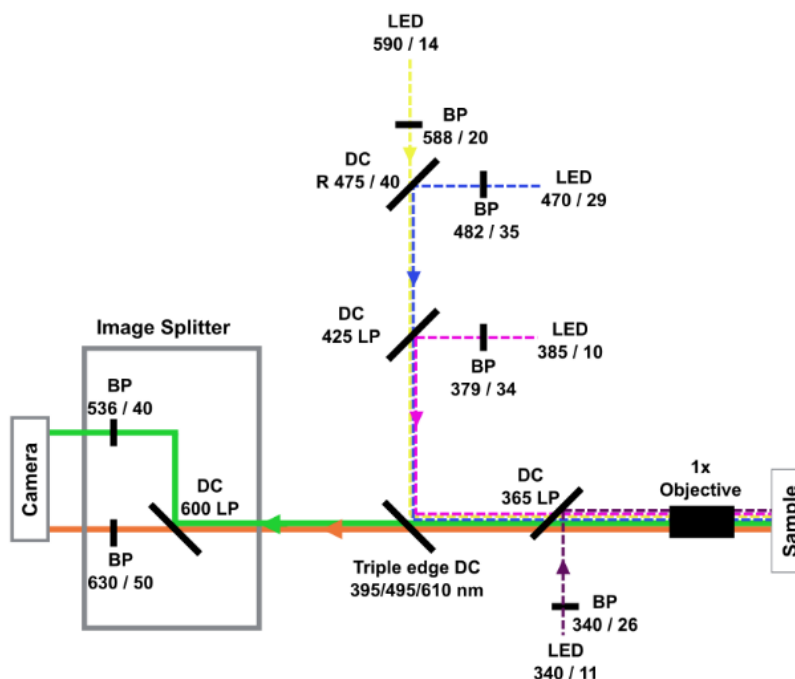**Figure S4.3: Scheme of the setup for FRET and pH measurements.** Four alternating LEDs have been used to excite FAM (blue LED), ROX (amber LED), and the two excitation maxima of Lysosensor (340 nm and 385 nm LEDs). Each LED was alternatively switched on for 100 ms. Therefore, the camera recorded four images per cycle. Together with the dead times, the camera frame rate was approximately 8 fps.

9

5. RNA hybridization model as a function of pH, salts, length and GC%

The stability of duplex oligonucleotides (RNA or DNA) in solution is determined by many factors. Intrinsic properties like sequence length and sequence composition play a crucial role, as well as environmental factors such as pH[13] and the concentration of ions[10] in solution. We modeled hybridization creating a model based on van 't Hoff to calculate the melting curve of RNA as a function of pH, Mg^{2+} concentration, sequence length and the GC content of the sequence. The van 't Hoff equation is the following:

$$\ln K_{\text{eq}} = -\frac{\Delta H}{RT} + \frac{\Delta S}{R}$$

(18)

where K_{eq} is the annealing equilibrium constant, ΔH and ΔS are the standard enthalpy and entropy changes, T is the temperature and R is the gas constant. The model has been calibrated on experimental melting curves measured by FRET. Given the melting curve for every specific condition (pH, Mg^{2+}, GC% and sequence length) the data have been converted in the form of equation 18 (van 't Hoff), and then fitted with a linear function to obtain $\Delta H/R$ and $\Delta S/R$. In order to calculate $\Delta H/R$ and $\Delta S/R$ in function of pH, Mg^{2+}, GC% and sequence length, only one parameter at a time has been changed, while the others remained constant. For what concerns pH and Mg^{2+}, $\Delta H/R$ and $\Delta S/R$ have been fitted with a power law, a linear fit was used in the cases of GC% and an exponential fit for sequence length. The results are shown in Figure S5.1.

The linear fits of the van 't Hoff plots shown in Figure S5.1 are based on the assumption that entropy and enthalpy are constant over temperature changes. This assumption is not always correct, but the predictions of the model resulted to be adequately accurate for many sequences of different lengths and composition, and for a large range of pH and $MgCl_2$ values, as shown in Figure S5.2. Therefore, the assumption of linearity is a good approximation for the type of calculations that we considered.

Given the enthalpic and entropic terms calculated and fitted as previously explained, it was then possible to calculate the equilibrium constant for each parameter at a given temperature. To obtain the final equilibrium constant of the model ($K_{\text{eq}}^{\text{total}}$), the individual enthalpies and entropies for each parameter have been put together to calculate the total enthalpy and the total entropy as following:

$$\Delta H_{total} = \frac{\Delta H(pH)}{\Delta H(pH_{ref})} \cdot \frac{\Delta H(Mg^{2+})}{\Delta H(Mg^{2+}_{ref})} \cdot \frac{\Delta H(length)}{\Delta H(length_{ref})} \cdot \frac{\Delta H(GC\%)}{\Delta H(GC\%_{ref})} \cdot \Delta H_{ref}$$

(19)

$$\Delta S_{total} = \frac{\Delta S(pH)}{\Delta S(pH_{ref})} \cdot \frac{\Delta S(Mg^{2+})}{\Delta S(Mg^{2+}_{ref})} \cdot \frac{\Delta S(length)}{\Delta S(length_{ref})} \cdot \frac{\Delta S(GC\%)}{\Delta S(GC\%_{ref})} \cdot \Delta S_{ref}$$

(20)

$$\ln K_{eq}^{total} = -\frac{\Delta H_{total}}{RT} + \frac{\Delta S_{total}}{R}$$

(21)

where ΔH_{ref} and ΔS_{ref} correspond to the reference enthalpy and entropy at the arbitrary reference condition of pH, Mg^{2+}, length and GC%. This means that the enthalpy and entropy of the (arbitrary) reference condition are multiplied by a factor between 0 and $+\infty$, and the final equilibrium constant is calculated according to equation (21) (van 't Hoff equation).
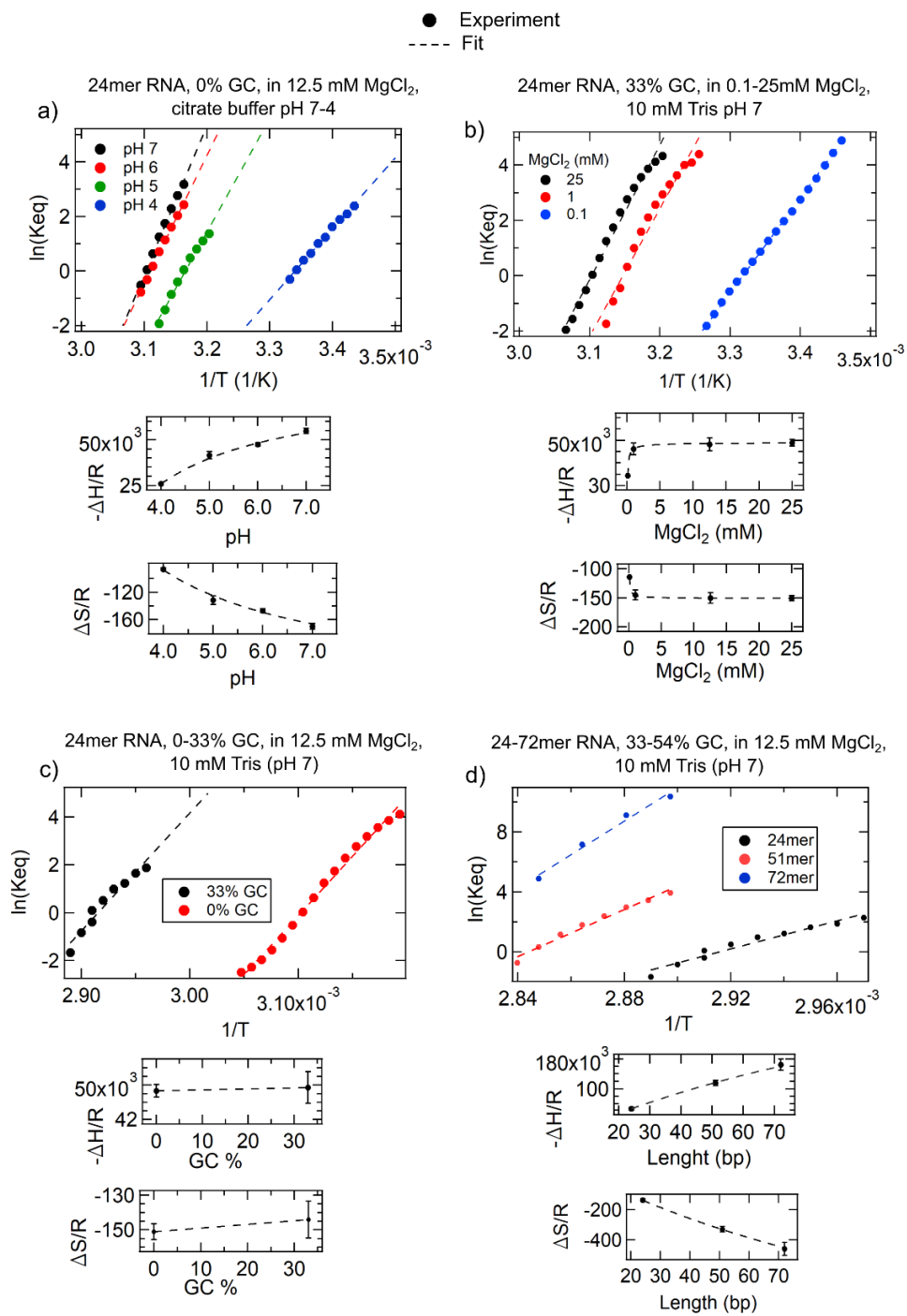
10

Figure S5.1: Experimental van 't Hoff plots used for the calibration of the model. RNA melting curves at different pH (a), Mg^{2+} (b), GC % (c) and sequence length (d), in the form of equation (18) (large plots), have been used to calculate enthalpy and entropy in function of the respective parameter (small plots). $\Delta H/R$ and $\Delta S/R$ have then been fitted with a power law (a and b), linearly (c) or with an exponential function(d).

With minimal discrepancies, the model successfully re-predicted the melting curves it was calibrated with, indicating that the method that we developed to put together the enthalpies and entropies is successful. Results are shown in Figure S5.2.
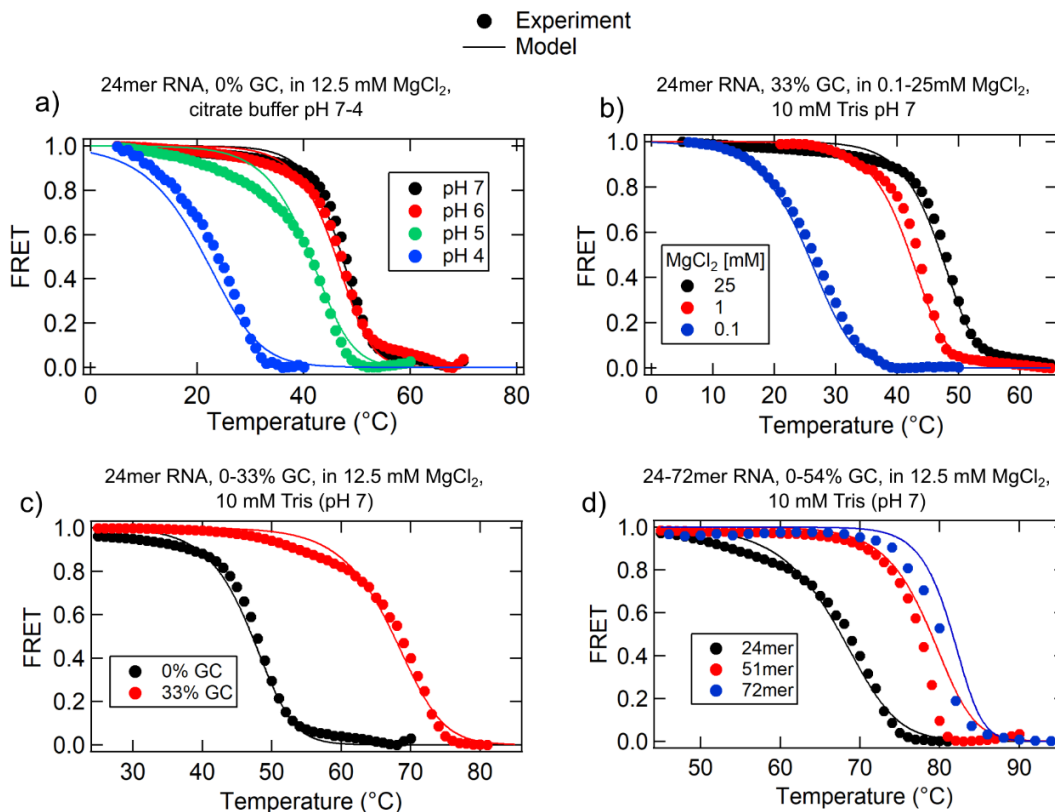

Figure S5.2: Experimental vs simulated melting curves. The experimental melting curves (points) at different pH (a), Mg^{2+} (b), GC % (c) and sequence length (d) have been compared to the melting curves calculated with our model (continuous lines). With only minor deviations, the experiment and the model show good agreement both in terms of the shape of the curve and the resulting melting temperature

The model described here has been used to obtain the data shown in Figure 2, e and Figure 5. By comparison with experimental data, it allowed us to determine the average salt concentration within the dew droplets, which resulted to be in the order of 0.25 mM MgCl$_2$.

This model helped us to better understand how the hybridization of oligonucleotides worked in a system of pH and salt fluctuations, where a water cycle at high pCO$_2$ continuously oscillated RNA between low-salt acidic dew droplets, and a pH-neutral salt-rich bulk. As already shown in Figure 2e and in the next Figure S5.3, the conditions of the bulk lied within a flatland region where the duplex oligo form is stable (this can be seen as a white/cyan surface (high T_m) in Figure S5.3, or as a yellow one (high FRET) in Figure 2e). On the other hand, the dew droplets lied outside of that flatland, after a circular boundary with a sudden drop in T_m and FRET. There, the duplex form became unstable. It is interesting to see that the shape of that boundary is not a square, but is rather circular. This indicates that the destabilizing effects of low pH and low salt concentration act synergistically.

The model is given in the supplementary file "*melting_curve_calculator.exe*"
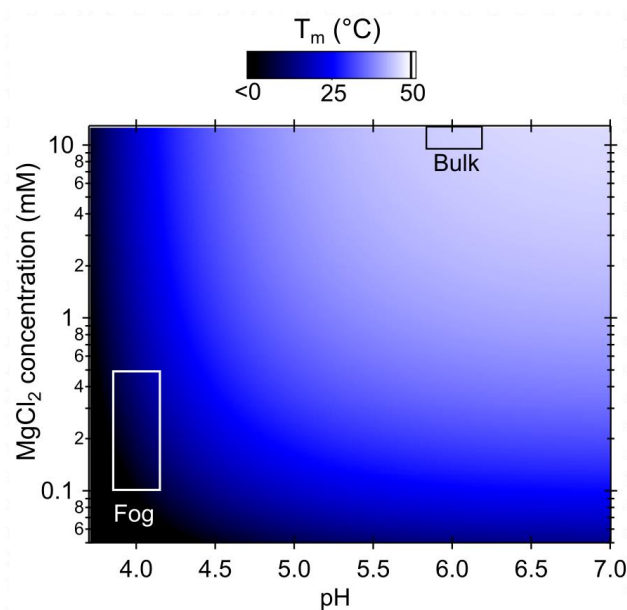
Figure S5.3: Surface plot of the simulated melting temperature. The surface plot shows how the melting temperature of a 24bp RNA, 0% GC varies as a function of pH and Mg^{2+}. The boxes inside of the plot indicate the existence regime of the bulk and of the dew droplets, when the gas contains 1 bar of pCO_2. This plot complements to the one shown in Figure 2e.

Using the hybridization model developed here, we could determine the stability of DNA or RNA in the bulk and dew as a function of pH. This helped us in estimating the pH range in which the dew and bulk maintain their denaturing and annealing characteristics, respectively. The concentration of Mg^{2+} is fixed at 0.25 mM in the dew and at 10 mM in the bulk. Results are shown in Figure S5.4, calculated in the conditions for the experiments shown in Figure 2d, 4a-c and 4d.
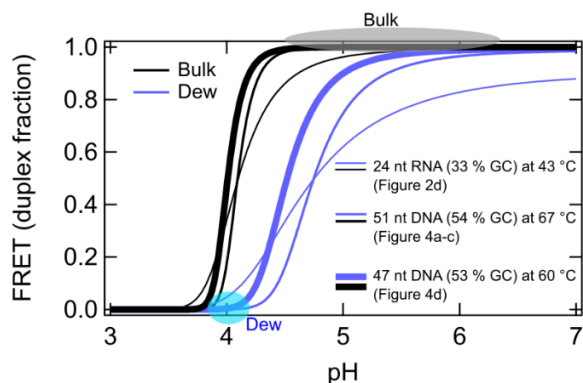

Figure S5.4: Duplex fraction as a function of pH in the dew and bulk. We calculated the duplex fraction of oligonucleotides for three different conditions: 24 nt RNA 33 % GC at 43 °C (thin lines), 51 nt DNA 54 % GC at 67 °C (medium lines), 47 nt DNA 53 % GC at 60 °C (thick lines), which correspond to the conditions of the experiments shown in Figure 2d, 4a-c and 4d, respectively. The colored circles generally indicate the expected pH of the dew (cyan circle) and bulk (gray ellipse) after CO_2 acidification. The bulk and the dew are micro habitats that have opposite effects on DNA stability, and can perform their functions also at higher temperatures.

Up to 67 °C, the dew always maintained denaturing conditions (FRET < 0.2) for pH up to ~ 4.2. The pH of low-salt water (i.e. dew) at 1 bar pCO_2 is supposed to remain below 4.0 for temperatures up to 80 °C[14]. Therefore, in the dew, the denaturation of the oligonucleotides that we used in our experiments was certain, and the assumption of a dew's pH of 4 for the calculations performed in Figure 5a-b was correct.

On the other hand, the bulk always retained duplex stabilizing conditions (FRET > 0.8) for pH down to ~ 4.3. An acidification of this magnitude is however not observed for buffered solutions at 1 bar pCO_2, which normally remain in a more neutral regime[15,16]. Therefore, the bulk is expected to retain annealing conditions also at the higher

13

temperatures of the experiments shown in Figure 3d, 4a-c, 4d. In fact, its duplex-stabilizing conditions are confirmed by the FRET measurements in Figure 3d and by the SYBR Green signal in Figure 4a-c, which only fluoresces in the presence of dsDNA.

According to Sigma-Aldrich, the pH of a Tris solution decreases of 0.25 pH units per 10 °C. We also measured that 1 bar of pCO_2 lead to a decrease in pH of 1.2 units (Figure 2a). The QIAGEN PCR Master Mix (which is buffered by 10 mM Tris) has an initial pH of 8.2. Summing the acidification induced by CO_2 and the temperature dependence of Tris, we obtain a pH of 6.0 at 67 °C and 1 bar pCO_2. At a pH of 6, a 100 % DNA duplex fraction in the bulk is expected (Figure S5.4, black lines).

6. Finite Element Simulation of DNA accumulation at the heated gas-water interfaces

We simulated our dew chamber using the software COMSOL Multiphysics®: an evaporating bulk and dew in a thermal gradient. The capillary flow, the convection and transport of solved DNA molecules were simulated. The simulated geometry (3D) was identical to our dew chamber (5 mm x 10 mm x 250 µm, x y z respectively). The bottom 2/3 of the chamber were filled with liquid and the top 1/3 contained air and a single dew droplet. The shape of the meniscuses of the dew were determined experimentally by imaging the dew chamber laterally (y-z plane) and measuring the contact angles of the dew droplet at the cold (Teflon) and warm (sapphire) sides (Figure S6a). The materials at the sides of the chamber (Teflon and sapphire) and the temperatures determined the contact angle of water on that surface. The same contact angles for the bulk (Figure S6b) have then been assumed. The shape of the dew and bulk in the x-y plane was also identical to what observed experimentally (Figure 3).

The temperature profile within the chamber was calculated through solving the partial differential equations for transient heat transfer, given the temperatures at the warm and cold sides (60 °C and 43°C respectively), while insulating the top and the bottom of the chamber. The temperature profile is shown in Figure S6c. Evaporative cooling was implemented by adding a boundary heat source at the air-water interface: $Q = H_{\text{vapor}} \cdot D_{\text{vapor}} \cdot \nabla c$ where H is the latent heat of vapor, D its diffusion coefficient, and c its concentration. The concentration profile of water vapor in the air was simulated by using a drift-transport diffusion equation:

$$\frac{\partial c}{\partial t} = \left(\frac{\partial^2 c}{\partial x^2} + \frac{\partial^2 c}{\partial y^2} \right) - u \frac{\partial c}{\partial x} - v \frac{\partial c}{\partial y}$$

(22)

As a boundary condition, the vapor concentration was fixed to saturation pressure at the air-water interface. The value of vapor concentration at the top of the chamber was a priori unknown, we therefore calculated this value experimentally by measuring the droplet evaporation rates (as discussed later).
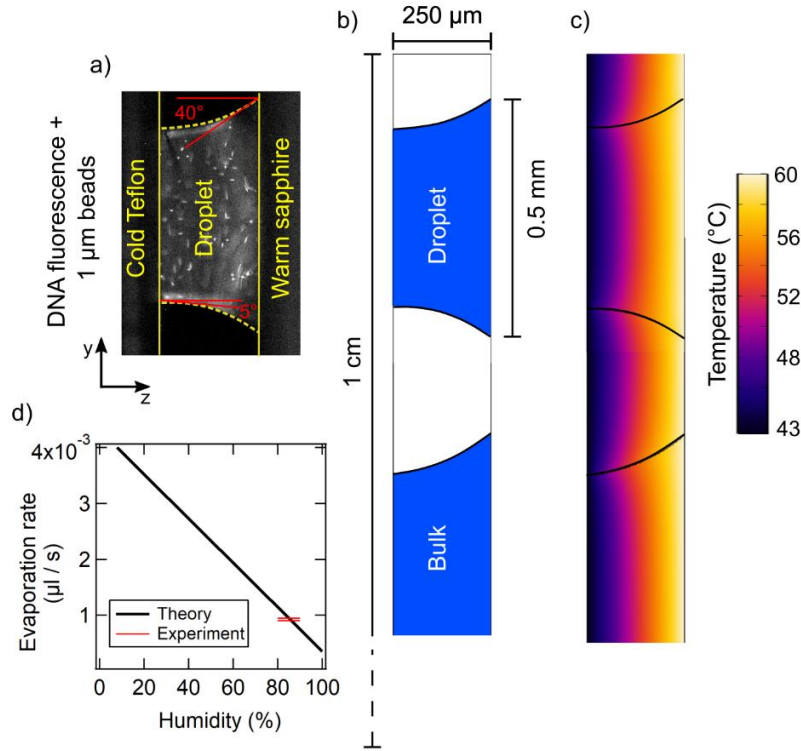
Figure S6. Measurement of droplet geometry and implementation of the dew chamber for simulation. a) Experimental picture used to obtain the lateral geometry of the dew droplets and the contact angles (red lines). The image was obtained by fluorescence microscopy, using FAM-labeled DNA (5 μM) and FAM-labeled beads 1 μm-sized. b) Geometry used in the simulation (y-z plane). c) Temperature gradient in our dew chamber (60 °C hot and 43 °C cold) calculated by finite element simulation. d) Evaporation rate in function of humidity. Comparing theory (black line) and experiments (red brackets) allowed us to deduce a humidity in the range of 80-90 % in our dew chamber.

As a result of the horizontal temperature gradient, the evaporation rate at the interface was stronger at the hot side than the cold side. Throughout the evaporation process, the interface maintained its geometrical shape, thus shrinking vertically downwards along the y axis. To compensate for the excess loss of water molecules at the warmer side of the interface, a capillary flow arose (the so-called coffee-ring effect[17]). We derived an expression for the velocity profile at the gas-water interface based on conservation of mass:

$$\vec{v} = \frac{-\rho}{M}\left(\vec{J}\cdot\vec{n}\right)\cdot\vec{n} - \Phi\vec{\tau}, \Phi_\tau = \frac{\Phi}{\int|\vec{\tau}|\cdot dS}$$

(23)

Where ρ is the density of water, *J* is the gradient of vapor concentration, *n* is the surface normal vector, *Φ* is the total evaporation rate, and tau τ is the vector along which the volume shrinks. The parameters *Φ* and τ were obtained experimentally. For the bulk interface, the volume shrank vertically along the y-axis, therefore $\tau = \hat{e}_y$. The capillary bridge shrank radially inwards, and therefore $\tau = \hat{e}_x + \hat{e}_z$ was a good approximation. The total evaporation rate *Φ* was obtained by experimentally investigating the change in volume of the droplet. The change in volume was linear in time, which is in good agreement with other research[18]. The experimental results were then compared to those obtained with a finite element simulation, and found these to be compatible with a humidity value at the top of the chamber in the range between 80-90%. Data are shown in Figure S6d.

The capillary and convectional flow profiles were obtained by numerically solving the Navier-Stokes equations for incompressible fluids. The convection flow was modeled by including the gravitation volume force as

15

the external force on the fluid. The capillary flow was implemented as a velocity profile at the gas-water interface. The accumulation of DNA was simulated using equation (22), where the velocities u and v were given by the sum of the liquid velocity and thermophoretic velocity: $D_T \cdot \nabla T$, where D_T is the thermophoretic mobility of DNA. The thermophoretic speeds were much slower than that of the liquid, therefore making the impact of thermophoresis on our experiments relatively weak. Diffusion, on the other hand, proved to be of great importance to our work. In particular, the length dependence of the diffusion coefficient of DNA explains why we observed a stronger accumulation of longer DNA strands than shorter ones. Moreover, our simulations showed a significantly greater accumulation at the bulk interface than in the droplet. This effect was attributed to the superposing of convective and capillary flows in the bulk. This effectively created a long range divergent flow, which had a large reservoir of molecules to accumulate. This means that a longer chamber could accumulate DNA molecules stronger.

All simulations were performed for a total time of 200 s, which was a reasonable length to assume the simulation to have reached a steady state. However, also in our dew chamber the lifetime of a droplet (in the range between 10 and 100 seconds) was usually shorter than the time needed to reach a complete steady state for DNA accumulation. After tens of seconds, a dew droplet was seen coalescing back in the bulk or completely drying on the hot sapphire. The simulation is given in the attached file "simulation_dew.mph".

To experimentally validate the results of the simulation, we performed dual-channel fluorescence imaging using differentially labeled DNA molecules of different lengths: FAM-labeled 8 nt ssDNA, ROX-labeled 51 nt ssDNA. The two strands were added at a final concentration of 1 µM in a solution of 10 mM $MgCl_2$, 10 mM Tris, at pH 7. The solution was then inserted into the thermal trap, and the same temperature gradient as the simulation of Figure 3 was applied ($\Delta T = 17$ °C: hot side 60 °C, cold side 43 °C). For matter of simplicity, the atmosphere has not been enriched with CO_2 (DNA convection and accumulation are independent of that anyway). The microscopy images have been obtained using the same imaging protocol shown in supplementary section 4, taking two consecutive images (FAM channel and ROX channel, 50 ms exposure time each), every 1 second. Results are shown in the following figure.
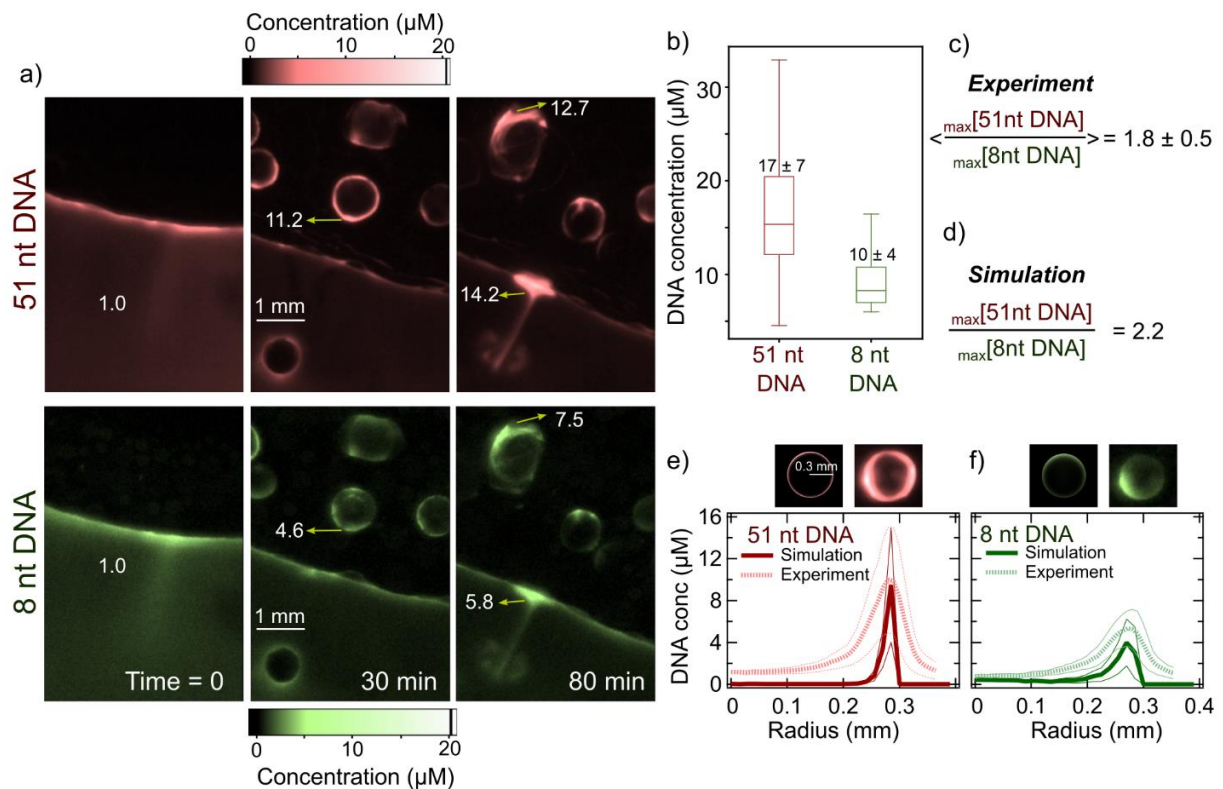
Figure S6.2. Longer DNA strands accumulate stronger at the gas-water interfaces. a) Dual-channel fluorescence images showing DNA accumulation in the bulk and fog, for a 51 nt DNA (ROX-labeled, top) and an 8 nt DNA (FAM-labeled, bottom), at different times. The numbers in the images correspond to DNA concentration. The 51 nt DNA accumulated much stronger than the 8 nt one. b) Quantification of DNA accumulation at the dew´s gas-water interface over the course of the experiment (~5000 frames, total duration ~ 1.5 hours). The average max fold increase in the concentration of 51 nt DNA over the 8 nt DNA results to be 1.8 ± 0.5 in the experiment (c) (n = 1513), and 2.2 in the simulation (d) (n=1). e) DNA concentration as a function of the droplet radius (circular average). Experiment (dashed lines) has been compared with the simulation (thick line). Thinner lines indicate the standard deviation. Qualitative pictures of the droplets of interest are shown on top (left = simulation, right = experiment. f) Same as (e) but for the 8nt DNA.

As shown in Figure S6.2a, in the heated rock pore DNA accumulates at the gas-water interface of the bulk and of the dew. The longer DNA (51 nt) accumulates stronger than the shorter one (8 nt). The average concentration of the 51 nt DNA at the dew´s gas-water interface is 17 ± 7 µM, against 10 ± 4 µM for the 8mer (n = 1513) (Figure S6.2b). At the brightest spot (i.e. most concentrated, indicated as "max") of the dew droplet, the concentration ratio between the 51 nt and the 8 nt resulted to be 1.8 ± 0.5 for the experiment (n = 1513) and 2.2 for the simulation (n = 1) (Figure S6.2c-d). The experimental and simulated DNA concentration profiles of the dew droplet (radially averaged) show an impressive agreement (Figure S6.2e-f). However, the simulated profile looks slightly narrower and sharper than the experimental one. This is probably attributed to the inevitable diffraction of light through the lenses and the optical path of the microscope. It is important to note that only one single droplet was selected for the profile analysis. In the experiment, however, many droplets of different size form over time, which pick up variable amounts of dried DNA. The final maximum DNA concentration at the dew´s gas-water interface is in fact very variable, as we showed in Figure S6.2b.

7. Sequencing of the longer DNA replication products

We sequenced the DNA products of the replication reaction in the CO_2 dew chamber shown in Figure 4d (6th lane), where two DNA templates of different lengths (47 bp and 77 bp) were replicated. Apart from the replication of the templates, also the formation of unexpected products has been observed. We sequenced them using the MinION Oxford Nanopore sequencing technology. The detailed protocol for DNA purification and preparation for sequencing is written in the material and methods. The sequencing procedure yielded 2856 reads. The length distribution of the reads is shown in Figure S7.1
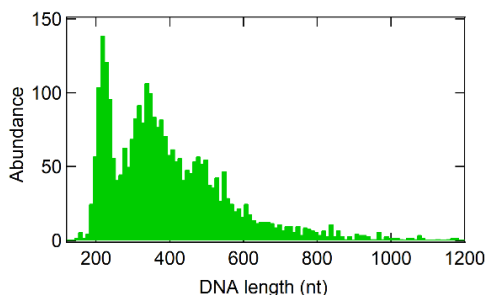

Figure S7.1: Length distribution of the reads generated by Nanopore sequencing.

The Levenshtein string distance[19] has been used to measure the distance between the reads and the templates and primers. It is defined as:

$$Lev_{a,b}(i,j) = \begin{cases} \max(i,j) & \text{if } \min(i,j) = 0, \\ \min \begin{cases} Lev_{a,b}(i-1,j) + 1 \\ Lev_{a,b}(i,j-1) + 1 \\ Lev_{a,b}(i-1,j-1) + 1_{(a_i \neq b_j)} \end{cases} & otherwise. \end{cases}$$

$$(24)$$

17

where $Lev_{a,b}(i,j)$ is the distance between the first *i* characters of the string *a* and the first *j* characters of the string *b*. $1_{(a\neq b)}$ is the indicator function, which equals 0 when $a_i=b_j$ and equals 1 otherwise. The result is a matrix of size *a*+1 × *b*+1 where the entries of the matrix indicate how many steps (character insertion, deletion or substitution) are required to convert one string into the other. The last cell of the matrix therefore indicates the distance between the strings *a* and *b*, i.e. the total number of steps that are necessary to completely convert *a* into *b* (or *vice versa*).

We calculated the Levenshtein distance for a specific sequence *a* (template or primer) mapped on the read *b*, looping over all possible substrings of length *a* of the read. This yielded a Levenshtein distance for the sequence in function of the read position, which was then converted into a probability in the following way:

$$Probability(a) = 1 - \frac{Lev_{distance}(a, b_{substring})}{Length(a)}$$

(25)

Some examples of the raw alignment data can be seen in Figure S7.2a-b. From the probability vs position plots we then reconstructed the sequence structure, as shown in Figure S7.2c-d.
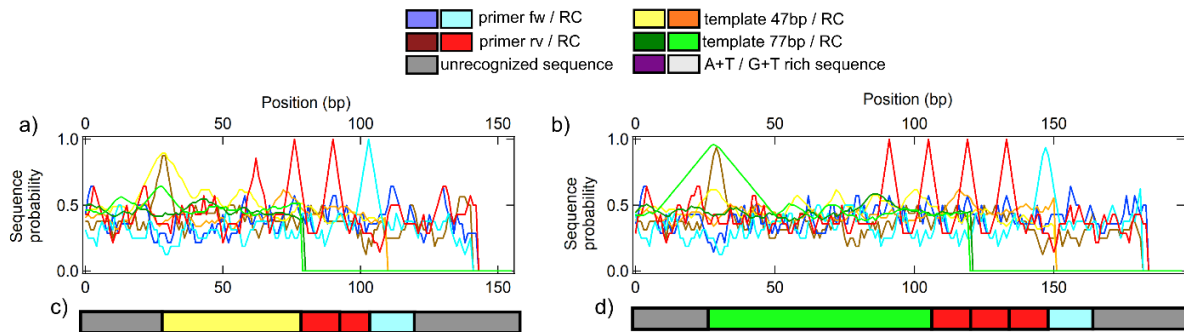

Figure S7.2: Analysis and reconstruction method of the sequences created in the dew. a-b) Raw data showing the probability of matching of every primer or template sequence as a function of the read position. A spike indicates the start of the match. c-d) Sequence reconstructed according to the plot shown above. RC = reverse complement.

Some sequences revealed to contain many repetitions of primers and templates (Figure S7.3a) attached one after the other, with a length distribution in the range between 150-300 nucleotides. These sequences correspond to the pink blob that can be seen in Figure 5a-b. Figure S7.3b shows the structure of the longer, AT rich sequences (the white pool of Figure 5a). They contain extended regions rich in As and Ts, and also eventually some primers and templates.

The whole analysis of the sequence alignments and reconstruction has been performed using LabVIEW.
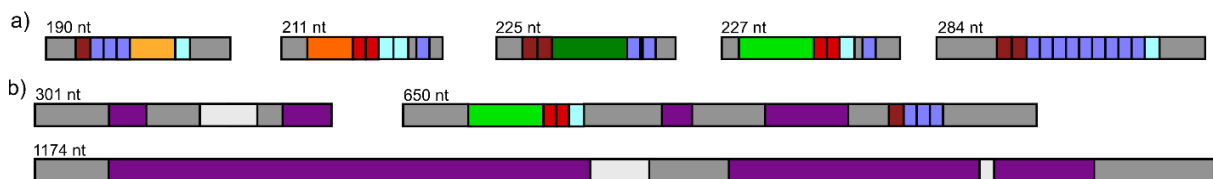

Figure S7.3: The CO$_2$ dew creates sequences with repeated primer/template patterns and very long AT rich ones. a) Examples of sequences that contain repetitive structures made of primers and templates. b) Long (300 - 1300 nt) DNA sequences that contain AT rich regions.

8. Modeling unspecific replication in the CO_2 dew droplets

In the experiments shown in Figure 5 we determined that the CO_2 dew droplets are able to replicate DNA and drive their evolution towards longer DNA sequences. Their sequence composition (indicated as AT:GC ratio) correlates with the denaturing conditions of the dew droplets. In particular, the long sequences that were replicated had an average duplex fraction (i.e. DNA FRET) of 0.14 ± 0.12.

We developed a probabilistic model to describe the replication and evolution of DNA sequences under the denaturing conditions of the CO_2 dew (acidic pH and low salts). The algorithm is shown in Figure S8.1.
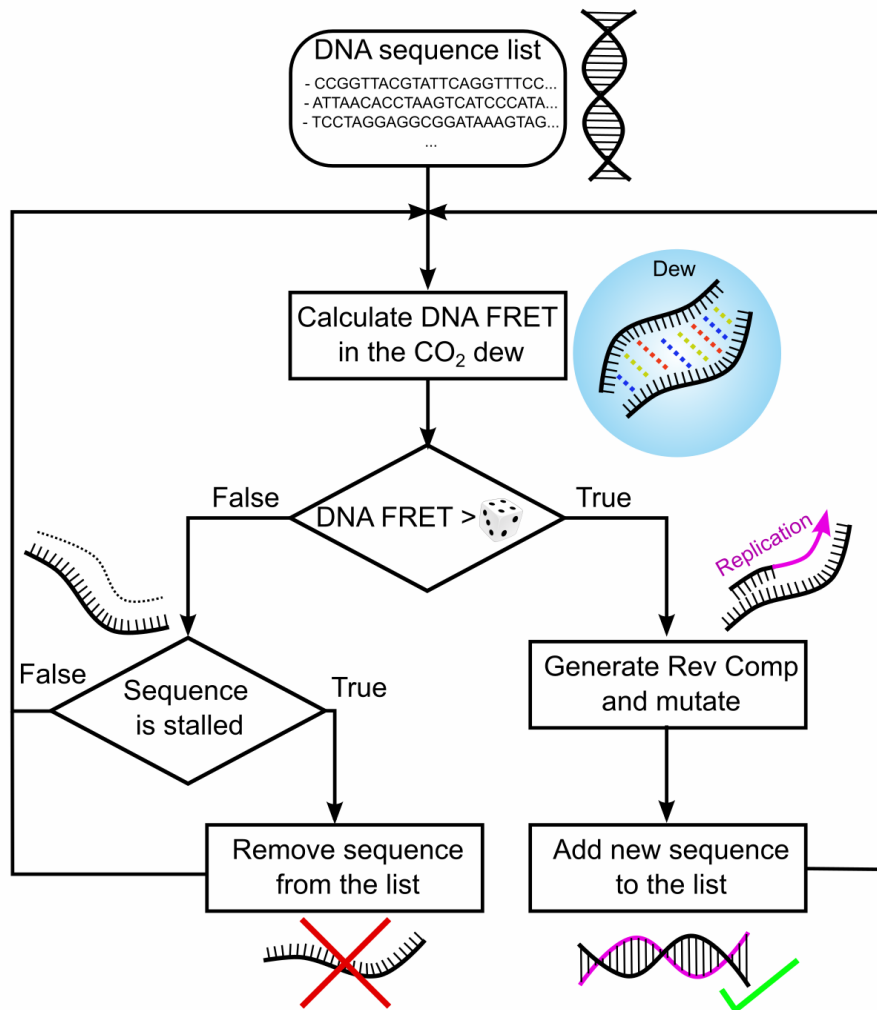

Figure S8.1: Algorithm of the stochastic replication model.

Every sequence in the pool has a probability of being replicated based on their duplex fraction, as indicated in Figure S8.2a (determined from the experiments, 0.14 ± 0.12). This introduces a selection pressure, resulting in the preferential replication of sequences with intermediate stability (FRET ~ 0.14). The sequences with a too high melting temperature (T_m) do not melt, and therefore do not provide single strands to initiate the next templated polymerization cycle. The sequences with a too low T_m remain in the single-stranded form and do not bind a template that can then be elongated via polymerization. In both cases, such sequences would stall and die out.

When a replication step is initiated, the reverse complement (RC) of the sequence is created. Then, a modification of the RC sequence takes place: it can be elongated or shortened. The probability of being elongated (p) vs being shortened ($1-p$) has been screened in Figure 5a-b (p from high to low: 1.0, 0.9, 0.84, 0.8, 0.7, 0.6), and

19

yields results similar to the experiment for 1.0≥*p*>0.5. Experimentally, the insertion or deletion of nucleotides may occur via processes such as unspecific annealing, hairpin formation and other self-templating processes[20]. A similar principle has been applied in our simulation. An elongation step consists of the insertion of a random submer of random length (between 0 and 15 nt, chosen with uniform probability) at a random position in the sequence. A shortening step consists of the deletion of a random part of the sequence of random length (again, between 0 and 15 nt, chosen with uniform probabilities). Moreover, at each step of elongation or shortening, a mutation rate on the sequences of 1e-4 mutations/nt has been introduced (this number corresponds to the error rate of the *Taq* polymerase enzyme[21]). The process is completely stochastic and therefore excludes any specific sequence bias that could have possibly been introduced by the polymerase enzyme in our experiments.

The size of the sequence pool was maintained constant at ~3000. When the size of the sequence pool exceeded that number (because of replication), the sequences were removed according to their propensity of being replicated: the sequences that stalled during the previous cycles of replication, because their T_m was too high or too low, were removed. This step emulates the sequences that die out during the replication process.
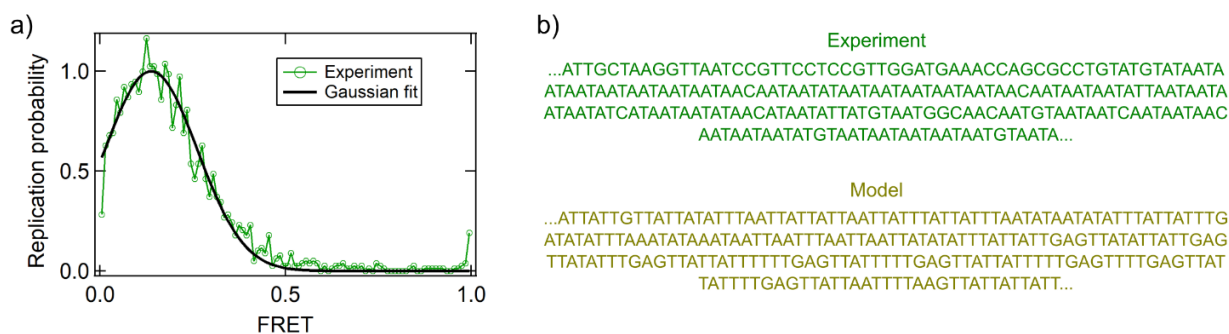

Figure S8.2: Model for the replication of sequences in the CO_2 dew. a) Replication probability as a function of DNA duplex stability (FRET). The highest replication probability occurs for FRET of 0.14 ± 0.12. Green data correspond to experimental data (Figure 5a), and they have been fitted with a Gaussian function (black line). b) Example of the sequences obtained in the experiment of DNA replication in the CO_2 dew (green) or using the replication model (yellow). Both sequences contain repeated AT rich motifs.

The simulation was run for about 100-150 steps, until the average sequence length distribution matched the reads observed experimentally in the CO_2 dew replication. A qualitative comparison is shown in Figure S8.2b and Figure 5. The sequences obtained by the simulation matched many features of the experiments. They were rich in A and T (A + T fraction > 80%), their submer composition showed a strong reduction in entropy and their final AT : GC ratio was determined by the denaturing conditions of the dew (with higher temperatures favoring sequences richer in GC). The model reproduced well what we observed experimentally. It provides a robust and enzyme-free confirmation of the general mechanism of how the CO_2 dew can drive the replication and evolution of DNA sequences.

The entropy of the sequences was calculated using the Shannon entropy (H), given a discrete variable *X* with possible outcomes x_1, …, x_n, that have probability P(x_1), …, P(x_n) to occur:

$$H(X) = -\sum_{i=1}^{n} P(x_i) \log P(x_i)$$

(26)

It was calculated over the submer counts shown in Figure 5c. P(x_i) corresponded to the normalized count (probability) of a specific submer (x_i) in the whole set (*n*) of submer combinations, with length *X*. In other words, the recurrence of each subsequence of given length was counted, and the probability of each submer was calculated. The entropy was then normalized on the random pool, in order to measure the relative change in entropy to the maximum possible entropy (which corresponds to the random pool).

9. List of attached files

supplementary_movie_1_fluorescent_droplets.avi
supplementary_movie_2_FRET_and_pH.avi
supplementary_movie_3_DNA_replication.avi
melting_curve_calculator.exe
simulation_file_dew.mph
source data for figures 2-5

10. References

1. Al-Hindi, M. & Azizi, F. Absorption and desorption of carbon dioxide in several water types. *Can. J. Chem. Eng.* **96**, 274–284 (2018).

2. Gillian M. Bond, *,† *et al.* Development of Integrated System for Biomimetic CO2 Sequestration Using the Enzyme Carbonic Anhydrase. (2001). doi:10.1021/EF000246P

3. Pocker, Y. & Bjorkquist, D. W. Stopped-flow studies of carbon dioxide hydration and bicarbonate dehydration in water and water-d2. Acid-base and metal ion catalysis. *J. Am. Chem. Soc.* **99**, 6537–6543 (1977).

4. Gordon, G. E. Chemistry of the Natural Atmosphere. Peter Warneck. Academic Press, San Diego, CA, 1988. xiv, 757 pp., illus. $85. International Geophysics Series, vol. 41. *Science* **242**, 121–2 (1988).

5. Keil, L. M. R., Möller, F. M., Kieß, M., Kudella, P. W. & Mast, C. B. Proton gradients and pH oscillations emerge from heat flow at the microscale. *Nat. Commun.* **8**, 1897 (2017).

6. Greenwood, N. N. & Earnshaw, A. *Chemistry of the elements*. (Butterworth-Heinemann, 1997).

7. Soli, A. L. & Byrne, R. H. CO2 system hydration and dehydration kinetics and the equilibrium CO2/H2CO3 ratio in aqueous NaCl solution. *Mar. Chem.* **78**, 65–73 (2002).

8. Deegan, R. D. *et al.* Capillary flow as the cause of ring stains from dried liquid drops. *Nature* **389**, 827–829 (1997).

9. Kapanidis, A. N. *et al.* Fluorescence-aided molecule sorting: Analysis of structure and interactions by alternating-laser excitation of single molecules. *Proc. Natl. Acad. Sci.* **101**, 8936–8941 (2004).

10. Ianeselli, A., Mast, C. B. & Braun, D. Periodic Melting of Oligonucleotides by Oscillating Salt Concentrations Triggered by Microscale Water Cycles Inside Heated Rock Pores. *Angew. Chemie Int. Ed.* (2019). doi:10.1002/anie.201907909

11. Mast, C. B., Schink, S., Gerland, U. & Braun, D. Escalation of polymerization in a thermal gradient. *Proc. Natl. Acad. Sci. U. S. A.* **110**, 8030–5 (2013).

12. Whitaker, J. E., Haugland, R. P. & Prendergast, F. G. Spectral and photophysical studies of benzo[c]xanthene dyes: Dual emission pH sensors. *Anal. Biochem.* **194**, 330–344 (1991).

13. Mariani, A., Bonfio, C., Johnson, C. M. & Sutherland, J. D. pH-Driven RNA Strand Separation under Prebiotically Plausible Conditions. *Biochemistry* **57**, 6382–6386 (2018).

14. Peng, C., Crawshaw, J. P., Maitland, G. C., Martin Trusler, J. P. & Vega-Maza, D. The pH of CO2-saturated water at temperatures between 308 K and 423 K at pressures up to 15 MPa. *J. Supercrit. Fluids* **82**, 129–137 (2013).

15. Liu, Q. & Maroto-Valer, M. M. Investigation of the effect of brine composition and pH buffer on CO2 -brine

21

sequestration. *Energy Procedia* **4**, 4503–4507 (2011).

16.   Holmes, J. D. *et al.* Buffering the Aqueous Phase pH in Water-in-CO2 Microemulsions. *J. Phys. Chem. B* **103**, 5703–5711 (1999).

17.   Deegan, R. D. *et al.* Capillary flow as the cause of ring stains from dried liquid drops. *Nature* **389**, 827–829 (1997).

18.   Carrier, O. *et al.* Evaporation of water: Evaporation rate and collective effects. *J. Fluid Mech.* **798**, 774–786 (2016).

19.   Levenshtein, V. I., Levenshtein & I., V. Binary Codes Capable of Correcting Deletions, Insertions and Reversals. *SPhD* **10**, 707 (1966).

20.   Park, D., Ellington, A. D. & Jung, C. Selection of self-priming molecular replicators. *Nucleic Acids Res.* **47**, 2169–2176 (2019).

21.   Potapov, V. & Ong, J. L. Examining sources of error in PCR by single-molecule sequencing. *PLoS One* **12**, (2017).

Appendix C

Paper 3: Protocells grow and divide inside microscale water cycles

Ianeselli, A.; Tetiker, D.; Stein, J.; Kühnlein, A.; Mast, C. B.; Braun, D.; Tang, D. T-Y.; Non equilibrium conditions inside rock pores drive fission, maintenance and selection of coacervate protocells. *Nature Chemistry* 2021 https://doi.org/10.1038/s41557-021-00830-y

OPEN

Non-equilibrium conditions inside rock pores drive fission, maintenance and selection of coacervate protocells

Alan Ianeselli[1,2], Damla Tetiker[1], Julian Stein[1,2], Alexandra Kühnlein[1,2], Christof B. Mast[1,2], Dieter Braun[1,2 ✉] and T.-Y. Dora Tang[3 ✉]

Key requirements for the first cells on Earth include the ability to compartmentalize and evolve. Compartmentalization spatially localizes biomolecules from a dilute pool and an evolving cell, which, as it grows and divides, permits mixing and propagation of information to daughter cells. Complex coacervate microdroplets are excellent candidates as primordial cells with the ability to partition and concentrate molecules into their core and support primitive and complex biochemical reactions. However, the evolution of coacervate protocells by fusion, growth and fission has not yet been demonstrated. In this work, a primordial environment initiated the evolution of coacervate-based protocells. Gas bubbles inside heated rock pores perturb the coacervate protocell distribution and drive the growth, fusion, division and selection of coacervate microdroplets. Our findings provide a compelling scenario for the evolution of membrane-free coacervate microdroplets on the early Earth, induced by common gas bubbles within heated rock pores.

ompartmentalization is a key feature of modern biological systems and has been hypothesized to play an important role during the origin of life by spatially localizing molecules and facilitating the first chemical reactions[1,2]. One viable route to compartmentalization is via liquid–liquid phase separation of oppositely charged polyelectrolytes in aqueous solution[3]. This process leads to the formation of membrane-free chemically enriched droplets. These coacervate microdroplets are intriguing protocell models as they form with little chemical identity under a broad range of physico-chemical conditions[4]; they localize and concentrate a range of different molecules[5–7] and exhibit molecular selectivity by partitioning[8–10]. In addition, coacervate droplets facilitate the assembly of fatty acid bilayers on their outer surface[11] and readily support catalytic reactions such as primitive RNA catalysis[12–14]. This provides a pathway to membrane-bound compartmentalization as observed in modern biology and a connection to the RNA–peptide world hypothesis.

Fusion events, division and maintenance of coacervate protocells would have been essential for the evolution of compartmentalized molecules. Fusion and growth of protocells are necessary for the exchange of molecules and genetic material[15] and it has been shown that the incorporation of free components by direct fusion with other protocells[16] or by external electric fields[17] can be achieved in a laboratory setting. In solution, these coacervate droplets will tend to coalescence, eventually forming a coacervate bulk macrophase[18,19], which limits their role as protocells. The division of coacervate protocells is required to transfer molecular information to succeeding daughter protocells that can pass evolutionary advantages to the next generation. To achieve division, modern cells make use of a complex machinery of regulatory proteins, scaffold proteins, enzymes and chemical messengers[20]. In the prebiotic world, division must have relied on other factors. Some studies suggest that division of lipid-based vesicles can be triggered by osmotic

changes[21], chemical changes[22], temperature[23] and shearing forces[24]. By comparison, less is known about the division mechanisms of membrane-free coacervate-based protocells that are chemically enriched. One theoretical study predicts that budding of chemically active membrane-free droplets is achieved by the flux of substrate and product across the interface which lies in a particular surface-tension regime[25]. Despite this prediction, there has been no experimental realization of fission of membrane-free protocells with or without chemical input. Furthermore, it has still not been experimentally shown how they would behave under prebiotically plausible non-equilibrium conditions.

To this end, pores in a thermal gradient provide a unique, facile and prebiotically feasible route to perturbing the system away from its equilibria[26]. Here, capillary flows induced by heat fluxes within millimetre-sized pores have been shown to accumulate molecules based on their size at the gas–water interface of gas inclusions. Simulations and experiments show that there are two main forces acting at the interface: capillary flows from the cold to the warm side and perturbative fluxes after the precipitation of water[27,28]. These forces induce rapid movements of particles, driving their contact and fusion. Under these conditions, lipid molecules accumulate at the interface to create vesicular structures and undergo fission driven by Marangoni flows and convection. These previous studies indicate that the growth, division and maintenance of coacervate droplets could be manipulated by the physical flows within thermal pores.

In this Article, we study the effect of out-of-equilibrium conditions provided by heated pores containing gas bubbles, a common primordial scenario[26], on the growth and division mechanisms of complex coacervate microdroplets formed by mixing polyanionic (carboxymethyl dextran (CM-Dex), adenosine 5′-triphosphate (ATP)) and polycationic (polydiallyldimethylammonium chloride (PDDA), poly-L-lysine (pLys)) species. Even though the coacervates

in this study might not be generated from prebiotically relevant molecules, they provide a robust model system for reconciling the general role of heat-induced out-of-equilibrium systems on coacervate microdroplets.

We show that the accumulation of coacervate-forming components at the gas–water interface of the gas bubble[28] drives growth by fusion of the coacervate microdroplets. Droplets of up to 300 μm in size are formed and maintained over time. This property is not observed under equilibrium conditions where droplets coalesce to eventually form a single coacervate macrophase (Supplementary Fig. 5.1)[18,19]. Intriguingly, the microfluidic water cycle induced by the thermal gradient[27] creates perturbative fluxes at the gas–water interface that lead to the fission and fragmentation of the coacervate droplets using purely physical processes (Fig. 1a–c). This offers direct evidence that physical forces within a confined environment are sufficient to provide the mechanism of membrane-free protocell division without complex machinery or targeted chemical reactions. Furthermore, the environment provided the ability to create and select for separate populations of droplets with different chemical composition. Specifically, the out-of-equilibrium conditions were able to overcome the intrinsic preference of RNA to coacervate with pLys (ref. [29]), yielding RNA:pLys droplets also enriched with CM-Dex at the gas–water interface. In the bulk, the coacervate droplets were formed mainly by RNA and pLys. This means that the thermal gradient, in combination with the gas bubble, led to the creation and spatial segregation of two different populations of coacervate droplets with different composition: oligonucleotide:polypeptide (RNA:pLys) coacervate droplets in the bulk and sugar:oligonucleotide:polypeptide (CM-Dex:RNA:pLys) droplets at the gas–water interface.

We present the proposed mechanisms as a prebiotic model for membrane-free protocell growth, division and evolution, since the only requirements are simple and ubiquitous physical conditions that could be found inside heated rock pores on the early Earth.

Results

The gas–water interface accumulates coacervate droplets and facilitates fusion.

To characterize the effect of non-equilibrium perturbations on coacervate microdroplets, we experimentally recreated a heated rock pore filled with liquid and gas bubbles as described previously[27,28]. In brief, a polytetrafluoroethylene (PTFE) sheet (250 μm thick) cut with sharp triangular structures was placed between an optically transparent sapphire and a silica plate (Fig. 2a). Liquids were loaded into the chamber through microfluidic tubes and gas bubbles were created by incomplete filling of the liquid into the triangular cavities (Fig. 2b). The sample chamber was loaded onto a custom-built microscope (Materials and Methods and Supplementary Section 1) and a temperature gradient was generated by differentially heating the sapphire with rod resistors inserted into a copper holder and cooling the copper back-plate through a connection to a water bath (Fig. 2c,d). The temperature gradients were varied between 15 and 29 °C with an accuracy of ±1 °C. Imaging was provided through the transparent sapphire with the camera focused on the cold wall. This chamber is also referred to as a "thermal trap".

Coacervate microdroplet dispersions were prepared by mixing negatively charged modified sugars CM-Dex (degree of polymerization between 50 and 100, with 1 carboxyl group every 3 repeats) or ATP, with positively charged polyelectrolytes, either pLys (degree of polymerization of 20 to 70) or PDDA (degree of polymerization of 90) (Fig. 2e). CM-Dex:PDDA and CM-Dex:pLys mixtures were prepared at molar ratios of 6:1 and 4:1, respectively, whilst ATP:PDDA and ATP:pLys droplets were prepared at molar ratios of 4:1. The molar ratios correspond to a [carboxyl] to [amine] ratio of 5 (CM-Dex:PDDA) or 7 (CM-Dex:pLys). Such ratios were optimized in previous work to yield a good amount of coacervation[11,30].

The total polymer concentrations were varied between 2 and 20 mM. The starting concentration dictated the density of coacervate droplets within the dispersion and the final amount of material accumulated at the gas–water interface. In order to visualize the coacervate droplets, we added 0.1% fluorescein isothiocyanate (FITC)-labelled CM-Dex or pLys. The coacervate dispersions were prepared in either 0.1 M Na+ bicine buffer (pH 8.5) or 10 mM Tris (pH 8) and 4 mM MgCl2. Control experiments showed that there was no appreciable difference between the two different buffers regarding the dynamics of the coacervate within the thermal trap (Supplementary Section 2). Therefore, we used both buffers interchangeably throughout our experiments to highlight the generality of our findings.

On loading the coacervate dispersion (20 mM CM-Dex:PDDA in 0.1 M Na+ bicine buffer, pH 8.5) into the thermal trap, microscopy images (taken every ~1 s) showed the presence of small coacervate droplets (<10 μm) evenly dispersed throughout the chamber (Fig. 3a). After differential heating at the two sides of the trap (warm side 49 °C, cold side 20 °C), the fluorescent droplets experienced convective flows in the bulk of the solution. The speed of the convective flow could be modulated by the temperature difference as observed in previous simulations[27]. Interestingly, we saw that the coacervate droplets in the bulk solution were transported by the convection flow to the gas–water interface where they accumulated and started growing by fusion (Fig. 3b,c and Supplementary Video 1). At the interface, the droplets moved parallel to the interface, driving contact and coalescence events. An individual fusion process between two coacervate droplets required a few seconds (from 1 to 10 s) and resulted in elliptically shaped coacervates. Figure 3d shows the process of fusion between three large coacervate droplets.

The growth of the coacervates over time was quantified from the optical microscopy images. Using LabVIEW, the average horizontal size was measured at different times (as depicted in Fig. 3b). Analysis showed that the CM-Dex:PDDA coacervates reached a maximal average size of 150 μm. Experiments with a different buffer (10 mM Tris, pH 8 and 4 mM MgCl2) or different polymers of different molecular weights (CM-Dex:pLys, ATP:pLys, ATP:PDDA or CM-Dex:pLys of higher molecular weight) showed comparable behaviour with minor differences in the final coacervate size (Fig. 3e and Supplementary Section 2). Note that, in our analysis, we only measured the horizontal size and not the whole volume of the coacervate droplet. Therefore, we believe that our method was not sensitive to small changes in size. This could be why there was no particular observable effect of the buffer or coacervate type on the final droplet size. However, the method was successful in calculating the average size distribution, as shown in Figs. 3e and 5j.

In addition, we characterized the effect of total polymer concentration on the growth rate and the final size of the coacervate droplets by performing a series of experiments with a constant thermal gradient (warm side 49 °C and cold side 20 °C), buffer conditions (4 mM MgCl2, 10 mM Tris, pH 8.0) and polymers (CM-Dex:PDDA molar ratio 6:1, [carboxyl]/[amine] = 5), doped with 0.1% FITC-labelled CM-Dex. The total polymer concentration was varied between 1 and 20 mM (a common concentration range that was used in other studies[12,18,31,32]). Immediately after inserting the coacervate solution in the thermal trap (<1 min), fluorescence microscopy images were taken every ~1 s. The images were analysed using ImageJ or LabVIEW to determine the growth rate and the average droplet size at steady state (after 1 h of thermal gradient) at the interface (Supplementary Section 3). The final droplet size and the growth rate did not seem to be significantly affected by the initial polymer concentration.

Also, we noticed that the variability in the size of the droplets between the experiments was large. This could be attributed to oscillatory salt fluctuations induced by the microscale water cycle, together with the intrinsic stochastic nature of droplet fusion. The
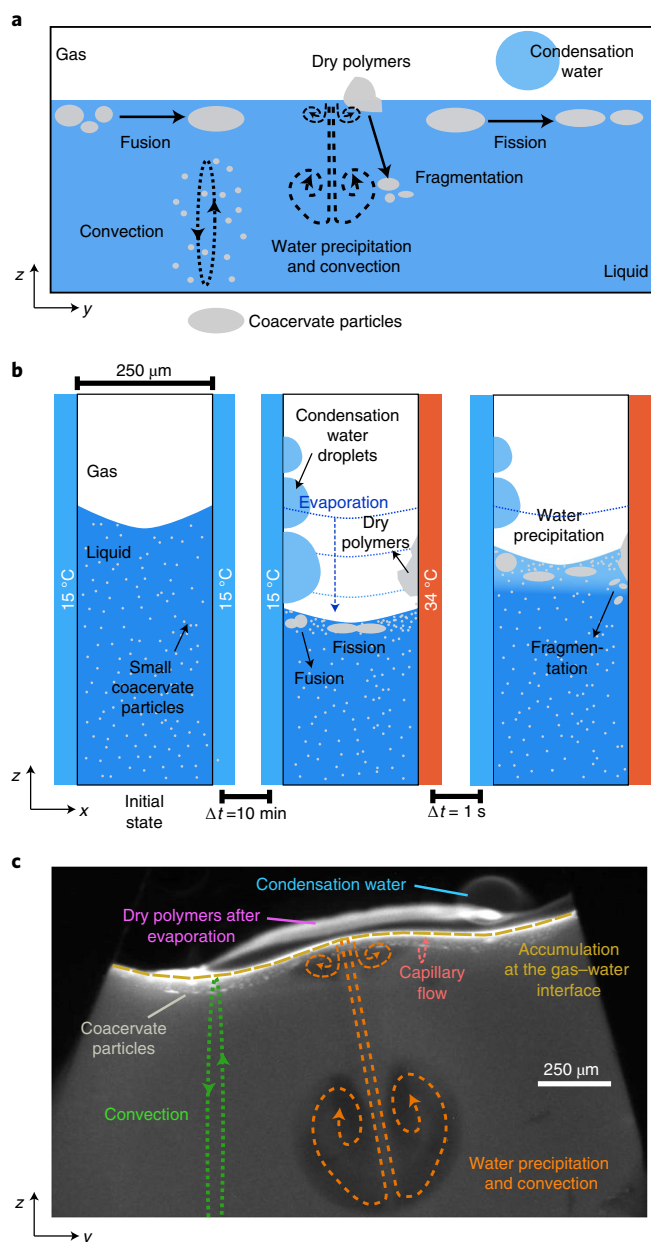
Fig. 1 | Fusion, division and transport of coacervate protocells inside a thermal pore. a, Scheme of coacervate transport, accumulation, growth and division at the gas–water interface, driven by convective flows, water condensation and subsequent water precipitation and convection. **b**, Left, scheme showing the thermophoretic pore in the absence of heating with pre-formed small coacervate droplets in the bulk. Centre, temperature gradient by differential heating across the pore with a gas bubble leads to water evaporation and a decrease in the water level that leads to dried polymers on the surface of the pore. Furthermore, droplet accumulation, fusion and fission are observed. Right, water precipitation drives coacervate fragmentation. **c**, Fluorescence image showing evaporation, water condensation, wet–dry cycles, convection and capillary flows at the gas–water interface of the thermal pore. Conditions for **c** were: CM-Dex:PDDA total polymer concentration 2 mM (molar ratio 6:1, [carboxy]/[amine] = 5) + 0.1% FITC-labelled CM-Dex, 10 mM MgCl$_2$, 10 mM Tris, pH 8, temperature gradient of 19 °C (warm side 34 °C, cold side 15 °C).

salt fluctuations induced by microscale water cycles in our thermal trap were previously characterized and showed periodic salt oscillations and perturbative flows caused by water precipitation[27].

While salts are known to have a major impact on coacervation[33,34], the effects of the salt oscillations on the coacervate droplets in the thermal trap do not appear to adversely affect the droplet stability, as the droplets stay intact at the interface. It is possible that the small fluctuations in salt concentration at the interface can induce local changes in the surface charge of the droplets, influencing droplet fusion and droplet composition. However, it is clear that the droplets are stable under these salt conditions. We estimated a ~1% change in the bulk salt concentration, accounting for the total volume within the pore versus the volume of water that takes part in precipitation. Therefore, the high variability in the sizes of the droplets and their composition that we observed during our analysis was likely to be due to the intrinsic stochastic nature of droplet fusion.

Despite this, in all instances (more than 50 different experiments that explored different coacervate conditions, starting concentrations and buffer conditions) we saw that the coacervate droplets accumulated and fused together, indicating that the accumulation, fusion and maintenance of the coacervate droplet at the gas–water interface are general phenomena driven by the forces in the thermal trap rather than the chemistry of the coacervate dispersion.

We also performed experiments with starting polymer concentrations below the critical coacervate concentration (CCC), ~1 mM for the CM-Dex:PDDA coacervate dispersions. At a starting concentration of 0.2 or 0.05 mM, no coacervate droplets were observed using optical microscopy within the resolution of our experiment, despite evident polymer up-concentration at the gas–water interface (Supplementary Section 3). Our results indicate that the thermal pore acts at the mechanical level to drive fusion of previously existing coacervate droplets, followed by droplet division by stretching or fragmentation and aggregation by wet–dry cycling.

We then wanted to verify that these observed phenomena were attributed to the gas–water interface in combination with thermal flows. To this end, we undertook two control experiments. The first determined the effect of convective flow alone, that is, in the absence of a gas bubble on the coacervate droplets. To do this, coacervate dispersions (CM-Dex:pLys, 2 mM, ratio 4:1, [carboxyl]/[amine] = 7, 10 mM Tris, pH 8.0, 4 mM MgCl$_2$) were loaded into a thermal trap without gas bubbles (warm side 49 °C, cold side 20 °C). Time-resolved optical microscopy images showed that the bulk coacervate droplets (<15 μm) were transported in the bulk by the convection flow at a speed of about $1.6 \pm 0.4\,\mu m\,s^{-1}$ but did not undergo fusion events in the bulk solution or accumulate within the trap (Supplementary Section 4). We then characterized the behaviour of coacervate droplets within the thermal chamber in the absence of thermal flow. At isothermal conditions, almost 100% of coacervate droplets within the pore slowly sedimented to the bottom of the microfluidic chamber, where the droplets fused to form a single coacervate droplet, as expected under isothermal conditions[18,19]. In the presence of the thermal gradient, the convection flow in the bulk prevented the coacervate droplets from sedimenting by maintaining them within the thermophoretic flow. The fraction of droplets that survived sedimentation was proportionally dependent on the thermal gradient. Steeper thermal gradients induced faster convection and prevented the sedimentation of a larger fraction of droplets. Finite element simulations of the sedimentation of the coacervate droplets in a thermal trap, with comparable thermal gradients to the experiments, showed that droplet sedimentation reached a steady state after 5 h and this was maintained for up to 30 h (Supplementary Section 5). In comparison, coacervate droplets at the gas–water interface resided at the interface even with very shallow temperature gradients.

Taken together, our results confirm that the flows at a gas–water interface led to the accumulation of coacervate droplets at the interface, fusion events between the droplets and to the maintenance of the droplets against sedimentation. In the absence of the thermal flow, the droplets will sediment to the bottom of the pore. Therefore,
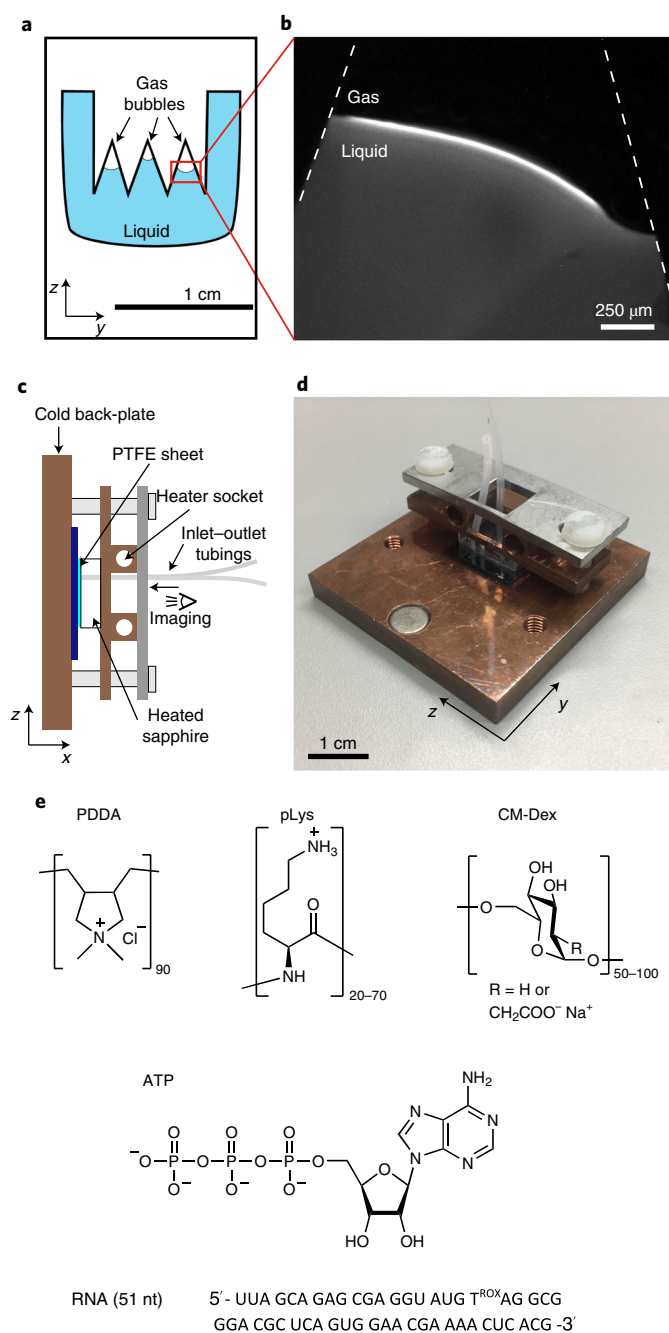
Fig. 2 | Description of the thermal trap used in the experiments. a, Schematic of the PTFE interspacer. The triangular structures cause the formation of gas bubbles on addition of buffer. **b,** Fluorescence image of the gas bubble and gas–liquid interface in a thermal trap with temperature gradient (CM-Dex:PDDA 6:1 ratio + 0.1% FITC-labelled CM-Dex, total concentration 2 mM). **c,d,** Lateral sketch (**c**) and photograph (**d**) of the thermal trap. The PTFE sheet with defined geometry was placed between a transparent sapphire and a cold copper back-plate. The sapphire was heated with rod resistors whilst the copper back-plate was cooled using a water bath to generate a temperature gradient. Aqueous solution was loaded and removed from the chamber by inlet and outlet tubings. **e,** Chemical structures of the components used: PDDA, pLys, CM-Dex, ATP, RNA sequence (51 nucleotides (nt)).

the combination of convection and capillary flow at the interface maintained the droplets at the gas–water interface or circulating within the bulk for extended periods of time.

Droplet division at the gas–water interface. Our data show that the opposing forces at the interface lead to the elongation of the droplets (Fig. 3c,d). As an elliptical shape has been associated with the initial stages of vesicle division[35] we wondered whether the forces in our non-equilibrium setting would be strong enough to drive the elliptical deformation of the membrane-free coacervate droplet into a fission event.

We applied a temperature gradient of 19 K (15–34 °C) on a coacervate dispersion of CM-Dex:PDDA (molar ratio 6:1, [carboxyl]/[amine] = 5, total polymer concentration 2 mM, 10 mM Tris, pH 8, 4 mM MgCl$_2$) doped with 0.1% FITC-labelled CM-Dex. Time-resolved optical microscopy images show that the coacervate droplets accumulated, fused and became elliptically elongated at the gas–water interface (Fig. 3c,d). Excitingly, on accumulation, droplets were progressively stretched along the interface until the droplet divided to produce two daughter protocells of a similar size (Fig. 4a and Supplementary Video 2). Our results confirm that elliptical deformation of the coacervate droplets at the interface do indeed drive droplet division. Droplet stretching and fission occurred as a consequence of the forces induced by the thermal gradient at the gas–water interface. In additional experiments, CM-Dex:pLys droplets also underwent fission events at the interface, indicating that this is a general phenomenon that is driven by the physical forces rather than the chemistry or type of coacervate (Supplementary Section 6).

In addition to convection and capillary forces at the interface, the presence of a gas bubble creates an environmental water cycle—this hypothetical prebiotic scenario may also have an effect on coacervate behaviour and properties. For example, wet–dry cycles can lead to the accumulation, drying and rehydration of molecules at a surface. Previous studies[27,28] have shown that a heated gas bubble in contact with a cold surface within a thermal trap will simulate a microfluidic water cycle. Pure water from the bulk solution will evaporate at the warm side and condense on the cold surface. These water droplets will grow in size and fall back into solution. The evaporation, water condensation and re-entry into the bulk solution leads to decrease (evaporation) and increase (rainfall) of the interface height. We therefore sought to determine how such wet–dry cycles and water precipitation would affect the coacervate droplets.

To do this, a dispersion of coacervate microdroplets (CM-Dex:PDDA, molar ratio 6:1, [carboxyl]/[amine] = 5, total polymer concentration 20 mM, 10 mM Tris, pH 8, 4 mM MgCl$_2$, doped with 0.1% FITC-labelled CM-Dex) was loaded into the thermal trap with a temperature gradient (warm side 34 °C, cold side 15 °C). Time-resolved optical microscopy images (Fig. 4b and Supplementary Video 3) show that coacervate droplets accumulated at the gas–water interface and stuck to the warm surface of the trap as the height of the interface decreased from water evaporation. This had the effect of driving the accumulated coacervates into a quasi-dry state on the surface. The dry polymers (see arrow in Fig. 4b) were later rehydrated and the perturbative fluxes induced by the water precipitation led to their fragmentation. The resulting smaller daughter droplets fell into the bulk and circulated with the convection flow. These results show that water cycles can drive the fragmentation and fission of coacervate droplets. Again, additional experiments with CM-Dex:pLys mixtures showed that this process is general and can also take place when different types of coacervate are used (Supplementary Section 6).

Despite this, fission events were rarely observed. Out of a total of 53 experiments (average duration of ~2 h each) which explored different polymer types, polymer concentrations, temperature gradients, buffers and trap geometries, we observed 12 division events. Of these 12 events, 10 of them consisted of division by fragmentation (the type of Fig. 4b). Two of them were of the type shown in Fig. 4a. However, the division events may be happening more frequently since we only image one of the many gas bubbles that were present
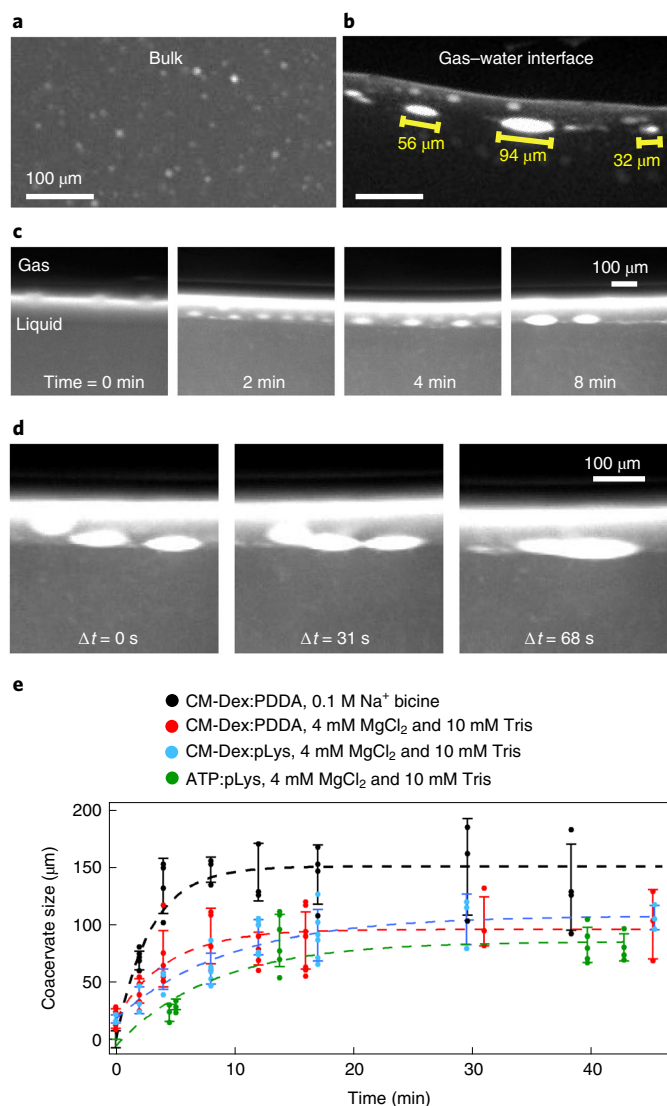
Fig. 3 | Coacervate droplets accumulate and fuse at the gas–water interface. a,b, Fluorescence microscopy images of coacervate droplets in bulk (**a**) and at the gas–water interface (**b**). On implementation of the thermal gradient, convective flows transport the coacervate droplets in the bulk to the gas–water interface where they fuse. Droplets will grow until they reach a steady-state size which is then maintained over time. **c,** Coacervate droplets at the interface (from left to right) at $t = 0$, 2, 4 and 8 min in a thermal gradient show progressive increase in droplet size. **d,** Microscopy images showing a fusion event between three coacervate droplets. **e,** Quantification of coacervate size over time for different buffer and coacervate compositions. Each data point represents the mean and standard deviation of approximately five different larger droplets at the gas–water interface. The dashed lines represent phenomenological exponential fits.

in the chamber. It is also important to note that our imaging protocol projected the view of the thermal trap on a 2D plane and was therefore not able to distinguish objects or observe any dynamics in the perpendicular axis. In Supplementary Section 7, we thoroughly analysed the experiment shown in Fig. 4a to rule out possible artifacts derived from the imaging.

Taken together, our results show two mechanisms by which the out-of-equilibrium behaviour induced by the thermal gradient at the gas–water interface of a microfluidic pore can drive droplet fission. This represents a viable route to coacervate fission and

subsequent evolution within the prebiotically plausible scenario of a thermal pore.

Furthermore, to determine how robust the behaviour within the pore was, we characterized the effect of different temperature gradients (values of ΔT between 10 and 60 K), trap thicknesses (between 127 and 500 μm) and the volume of the gas bubbles (between 0.005 and 50 mm³) on dispersions of coacervate droplets. Within these broad ranges of conditions, the features of coacervate accumulation, fusion, wet–dry cycles and divisions were observed. It appears that differences in these three parameters can affect the sedimentation and accumulation properties, fusion and division events and the quantity of dried polymers on the surface of the pore. For example, steep temperature gradients induce a fast convection in the bulk which prevents sedimentation and induces a fast capillary flow that promotes the fusion between the droplets. The increased wet–dry cycles also promote the division mechanism by fragmentation (Fig. 4b). On the other hand, droplet division by stretching would benefit from shallower temperature gradients, because the droplet needs to be slowly stretched in order to divide (Fig. 4a). In addition, steep temperature gradients will affect the size and frequency of water precipitations and, consequently, the extent to which the gas–water interface moves up and down during the evaporation/water condensation cycles that affect the quantity of dried polymers.

In summary, the general properties of accumulation, fusion and division, drying and coacervate re-entry are observed across a broad range of experimental conditions such as the temperature gradient, the chamber thickness and the gas-to-liquid ratio. Tuning these experimental parameters will tune the dynamic behaviour of the droplets in the pore. This provides exciting and plausible evidence that our observed phenomena of flow-induced droplet maintenance, accumulation, fusion and fission could have taken place within rocky environments of early Earth, which had pores of different sizes, incorporated bubbles of different dimensions and were subject to different thermal gradients.

Separation and selection of coacervate phenotypes. So far, we have determined the effect of the thermal trap with gas bubbles on coacervates prepared from modified sugars, peptides and synthetic polymers. Despite the fact that PDDA was unlikely as a prebiotic molecule, we observed the general phenomena of accumulation, fusion, maintenance and fission by different mechanisms which appear independent of the chemical properties of the coacervate (Supplementary Fig. 2).

Recent studies have shown that compartmentalization by coacervation[12,36] or the hydrophobic effect with fatty acids[37] could complement the RNA world hypothesis by providing the means to accumulate RNA and regulate RNA activity. Therefore, we wanted to determine the effect of the out-of-equilibrium dynamics of the thermal trap on dispersions of CM-Dex, pLys and RNA. To do this, dispersions of CM-Dex and pLys (molar ratio 4:1, [carboxyl]/[amine] = 7) with and without RNA (51 nt, single-stranded, Fig. 2e) were prepared at concentrations of 1.5 mM, 0.5 mM and from 0–5 μM respectively in 10 mM Tris, pH 8 and 4 mM MgCl₂. In order to study the co-localization between RNA, CM-Dex and pLys, dual-channel fluorescence imaging was used. RNA was labelled with ROX (carboxy-X-rhodamine) while 0.1% of the coacervate components (CM-Dex or pLys) contained a FITC label (see Fig. 5a). The microscope was equipped with an image splitter (Optosplit II) containing the filterset for FITC and ROX to enable dual-channel fluorescence imaging.

After loading the dispersions of CM-Dex and pLys with RNA into the sample chamber, dual-channel fluorescence imaging showed that pre-formed small coacervate droplets (size <15 μm) in the bulk colocalized RNA. Microscopy images showed that already prior to the thermal gradient, the droplets were rich in RNA and pLys with a weak signal attributed to CM-Dex. This indicates that RNA strongly
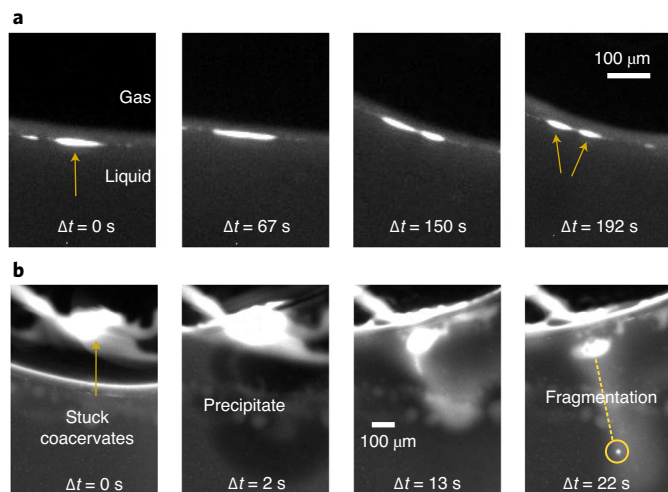
Fig. 4 | Fission of coacervates induced by interfacial forces and fluxes caused by water precipitation. a, Fission of a coacervate droplet into two smaller droplets, induced by interfacial forces at the gas–liquid interface. The initial droplet (yellow arrow) is slowly stretched (over a time frame of minutes) at the interface until it divides into two smaller droplets. **b**, Rehydration of coacervates stuck to the surface can induce fission by fragmentation, due to the perturbative fluxes caused by precipitating water. It induces a fast mixing of the dry polymers that eventually fragment.

competes with CM-Dex to form droplets with pLys. Indeed, thermophoretic measurements to obtain the binding constants between RNA with pLys and CM-Dex with pLys confirmed a higher affinity of RNA for pLys compared to CM-Dex (Supplementary Section 8). Fitting to the dose–response curve, we found that the dissociation constant (K_D) of the RNA:pLys complex ($K_D < 11$ nM) is an order of magnitude lower than the K_D of the CM-Dex:pLys complex (120 nM $< K_D < 400$ nM). This difference in K_D may be attributed to the fact that RNA has a higher charge density compared to CM-Dex. Therefore, whilst there is a small amount of CM-Dex within the droplet, CM-Dex will also be free in the coacervate dispersion. On inducing a thermal gradient (warm side 34 °C, cold side 15 °C), we observed the same phenomena as described previously, that is that coacervate droplets accumulate at the interface and fuse together. Interestingly, with the three coacervate components, dual fluorescence imaging of dispersions containing either FITC-labelled CM-Dex or pLys, with ROX-labelled RNA showed that the droplets at the interface were larger and contained all three components (CM:Dex, RNA and pLys) (Fig. 5a–c and Supplementary Video 4) whilst the droplets in the bulk remained small and rich in RNA and pLys (Fig. 5d–f). This observation is most likely to be due to the ability of the thermal trap to drive a strong accumulation of the RNA, pLys and CM-Dex in solution to the gas–water interface and induce an enrichment of the three components within the coacervate droplets, overcoming the equilibrium binding constants (Supplementary Section 8). Merging of the optical images shows that the microdroplets in the bulk have an overlap of the fluorescence signals of RNA and pLys (Fig. 5d–f and Supplementary Section 9).

These results are important as they show that the thermal pore can generate and select for two different populations of coacervate droplets with different chemical compositions at the gas–water interface and within the bulk solution, which has not been previously reported on.

We quantified the droplet size at the interface after applying the thermal gradient for 1 h using the methodologies already described and as a function of RNA concentration. We observed that the final size of the coacervate protocells at the gas–water interface

was inversely affected by RNA. In the presence of RNA, the average coacervate size dropped from 69 ± 31 μm down to 25 ± 9 μm (Fig. 5g–j and Supplementary Figure S8). As already shown in other studies[38], a higher charge density can lead to the formation of smaller coacervate droplets. This is in fact what we observed and we believe that this effect is driven by the stronger binding of RNA to pLys compared to CM-Dex to pLys.

The results show how the thermal trap can keep the coacervate droplets in a non-equilibrium state, enabling energetically unfavourable interactions at the interface. This permits the formation and selection of two different populations of droplets within the pore with different physical properties and different compositions. The results also show that the chemical composition of the coacervate droplets will affect their phenotype with smaller droplet size for increasing RNA concentration.

Discussion

We have shown that experimental primordial conditions—a millimetre-sized pore in a temperature gradient with a gas bubble—imparted specific selection pressures on dispersions of coacervate microdroplets. The thermal gradient across the pore drove a convection flow within the bulk solution and instigated the accumulation and growth of the coacervate droplets by fusion at the gas–water interface. The forces in the heated rock-like pores hindered the sedimentation of the coacervate droplets and the formation of large coacervate macrophases whilst permitting the maintenance of cell sized coacervate microdroplets for longer times. These droplets were elongated due to convection and capillary forces and underwent division after deformation at the gas–water interface. In addition, we observed division as a consequence of a water cycle within the gas bubble. The water precipitations induced the division and fragmentation of the coacervate material accumulated on the surface of the pore. These features were not observed in thermal traps in the absence of gas bubbles or at isothermal temperatures, indicating that this was a unique property of the thermal gradient and the gas bubble. This is a clear example of the accumulation, fusion, maintenance and fission of coacervate protocells. We have shown that this is a general phenomenon as we observed the same processes in coacervates with different chemical compositions and buffer conditions. These results represent a possible mechanism for the growth and division of membrane-free protocells on primordial Earth.

We have also shown that K_D determined the affinity of polyelectrolytes to form coacervates where oligonucleotides (RNA) had a higher propensity to form coacervates with polypeptides (pLys) compared to modified sugars (CM-Dex). The coacervate microdroplets that we studied seemed to be selective towards RNA (a molecule which can be catalytic) incorporation. In an origin-of-life scenario, this process could give a selective advantage in terms of catalysis within a pool of coacervate protocells. The thermal trap generated two different populations of coacervate droplets, where droplets poor in CM-Dex were maintained in the bulk solution whilst CM-Dex rich droplets formed and accumulated at the gas–water interface. This finding shows that the environment of a thermal trap with a gas bubble enables energetically unfavourable coacervate droplets to form by driving the system into an out-of-equilibrium state. As a consequence, the thermal trap was able to generate and contain populations of coacervate droplets which differ in chemical composition and size and therefore physical properties. In the presence of active RNA, these genotypic and phenotypic differences would be most likely to lead to different activities within the droplet. The droplets at the gas–water interface would benefit from additional variability and non-equilibrium properties: preferential enrichment of longer oligonucleotides[28], enhanced strand separation at lower temperatures[27] (and therefore lower hydrolysis rates) and enhanced RNA catalysis induced by the presence of an
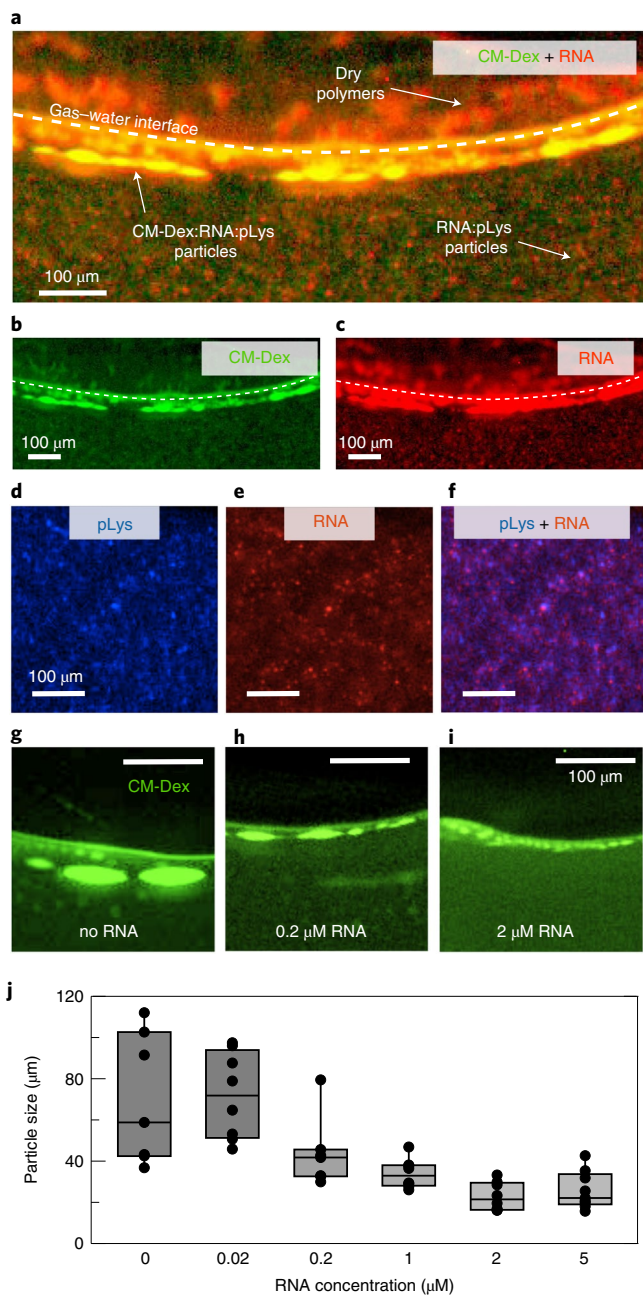
Fig. 5 | The thermal trap creates and separates two populations of coacervate droplets. a–c, Dual-channel fluorescence images of the CM-Dex:pLys:RNA coacervates in the thermal trap. CM-Dex and RNA were differentially labelled with FITC 0.1% and ROX 100%, respectively. The single pictures of the composite (**a**) are shown in **b** and **c**, respectively. Small droplets (<15 μm) enriched in RNA and pLys are formed in the bulk. Droplets enriched of all three components form instead at the gas–water interface. **d–f**, pLys channel (0.1% FITC-labelled) (**d**), RNA channel (**e**) and composite image (**f**), showing co-localization between RNA and pLys in the bulk droplets. **g–i**, no RNA (**g**), 0.2 μM RNA (**h**) and 2 μM RNA (**i**) showing the droplets at the gas–water interface (CM-Dex channel). **j**, Quantification of the size of CM-Dex:pLys droplets as a function of RNA concentration. The bars indicate the average size and standard deviation of nine different coacervate droplets.

additional polyanionic component that could lead to a change in material properties and the diffusion and reaction rates of RNA within the coacervate[39].

This has important implications for demonstrating how thermal fluxes could have driven an evolutionary selection pressure on coacervate microdroplets, giving experimental evidence for a key role within the origin-of-life scenario. In conclusion, our work has shown that a temperature gradient with a gas bubble generates a unique environment for the accumulation, fusion, fission and selection of coacervate microdroplets. We have shown that these characteristics have been made accessible by physical forces alone, without the chemical complexity or sophisticated machinery seen in modern biology. This makes the gas bubble within a heated rock pore a compelling scenario to drive the evolution of membrane-free coacervate microdroplets on early Earth.

Online content

Any methods, additional references, Nature Research reporting summaries, source data, extended data, supplementary information, acknowledgements, peer review information; details of author contributions and competing interests; and statements of data and code availability are available at https://doi.org/10.1038/s41557-021-00830-y.

References

1. Mason, A. F. et al. Mimicking cellular compartmentalization in a hierarchical protocell through spontaneous spatial organization. *ACS Cent. Sci.* **5**, 1360–1365 (2019).
2. Sokolova, E. et al. Enhanced transcription rates in membrane-free protocells formed by coacervation of cell lysate. *Proc. Natl Acad. Sci. USA* **110**, 11692–11697 (2013).
3. Oparin, A. I. *The Origin of Life* 2nd edn (Dover Publications, 1953).
4. Priftis, D., Laugel, N. & Tirrell, M. Thermodynamic characterization of polypeptide complex coacervation. *Langmuir* **28**, 15947–15957 (2012).
5. Koga, S., Williams, D. S., Perriman, A. W. & Mann, S. Peptide–nucleotide microdroplets as a step towards a membrane-free protocell model. *Nat. Chem.* **3**, 720–724 (2011).
6. Tena-Solsona, M. et al. Kinetic Control over droplet ripening in fuel-driven active emulsions. Preprint at *ChemRxiv* https://doi.org/10.26434/CHEMRXIV.9978539.V1 (2019).
7. Crosby, J. et al. Stabilization and enhanced reactivity of actinorhodin polyketide synthase minimal complex in polymer–nucleotide coacervate droplets. *Chem. Commun.* **48**, 11832 (2012).
8. McCall, P. M. et al. Partitioning and enhanced self-assembly of actin in polypeptide coacervates. *Biophys. J.* **114**, 1636–1645 (2018).
9. Nakashima, K. K., Vibhute, M. A. & Spruijt, E. Biomolecular chemistry in liquid phase separated compartments. *Front. Mol. Biosci.* **6**, 1–9 (2019).
10. Beneyton, T., Love, C., Girault, M., Tang, T. -Y. D. & Baret, J. High-throughput synthesis and screening of functional coacervates using microfluidics. *ChemSystemsChem* **2**, e2000022 (2020).
11. Tang, T.-Y. D. et al. Fatty acid membrane assembly on coacervate microdroplets as a step towards a hybrid protocell model. *Nat. Chem.* **6**, 527–533 (2014).
12. Drobot, B. et al. Compartmentalised RNA catalysis in membrane-free coacervate protocells. *Nat. Commun.* **9**, 3643 (2018).
13. Poudyal, R. R. et al. Template-directed RNA polymerization and enhanced ribozyme catalysis inside membraneless compartments formed by coacervates. *Nat. Commun.* **10**, 490 (2019).
14. Poudyal, R. R., Pir Cakmak, F., Keating, C. D. & Bevilacqua, P. C. Physical principles and extant biology reveal roles for RNA-containing membraneless compartments in origins of life chemistry. *Biochemistry* **57**, 2509–2519 (2018).
15. Santos, M., Zintzaras, E. & Szathmáry, E. Origin of sex revisited. *Origins Life Evol. Biospheres* **33**, 405–432 (2003).
16. Hanczyc, M. M. & Szostak, J. W. Replicating vesicles as models of primitive cell growth and division. *Curr. Opin. Chem. Biol.* **8**, 660–664 (2004).
17. Smith, A. E. & Chance, M. A. C. Coacervate behaviour in an alternating electric field. *Nature* **209**, 74–75 (1966).
18. Nakashima, K. K., Baaij, J. F. & Spruijt, E. Reversible generation of coacervate droplets in an enzymatic network. *Soft Matter* **14**, 361–367 (2018).
19. Mason, A. F., Buddingh, B. C., Williams, D. S. & Van Hest, J. C. M. Hierarchical self-assembly of a copolymer-stabilized coacervate protocell. *J. Am. Chem. Soc.* **139**, 17309–17312 (2017).
20. Schafer, K. A. The cell cycle: a review. *Vet. Pathol.* **35**, 461–478 (1998).

21. Beltrán-Heredia, E., Almendro-Vedia, V. G., Monroy, F. & Cao, F. J. Modeling the mechanics of cell division: influence of spontaneous membrane curvature, surface tension, and osmotic pressure. *Front. Physiol.* **8**, 312 (2017).

22. Zhu, T. F., Adamala, K., Zhang, N. & Szostak, J. W. Photochemically driven redox chemistry induces protocell membrane pearling and division. *Proc. Natl Acad. Sci. USA* **109**, 9828–9832 (2012).

23. Kudella, P. W. et al. Fission of lipid-vesicles by membrane phase transitions in thermal convection. *Sci. Rep.* **9**, 18808 (2019).

24. Pal, A. & Khakhar, D. V. Breakage of vesicles in a simple shear flow. *Soft Matter* **15**, 1979–1987 (2019).

25. Zwicker, D., Seyboldt, R., Weber, C. A., Hyman, A. A. & Jülicher, F. Growth and division of active droplets provides a model for protocells. *Nat. Phys.* **13**, 408–413 (2017).

26. Agerschou, E. D., Mast, C. B. & Braun, D. Emergence of life from trapped nucleotides? Non-equilibrium behavior of oligonucleotides in thermal gradients. *Synlett* **28**, 56–63 (2017).

27. Ianeselli, A., Mast, C. B. & Braun, D. Periodic melting of oligonucleotides by oscillating salt concentrations triggered by microscale water cycles inside heated rock pores. *Angew. Chem. Int. Ed.* **58**, 13155–13160 (2019).

28. Morasch, M. et al. Heated gas bubbles enrich, crystallize, dry, phosphorylate and encapsulate prebiotic molecules. *Nat. Chem.* **11**, 779–788 (2019).

29. Ukmar-Godec, T. et al. Lysine/RNA-interactions drive and regulate biomolecular condensation. *Nat. Commun.* **10**, 2909 (2019).

30. Moreau, N. G., Martin, N., Gobbo, P., Tang, T. Y. D. & Mann, S. Spontaneous membrane-less multi-compartmentalization: via aqueous two-phase separation in complex coacervate micro-droplets. *Chem. Commun.* **56**, 12717–12720 (2020).

31. Donau, C. et al. Active coacervate droplets as a model for membraneless organelles and protocells. *Nat. Commun.* **11**, 5167 (2020).

32. Love, C. et al. Reversible pH-responsive coacervate formation in lipid vesicles activates dormant enzymatic reactions. *Angew. Chem. Int. Ed.* **59**, 5950–5957 (2020).

33. Van Der Kooij, H. M. et al. On the stability and morphology of complex coacervate core micelles: from spherical to wormlike micelles. *Langmuir* **28**, 14180–14191 (2012).

34. Perry, S., Li, Y., Priftis, D., Leon, L. & Tirrell, M. The effect of salt on the complex coacervation of vinyl polyelectrolytes. *Polymers (Basel)* **6**, 1756–1772 (2014).

35. Urakami, N., Jimbo, T., Sakuma, Y. & Imai, M. Molecular mechanism of vesicle division induced by coupling between lipid geometry and membrane curvatures. *Soft Matter* **14**, 3018–3027 (2018).

36. Mountain, G. A. & Keating, C. D. Formation of multiphase complex coacervates and partitioning of biomolecules within them. *Biomacromolecules* **21**, 630–640 (2020).

37. Cornell, C. E. et al. Prebiotic amino acids bind to and stabilize prebiotic fatty acid membranes. *Proc. Natl Acad. Sci. USA* **116**, 17239–17244 (2019).

38. Vieregg, J. R. et al. Oligonucleotide-peptide complexes: phase control by hybridization. *J. Am. Chem. Soc.* **140**, 1632–1638 (2018).

39. Poudyal, R. R., Keating, C. D. & Bevilacqua, P. C. Polyanion-assisted ribozyme catalysis inside complex coacervates. *ACS Chem. Biol.* **14**, 1243–1248 (2019).

Methods

CM-Dex sodium salt (10–20 or 150–300 kDa, monomer: 191.3 g mol^{-1}), pLys hydrobromide (4–15 or 150 kDa, monomer: 208.1 g mol^{-1}) and PDDA (8.5 kDa, monomer: 161.5 g mol^{-1}), FITC-labelled pLys (15–30 kDa), FITC-labelled CM-Dex (15 or 150 kDa) and ATP (507.2 g mol^{-1}) were purchased from Sigma-Aldrich and were used without further purification. Stock solutions of each of the coacervate components were prepared to a concentration of 1 M in MilliQ water and stored at −20 °C until use. RNA oligonucleotides were purchased from biomers.net Gmbh, with HPLC purification and re-dissolved to a final concentration of 100 µM in nuclease-free water. The sequence was (51 bases): 5′-UUA GCA GAG CGA GGU AUG T^{ROX}AG GCG GGA CGC UCA GUG GAA CGA AAA CUC ACG-3′. Every RNA strand was labelled with a ROX molecule positioned centrally in the sequence attached to the backbone of a thymine and stored in pure nuclease-free water at a concentration of 100 µM.

The experiments were performed in a thin layer of PTFE (250 µm), which was cut with a defined geometry and then placed between a transparent sapphire and a copper back-plate. The geometry of the PTFE sheet was designed to induce the incorporation of gas bubbles as shown in previous work[27,28]. The sapphire was in contact with a copper placeholder which was heated with rod resistors. The copper back-plate was attached to an aluminium holder which was cooled with liquid water from a water bath (300F from JULABO). Temperature sensors (GNTP-SG from Thermofühler GmbH) were attached to the copper back-plate and to the copper sapphire holder to measure the outer temperatures of the cold and warm sides. The inner temperatures of the chamber were then calculated numerically, based on the outer temperatures, the heat conductivities of the materials (copper, silicon and sapphire) and their thickness. The outer warm target temperature was maintained constant via a PID loop implemented in LabVIEW, in order to control the output voltage to the rod resistors. The accuracy of the target temperatures was ±1 °C. The temperature differences that we used in the experiments shown here ranged from 15 to 30 °C.

Coacervate components were mixed together to the final desired concentration (2–20 mM) and immediately loaded into the microfluidic chamber. Dispersions of coacervates were prepared from either CM-Dex:PDDA or CM-Dex:pLys or CM-Dex:pLys:RNA in either 0.1 M Na$^+$ bicine buffer (pH 8.5) or 10 mM Tris and 4 mM MgCl$_2$ (pH 8.0). The chamber was then loaded onto a fluorescence microscope (Supplementary Section 1) which was focused on the cold wall and images were taken every 1–10 s for a certain timeframe (usually 1–2 h) using custom-built software written in LabVIEW.

Imaging was performed with a custom-built fluorescence microscope equipped with a blue light-emitting diode (470/29 nm), an amber light-emitting diode (590/14 nm), excitation filters (482/35 nm, 588/20 nm), a dual bandpass dichroic mirror (transmission edges at 505 and 606 nm), a 5× objective and an image splitter containing a longpass filter (600 nm) and emission filters (536/40 nm, 630/50 nm). This filterset allowed for the imaging of FITC and ROX respectively. The crosstalk between the channels was calculated following a standard protocol[27] (Supplementary Section 1). A Stingray-F145B ASG camera (ALLIED Vision Technologies Gmbh) was used to acquire images. The voltages to the light-emitting diodes and the camera were controlled with the LabVIEW software (a schematic of the microscope is shown in Supplementary Fig. 1). Image analysis of the droplets

was performed using ImageJ or LabVIEW. The raw data from the two different illumination channels were merged together to generate the composite dual fluorescence image.

Data availability

The datasets generated during and/or analysed during the current study are available via the following: https://doi.org/10.17617/3.6n.

Code availability

The code for the analysis of the particle sizes and for the dual-channel images is available via Edmond (the Open Research Data Repository of the Max Planck Society) at https://doi.org/10.17617/3.6n.

Author contributions

A.I., T.-Y.D.T., C.B.M. and D.B. designed the study. A.I., T.-Y.D.T., J.S. and A.K. performed the experiments. A.I. analysed the data. A.I., T.-Y.D.T., J.S., A.K., C.B.M. and D.B. wrote the manuscript.

Competing interests

The authors declare no competing interests.

Additional information

Supplementary information The online version contains supplementary material available at https://doi.org/10.1038/s41557-021-00830-y.

Correspondence and requests for materials should be addressed to Dieter Braun or T.-Y. Dora Tang.

Peer review information *Nature Chemistry* thanks the anonymous reviewers for their contribution to the peer review of this work.

Reprints and permissions information is available at www.nature.com/reprints.

Supplementary information

Non-equilibrium conditions inside rock pores drive fission, maintenance and selection of coacervate protocells

In the format provided by the authors and unedited

1   **Non-equilibrium conditions inside rock pores drive fission, maintenance and**
2   **selection of coacervate protocells**

3   Alan Ianeselli[1,2], Damla Tetiker[1], Julian Stein[1,2], Alexandra Kühnlein[1,2], Christof B. Mast[1,2], Dieter Braun[*,1,2]
4   and T-Y Dora Tang[*,3]

5   [1]Systems Biophysics, Ludwig Maximilian University Munich, Amalienstraße 54, 80799 München, Germany
6   [2]Center for NanoScience (CeNS), Ludwig Maximilian University, Amalienstraße 54, 80799 München, Germany
7   [3]Max-Planck Institute for Molecular Cell Biology and Genetics, Pfotenhauerstraße 108, 01307 Dresden, Germany
8   [*]Corresponding authors: tang@mpi-cbg.de, dieter.braun@lmu.de
9

10   **Supplementary information table of content:**

11

26
27
28
29
30
31
32
33
34
35
36
37
38
39
40
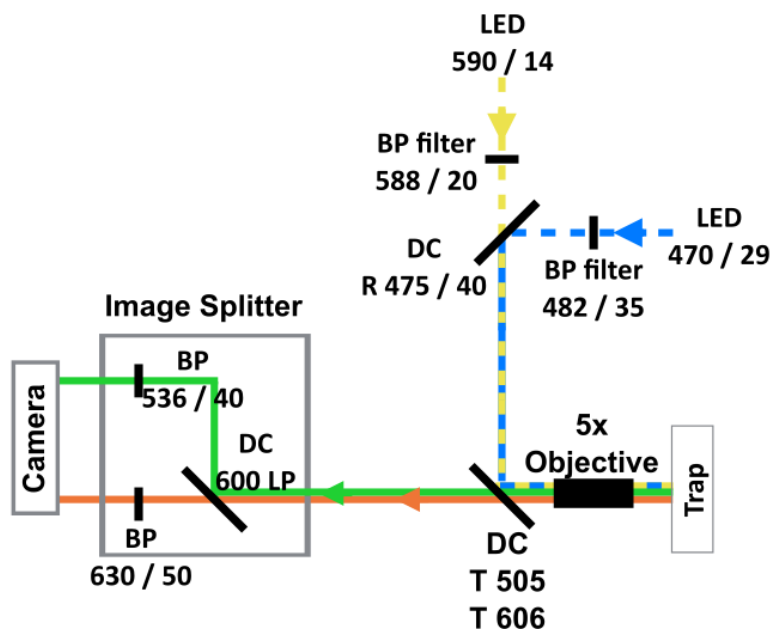41
42
43

44
45 **1. Microscope scheme**

46
47 **Supplementary Figure 1. Schematic of the custom-built microscope.** *The microscope was equipped with a blue LED*
48 *(470/29 nm), an amber LED (590/14 nm), excitation filters (482/35 nm, 588/20 nm), a dual bandpass dichroic mirror*
49 *(transmission edges at 505 nm and 606 nm), a 5X objective and an image splitter containing a longpass filter (600*
50 *nm) and emission filters (536/40 nm, 630/50 nm). This filterset allowed for the imaging of FITC (Fluorescein*
51 *Isothiocyanate) and ROX (Carboxy-X-Rhodamine). A Stingray-F145B ASG camera (ALLIED Vision Technologies Gmbh)*
52 *was used to acquire images. The numbers next to the filters and the LEDs correspond to the light wavelength in*
53 *nanometers / FWHM.*
54
55 The crosstalk from the FITC channel to the ROX channel was calculated with the following standard
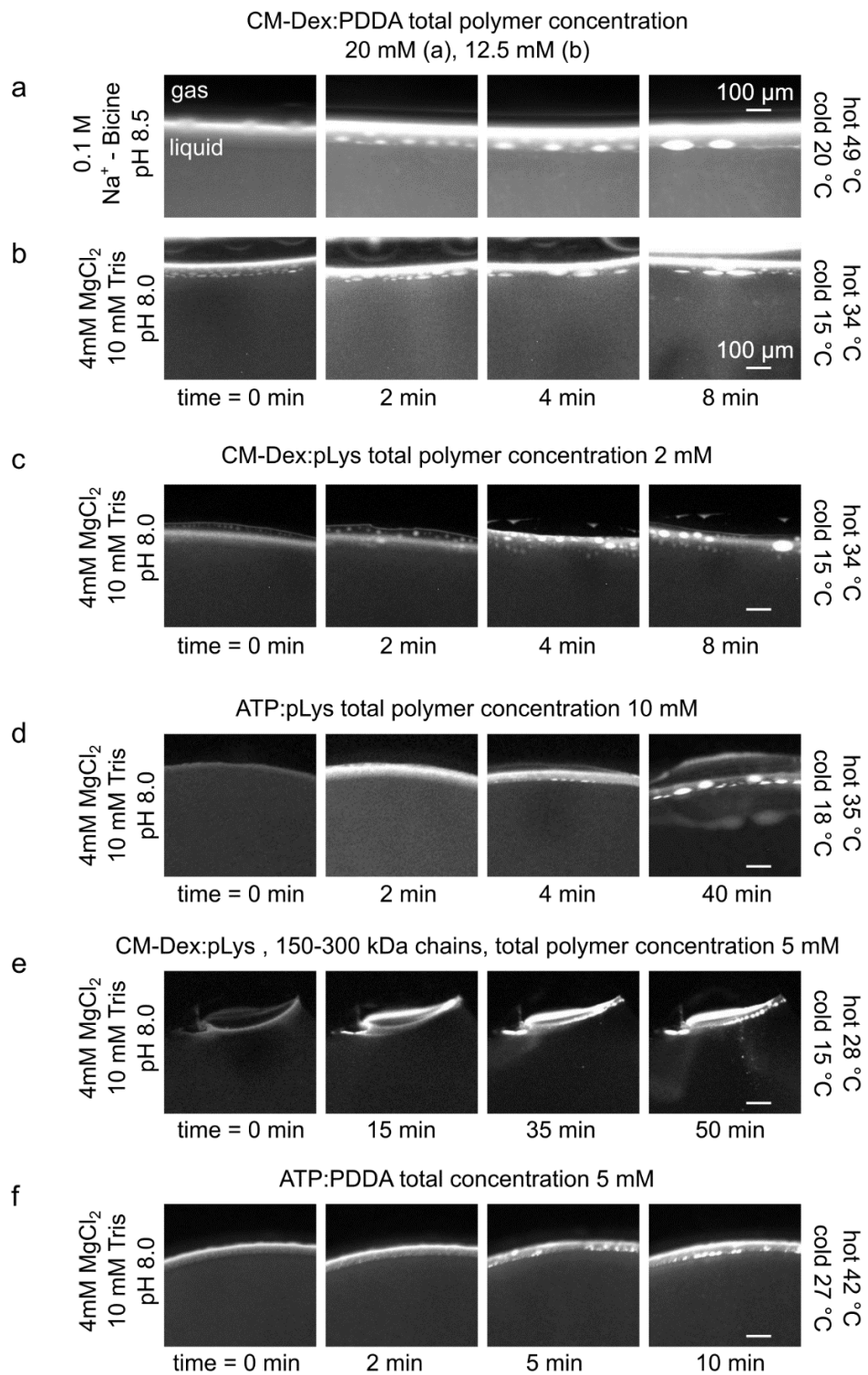56 protocol[1]:

57 $$crosstalk = \frac{DA_A}{AA_A}$$

58 where the first capital letter indicates the excitation wavelength (D), the second capital letter indicates
59 the emission wavelength (A), and the subscript index indicates which dye was used (D = FITC, A = ROX).
60 The crosstalk from the FITC to the ROX channel was measured to be approximately 7%. This is a relatively
61 low value which would not have affected the qualitative comparison made in Figure 5.
62
63
64
65 **2. Effect of buffer and polymer composition on coacervate assembly at the gas-water interface**

66 We studied the effect of the buffer composition and the type of coacervate polymer on the assembly and
67 growth of the coacervate droplets at the gas-water interface. Following the same procedure of the
68 experiments shown in Figure 3, we ran several experiments with slightly different conditions of buffer or
69 polymer composition, and temperature gradients. The mixtures were doped with 0.1 % FITC-labeled CM-
70 Dex or ATP. The results are schematized in Supplementary Figure 2. The droplet size over time was
71 quantified and shown in Figure 3e.

2

CM-Dex:PDDA total polymer concentration
20 mM (a), 12.5 mM (b)

a 0.1 M Na⁺ - Bicine pH 8.5 | gas | liquid | 100 μm | hot 49 °C cold 20 °C

b 4mM MgCl₂ 10 mM Tris pH 8.0 | 100 μm | hot 34 °C cold 15 °C

time = 0 min | 2 min | 4 min | 8 min

CM-Dex:pLys total polymer concentration 2 mM

c 4mM MgCl₂ 10 mM Tris pH 8.0 | hot 34 °C cold 15 °C

time = 0 min | 2 min | 4 min | 8 min

ATP:pLys total polymer concentration 10 mM

d 4mM MgCl₂ 10 mM Tris pH 8.0 | hot 35 °C cold 18 °C

time = 0 min | 2 min | 4 min | 40 min

CM-Dex:pLys , 150-300 kDa chains, total polymer concentration 5 mM

e 4mM MgCl₂ 10 mM Tris pH 8.0 | hot 28 °C cold 15 °C

time = 0 min | 15 min | 35 min | 50 min

ATP:PDDA total concentration 5 mM

f 4mM MgCl₂ 10 mM Tris pH 8.0 | hot 42 °C cold 27 °C

time = 0 min | 2 min | 5 min | 10 min

75 ***Supplementary Figure 2. Effect of the buffer and polymer composition on coacervate growth at the gas-water***
76 ***interface.*** *Growth mechanism by fusion for different coacervate types (indicated above the image), for different*
77 *buffers (indicated at the left) and different temperature gradients (indicated at the right). The scale bar indicates 100*
78 *μm.*

79   When using a different buffer (Na$^+$-bicine or Tris-MgCl$_2$) or a different polymer (CM-Dex, pLys,
80 PDDA or ATP), we observed only minor differences in the coacervate assembly process. The growth
81 process (by fusion with other coacervate droplets), occurred with similar timescales and reached a similar
82 threshold size in all the cases that we explored.

83

84 **3. Relationship between droplet growth and total polymer concentration**

85 We studied the effects of the total polymer concentration on the growth of the coacervate. To this end,
86 we performed a series of experiments in a thermal gradient (warm side 49 °C and cold side 20 °C), buffer
87 (4 mM MgCl$_2$, 10 mM Tris, pH 8.0) and the CM-Dex: PDDA (molar ratio 6:1, [carboxyl]/[amine] = 5), varying
88 the total polymer concentration between 1 and 20 mM, doped with 0.1 % FITC-labeled CM-Dex. After
89 inserting the coacervate solution in the thermal trap, we took a microscopy image every ~ 1 second. The
90 images were analyzed with ImageJ or LabVIEW to determine the growth rate and the average droplet size
91 at the interface. The results are shown in figure S3.1. Every data point in the plot corresponds to an
92 independent experiment.
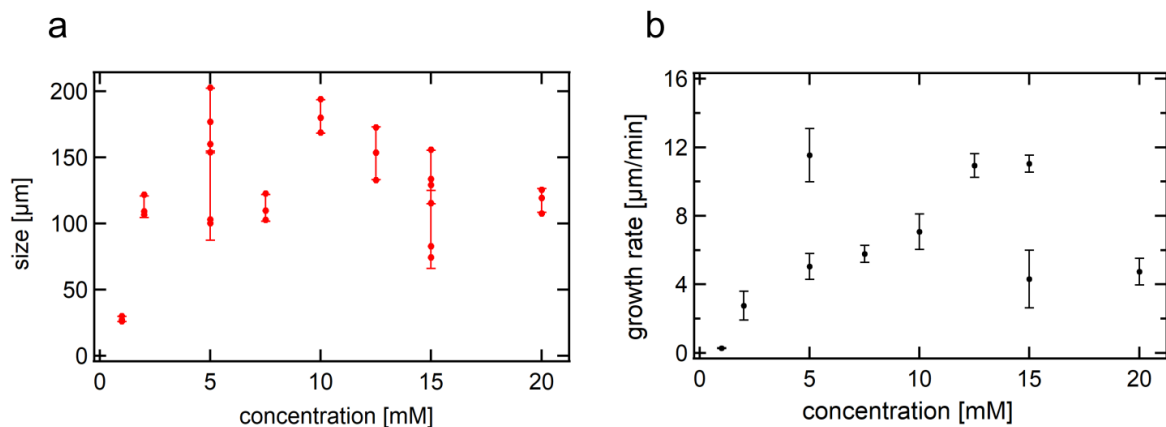
93
94 ***Supplementary Figure 3.1. No clear relationship between coacervate growth and total polymer concentration.*** *(a)*
95 *Average size at steady state (after ~ 1h of thermal gradient). Every set of data is represented by 3 points (the 3 largest*
96 *coacervate droplets observed in the experiment) and the error bar (standard deviation). b) Growth rate of the*
97 *coacervate droplets as a function of polymer concentration. Error bars correspond to the standard deviation of the*
98 *growth rate extracted from the linear fit of the size vs time traces (here not shown).*

99   Due to the intrinsic noise of our experiments, we could not determine any significant effect of the
100 total polymer concentration on the final droplet size at steady state and their growth rate.
101   Below the critical coacervate concentration (CCC), polymers are not able to coacervate and form
102 droplets. We tested whether the accumulation properties of the heated gas-water interfaces in our pores
103 were able to concentrate the polymers to cross the CCC threshold and trigger coacervation. We used a
104 CMDex:PDDA mixture (molar ratio 6:1, [carboxyl]/[amine] = 5), with a total polymer concentration below
105 the CCC, doped with 0.1 % FITC-labeled CM-Dex. In previous experiments the CCC of CM-Dex:PDDA >1mM.
106 Therefore, in the experiments that follow, we used a total polymer concentration of 0.2 mM and 0.05
107 mM, in a buffer containing 4 mM MgCl$_2$ and 10 mM Tris at pH 8 with a temperature gradient (hot side

108 49 °C, cold side 20 °C) (below the CCC). The polymer accumulation at the interface was imaged with
109 fluorescence microscopy (Supplementary Figure 3.2).
110   Our results show that no coacervate droplets were observed in the system but there was visible
111 polymer accumulation at the gas-water interface. This observation suggests that thermal trap acts at the
112 mechanical level to favor the assembly and fusion of the existing coacervate droplets.
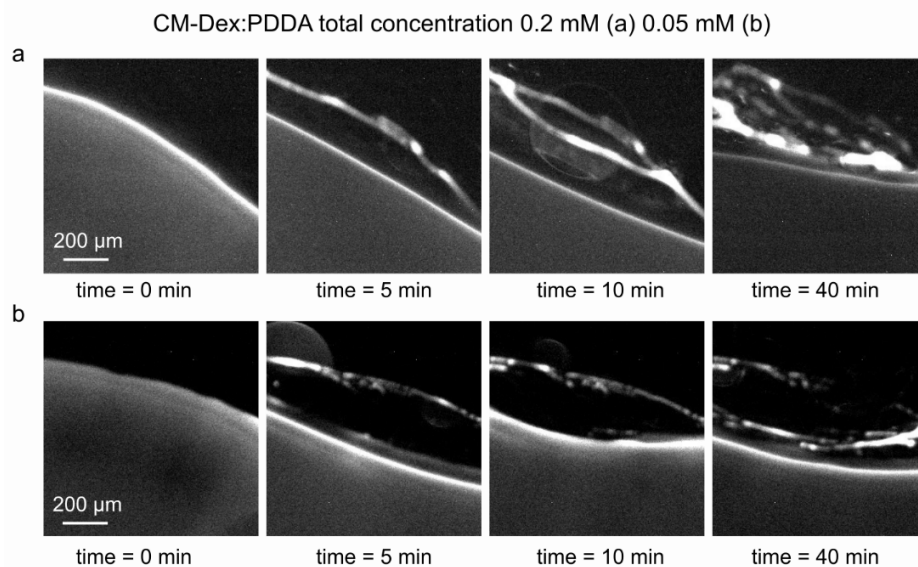
113
114
115 *Supplementary Figure 3.2. No coacervation below the critical coacervate concentration. Optical microscopy images*
116 *of the gas-water interface in the thermal trap at different times (0, 5, 10 and 40 minutes) of the coacervate mixture*
117 *in the thermal pore, for 0.2 mM (a) or 0.05 mM (b) total polymer concentration. No coacervate droplets were*
118 *observed at the gas-water interface or in the bulk despite the visible polymer accumulation.*

119

120 **4. Control experiment without gas-water interface**

121 In order to see the effect of the thermal gradient on coacervation, we characterized the effect of a thermal
122 flow on coacervate droplets in a control experiment without gas bubbles (Figure S4).
123
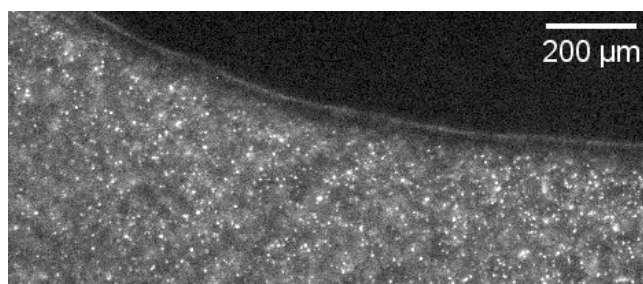
124
125
126 *Supplementary Figure 4. No large coacervate droplets in a thermal gradient without a gas bubble. Coacervate*
127 *droplets were prepared from CM-Dex:pLys (molar ratio 4:1, [carboxyl]/[amine] = 7, total polymer concentration 2*
128 *mM), buffer 10 mM Tris, 4mM MgCl$_2$, pH 8.0, temperature gradient of 29 °C. The image shows the fluorescence of*
129 *pLys (0.1 % labeled with FITC). Small coacervate droplets (size < 10 μm) are seen moving with the convection flow.*
130 *No larger coacervates (size > 15 μm) were observed forming in the system.*

5

131   In the absence of the gas bubble, no large coacervates form in the chamber. Small coacervate
132   droplets (< 15 μm), which spontaneously formed during the initial mixing of the polymers, could be seen
133   in the bulk transported by the convection flow at a speed of about 1.6 ± 0.4 μm/s. However, they did not
134   fuse to form larger droplets. The gas-water interface has the role of accumulating small microdroplets and
135   promote their fusion. In the experiments with a gas-water interface, we observed that the coacervate
136   droplets could grow up to an average size of 150 μm. Sometimes we could observe coacervate droplets
137   as large as 300 μm.
138
139
140
141   **5. Sedimentation of coacervate polymers**

142   We characterized the behaviour of the coacervate droplets under equilibrium condition. In the absence
143   of a thermal gradient, no convection occurs in the liquid phase, and the coacervate droplets fall to the
144   bottom of the channel, driven by gravity, to form a single coacervate macrophase. We studied the
145   sedimentation dynamics of CM-Dex:pLys (molar ratio 4:1, [carboxyl]/[amine]=7, total polymer
146   concentration 8 mM in 4 mM $MgCl_2$, 10 mM Tris at pH 8.0, doped with 0.1 % FITC-labeled CM-Dex) in a
147   microfluidic chamber at room temperature (22 °C, no temperature gradient). The droplet size was
148   determined as its horizontal width. The results are shown in Figure S5.1. The growth rate of the coacervate
149   droplets by sedimentation is much slower (requires hours) than the growth rate at the heated gas-water
150   interface shown in figure 3e (requires minutes). On the other hand, the final droplet size is much greater,
151   and only constrained by the size of the microfluidic chamber.
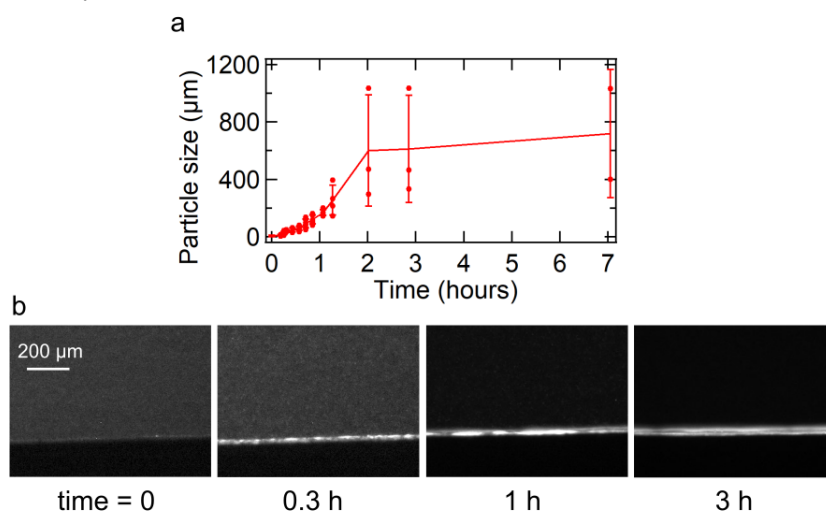
152
153   ***Supplementary Figure 5.1. Sedimentation of coacervate droplets induced by gravity.*** *a) Quantification of droplet*
154   *size over time. The droplets slowly sediment at the bottom of the chamber and fuse to become larger over the course*
155   *of several hours. Error bars indicate standard deviation (n~3). b) Snapshots of the sedimentation at different times.*
156   *The fluorescent layer at the bottom is the site of sedimentation.*

157   In the presence of the thermal gradient, a circular convective flow in the bulk arises. As we have
158   already seen in our experiments, it transports the small coacervate droplets around in the bulk, preventing
159   the sedimentation.
160   We simulated the sedimentation process by a 2D finite element simulation, using the software
161   Comsol Multiphysics. We modeled the heat transfer, laminar flow, diffusion and transport of coacervate
162   droplets in a thermal gradient, in a chamber equivalent to the one we used in our experiments (5 mm x
163   500 μm). The density of the coacervate droplets was set between 1.01 and 1.10 g/cm^3 and their radius

6

164   was set to 5 µm as determined from our experiments. The total polymer concentration was set to 1 mM.
165   The diffusion coefficient was calculated from the radius and the density, using the following Stokes-
166   Einstein equation:

167
$$D = \frac{k_B \, T}{6 \, \pi \, r_0 \, \mu_B(T)}$$

168   where k_B is the Boltzmann constant 1.38e-23 J/K, T is the temperature, r_0 is the droplet radius ad μ_B is the
169   bulk viscosity. The thermal gradient was varied between 0 °C and 85 °C. Results are shown in
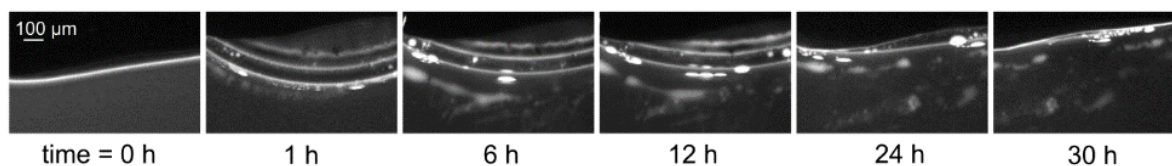170   Supplementary Figure 5.2.

171
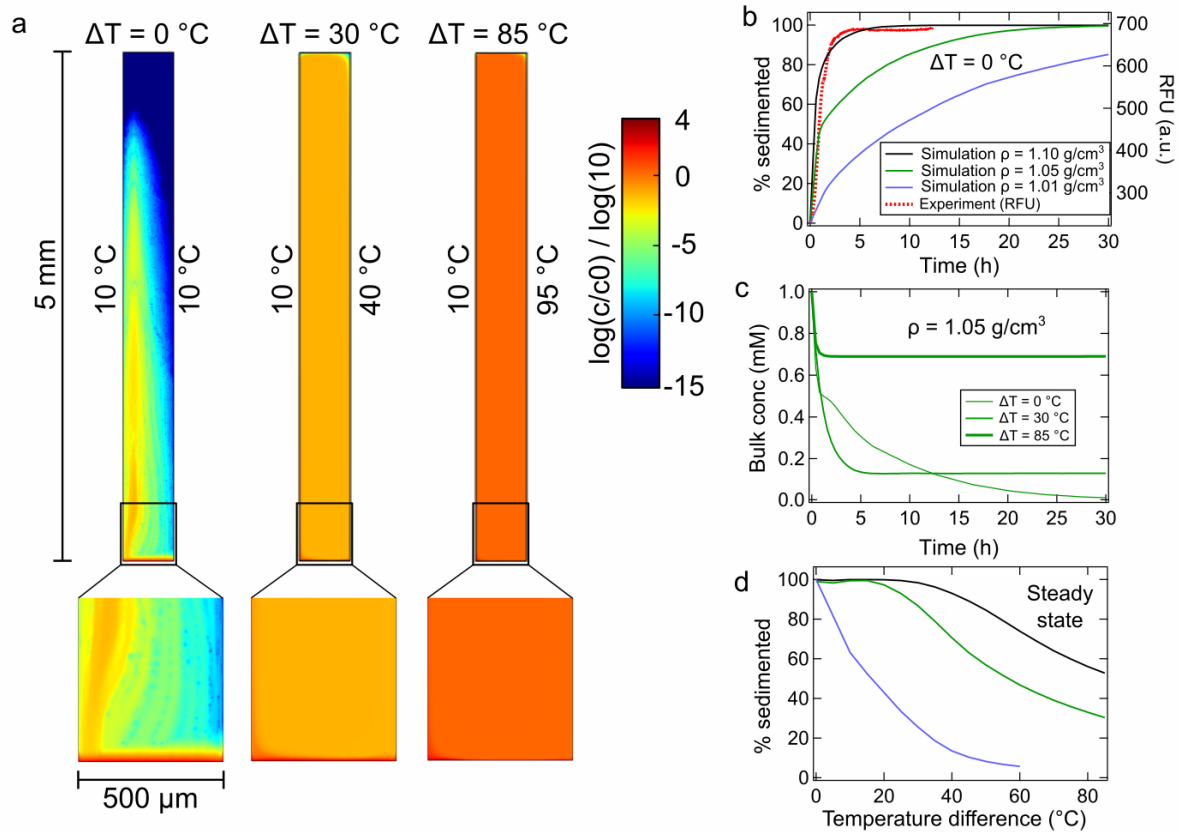
Supplementary Figure 5.2. Finite element simulation of the sedimentation of coacervate droplets in our thermal
trap. a) Distribution of coacervate concentration in a trap section after 10 h, for ΔT of 0, 30 and 85 K. The coacervate
density coefficient used here was 1.1 g/cm³. b) Sedimentation % over time at isothermal temperature for 3 different
densities. Red dotted line corresponds to experimental data (the experiment illustrated in Supplementary Figure 5.1).
c) Bulk coacervate concentration over time calculated for different temperature gradients. d) Sedimentation % at
steady state (simulation time = 30 h) as a function of the temperature gradient ΔT and for different densities.

178   In the absence of the thermal gradient, almost 100% of the coacervate droplets sediment to the
179   bottom of the chamber within 10 hours, driven by gravity (Supplementary Figure 5.2a, left). The timescale
180   of sedimentation depends on the density coefficient of the droplets. The best agreement between
181   experiments and simulation occurs for a density coefficient between 1.10 and 1.05 g/cm³ (Supplementary
182   Figure 5.2b). Note that the comparison between experiment and simulations is purely qualitative
183   (expressed in arbitrary RFU), due to the difficulty in accurately calculating the total fraction of sedimented
184   coacervates by fluorescence microscopy.

7

185   The total sedimented fraction depends on the convection triggered by the thermal gradient
186 (Supplementary Figure 5.2a middle, right pictures, and S5.2c-d). Our results show that a fraction of
187 droplets will sediment even in the presence of the thermal gradient. However, our simulations show that
188 temperature gradients between 19 and 40 °C will prevent the sedimentation of the coacervate fraction
189 by 3 - 30 %. Furthermore, simulations, up to 96 hrs show that the droplets remain in the bulk solution
190 indicating that with the thermal flow the droplets are prevented from sedimenting (data not shown). Note
191 that the data shown in Supplementary Figure 5.2d represent the final sedimented fraction at steady state.
192   Experiments undertaken within the thermal trap with dispersions of coacervate droplets
193 (ATP:PDDA droplets, 5 mM total concentration) that were subjected to shallow temperature gradients
194 (hot side 42 °C, cold side 27 °C) showed droplets at the gas-water interface after 30 hrs (Supplementary
195 Figure 5.3). Taking this into account, it is likely, that our experiment will reduce sedimentation further as
196 the gas-water interface introduce additional flows to the system (e.g. capillary flows) that accumulate and
197 maintain coacervate droplets at the gas-water interface. In summary, the thermal gradient is able to
198 reduce the sedimentation of coacervates, maintaining a fraction of droplets to circulate in the bulk.
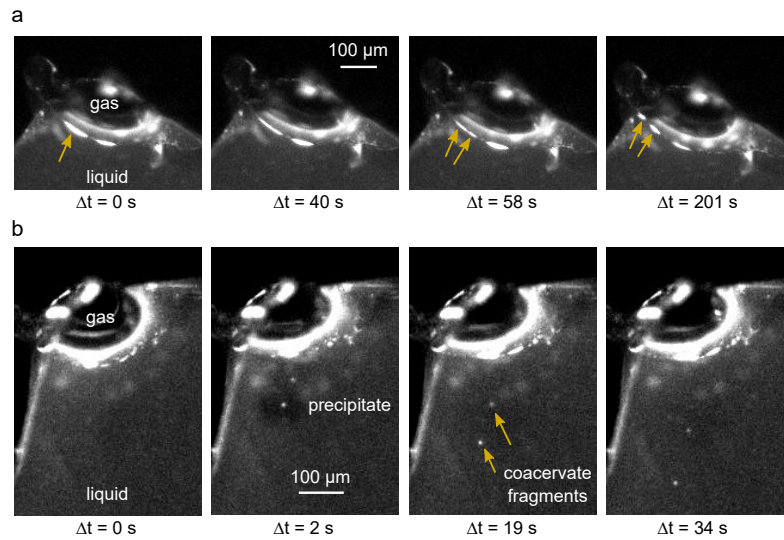199

200   time = 0 h   1 h   6 h   12 h   24 h   30 h
201 *Supplementary Figure 5.3. Coacervate droplets are retained at the gas-water interface and do not sediment.*
202 *ATP:PDDA coacervate droplets formed at the gas-water interface do not undergo sedimentation for at least 30 hours.*
203

6. Division and fragmentation of CM-Dex:pLys coacervate droplets

205 We have already shown in Figure 4 that CM-Dex:PDDA droplets in a thermal gradient can divide and be
206 fragmented by the forces acting at the gas-water interface (capillary flows and perturbative fluxes). In
207 additional experiments, we observed the same division and fragmentation processes happening for
208 solutions containing a different coacervate composition: CM-Dex:pLys (molar ratio 4:1,
209 [carboxyl]/[amine]=7, total polymer concentration 5 mM, doped with 0.1 % FITC-labeled CM-Dex). The
210 results are shown in the Supplementary Figure 6.
211   The coacervate droplet at the gas-water interface (yellow arrow) was stretched by the capillary
212 forces, until the coacervate droplet started to divide, and the two daughter droplets separated. The event
213 occurred in a time window of approximately 200 seconds.
214   Supplementary Figure 6b shows the fragmentation of coacervates. The precipitation of water re-
215 increased the water level and moved the gas-liquid interface slightly upwards. Therefore, the accumulated
216 coacervates that were stuck in a quasi-dry state on the hot sapphire were re-dissolved into the liquid. The
217 perturbative fluxes induced by the water precipitation induced the fragmentation of the polymers,
218 creating smaller droplets that fell into the bulk and started circulating with the convection flow.

8

a

gas

liquid

100 µm

gas

Δt = 0 s   Δt = 40 s   Δt = 58 s   Δt = 201 s

b

gas

gas

precipitate

100 µm

liquid

coacervate fragments

Δt = 0 s   Δt = 2 s   Δt = 19 s   Δt = 34 s

Supplementary Figure 6. Division of CM-Dex:pLys coacervate droplets at the gas-water interface. *a) Fission of a CM-Dex:pLys droplet into two smaller droplets induced by forces at the gas-liquid interface. b) Water precipitation rehydrates the stuck coacervates and induces fission by fragmentation. The temperature gradient for both experiments was: warm side 26 °C, cold side 15 °C.*

The division mechanisms described here and in Figure 4 are purely physical phenomena. The chemical composition of the coacervate droplets seems to play a minor role, as we observed similar events for coacervate droplets made of CM-Dex:PDDA or CM-Dex:pLys. We therefore consider these division mechanisms to have played an important role in the primordial division of protocells, since they derive from the physical properties of the environment only and do not require any specific chemical component or active biological machinery. The simple and ubiquitous setting of a gas bubble within a thermal gradient contains all the physical properties to trigger these type of division mechanisms.

7. Figure 4a extended: division by droplet stretching

The dynamics of the dividing coacervate droplet (Figure 4a) was tracked throughout the timeframe of the experiment to confirm that the division event was not an artefact arising from the 2D imaging technique, as this type of imaging does not provide information in the x-axis of our thermal pore. In particular, we wanted to test whether two coacervate droplets could have hidden behind one other and then moved parallel in the x-axis, creating a visual artifact similar to a division event.

9
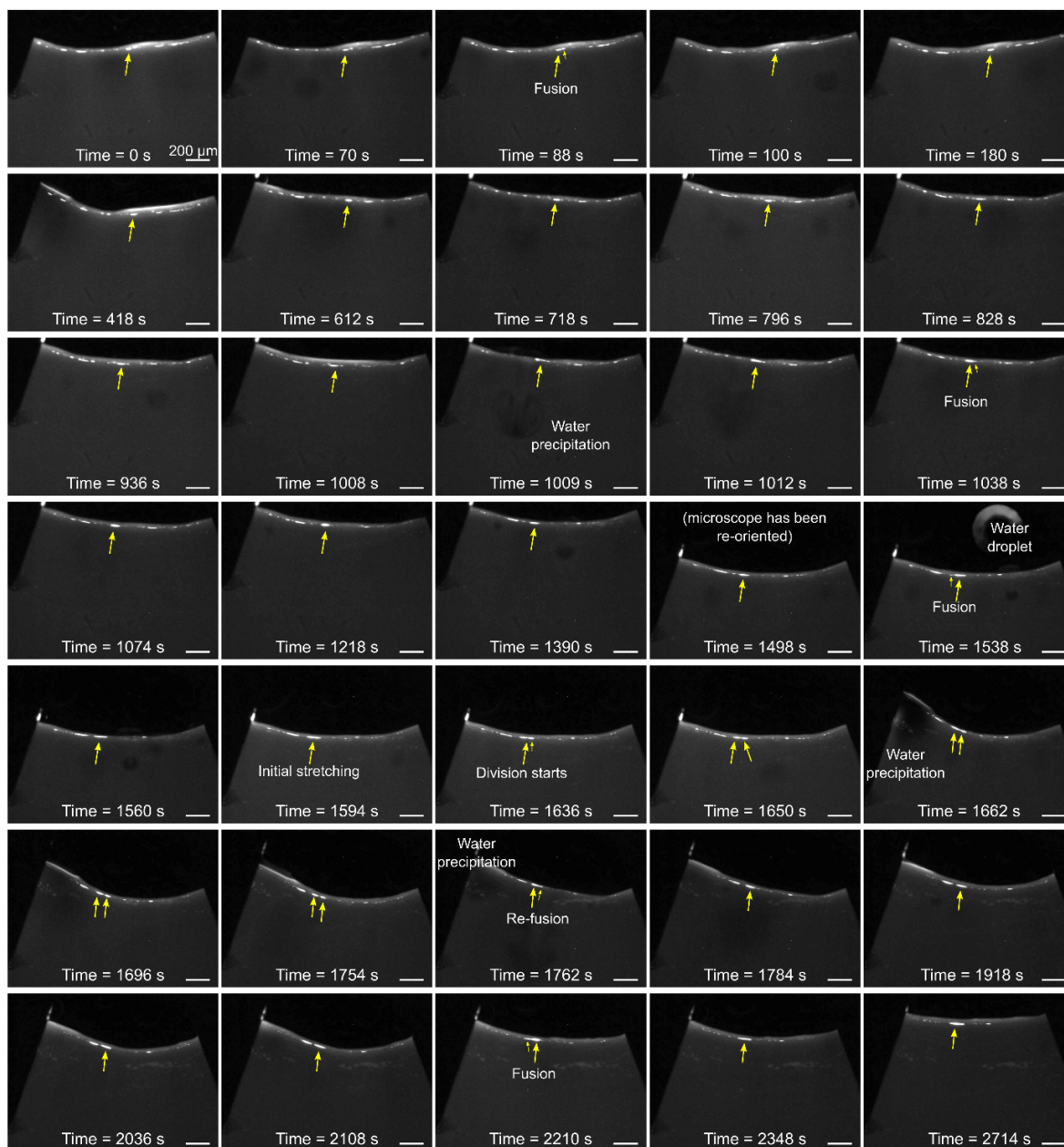
Supplementary Figure 7. Coacervate division by stretching. *Images at different times of the coacervate droplet that underwent division in Figure 4a. Experimental conditions were: CM-Dex:PDDA (molar ratio 6:1, [carboxyl]/[amine] = 5), total concentration 2 mM in 4 mM MgCl$_2$, 10 mM Tris, pH 8.0, doped with 0.1 % FITC-labeled CM-Dex. The temperature gradient was 19 °C with the warm side 34 °C, cold side 15 °C. The time reported in the pictures is not the absolute time of the start of the experiment, but is relative to the arbitrary starting point indicated in the first picture.*

Careful analysis of the full time frame (frame rate 0.75 fps) of coacervate division events at the air-water interface (Supplementary Figure 7) showed repeated fusion and water precipitation events for many minutes, until the droplet started to undergo division (time ~ 1500s). We do not observe any indication of a second droplet moving behind the droplet of interest (indicated with a yellow arrow). It can be also seen that the droplet of interest remains distinct for several minutes before undergoing a

249 division event. As the constrained thickness of the pore (x-axis size) is 250 μm and the daughter droplets
250 measure approximately 90 μm, it is highly unlikely that two droplets of similar size will coexist behind
251 each other without coalescence. Especially, when considering that capillary flow at the gas-water
252 interface pushes towards the warm side that facilitates fusion events and that we typically observe fusion
253 events between droplets in close proximity to each other within 10 seconds (Figure 3d). Our results
254 indicate that there is no artefact of droplet fusion that arises from the imaging method used in our
255 experiments.
256
257 **8. Measurement of the binding constant of pLys:CM-Dex and pLys:RNA**

258 In Figure 5, we observed that RNA:pLys droplets are preferentially formed when a mixture of RNA, pLys
259 and CM-Dex is provided. To gain a better understanding in the mechanism responsible of that
260 phenomenon, we measured the binding constant K_D of the RNA:pLys and of the CM-Dex:pLys complexes.
261 Measurements have been done using a Nanotemper NT.115 Pico machine, which measures a binding
262 dependent fluorescence signal upon local heating with IR laser.
263 Serial dilutions of CM-Dex (15 kDa) or RNA (single stranded, 51 nt) were mixed together with a
264 constant amount of FITC-labeled pLys (15-30 kDa). While the final FITC-pLys concentration was
265 maintained constant at 20 nM, CM-Dex and RNA concentrations spanned many orders of magnitude
266 ranging from 0.1 nm to 1 μM. The solutions of CM-Dex: pLys or RNA: pLys were inserted into thin glass
267 capillaries and placed on an alluminium holder and then inside of the Nanotemper NT.115 Pico machine.
268 Therefore, the fluorescence of the sample was measured over time. A focused IR laser beam was used to
269 locally heat the solution inside the capillaries, and the intensity response was measured. To calculate the
270 K_D, the obtained data have been fitted with the following model:
271

272 $$f(Conc)$$
273 $$= U + \frac{(B - U) \cdot (Conc + TargetConc + K_D - \sqrt{(Conc + TargetConc + K_D)^2 - 4 \cdot Conc \cdot TargetConc})}{2 \cdot TargetConc}$$
274
275 (1)
276
277 where U and B indicate the fluorescence response values of the unbound (after IR heating) and bound (no
278 IR heating) states, respectively. TargetConc corresponds to the concentration of the labeled species (pLys),
279 and K_D corresponds to the binding constant. Conc indicates the concentration of CM-Dex (Figure S8.1a) or
280 RNA (Figure S8.1b).
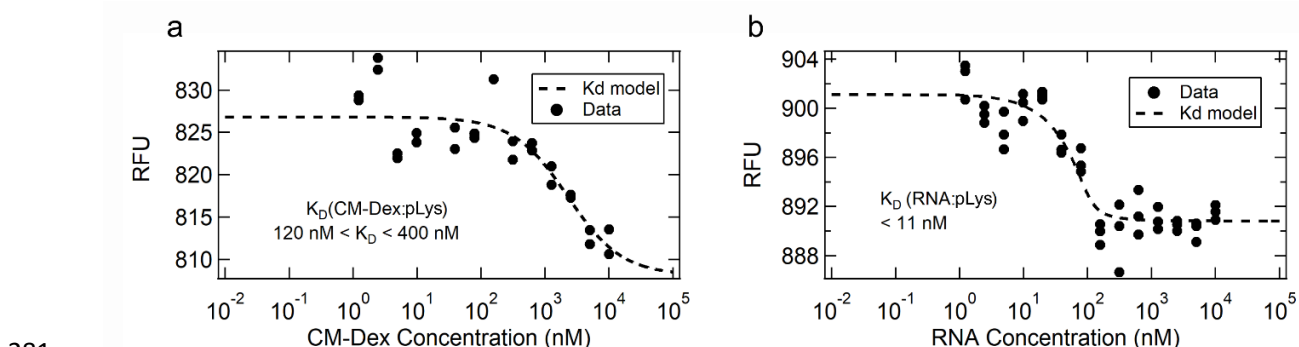
281

282 ***Supplementary Figure 8.1. Measurement of the binding constant K_D.*** *Dose-response curves for the CM-Dex: pLys*
283 *complex (a) or for the RNA: pLys complex (b). The dots indicate experimental data, and the dashed line corresponds*

11

284 *to the fit (equation 1).*

285   Instead of estimating a single value for the binding constant, we preferred to estimate a range
286 where it most likely lies within. We achieved that by estimating the NRMSD (Normalized Root Mean
287 Squared Deviation) between the data and the model. We arbitrarily chose a NRMSD threshold of 15% to
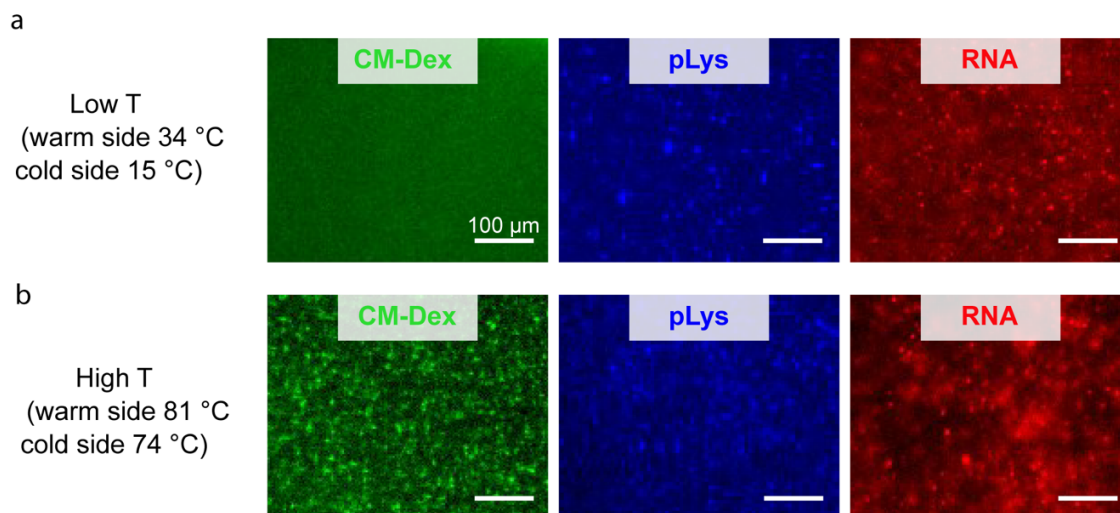288 estimate the range. NRMSD was defined as:

289 $$NRMSD = \frac{RMSD}{RFU_{max} - RFU_{min}}$$

290 where *RMSD* corresponds to the root mean squared deviation of the data. RFU_{max} and RFU_{min} are the
291 maximum and minimum values of the RFU data. The binding constant (K_D) of the CM-Dex:pLys complex
292 resulted to be higher than the K_D of the RNA:pLys complex (120 nM < K_D < 400 nM against K_D < 11 nM),
293 suggesting stronger binding of the RNA:pLys complex. This result can possibly explain what we observed
294 in Figure 5. In a solution containing all the three components (CM-Dex, RNA and pLys), pLys preferentially
295 creates complexes with RNA, since their binding is stronger.

296   To further investigate whether the separation of coacervate populations in the thermal trap is
297 driven by overcoming the binding constants at the gas-water interface, we performed additional control
298 experiments. We studied a mixture of CM-Dex, pLys and RNA (total polymer concentration 2 mM) in the
299 absence of a gas bubble, at temperature gradients (34 - 15 °C, as described previously) and at higher
300 temperatures gradients (81 - 74 °C). The higher temperature is expected to overcome the binding
301 constants, leading to the formation of bulk coacervate droplets enriched in all 3 components: the same
302 effect induced by the gas-water interface (Figure 5).

303   At low temperatures (Supplementary Figure 8.2a), the bulk coacervate droplets seemed to be
304 mostly made of pLys and RNA with a low, almost indistinguishable fluorescence signal from CM-Dex within
305 the coacervate droplets (Supplementary Figure 8.2 left). In comparison, experiments undertaken at higher
306 temperatures (Supplementary Figure 8.2b) show evidence of three components (CM-Dex, pLys and RNA)
307 by three fluorescent channels, suggesting that the bulk droplets were enriched in all three components.
308 Our results indicate that, the higher temperatures could override the binding constant and trigger the
309 interaction between all the three polymer components. Therefore, these results support our hypothesis
310 that the gas-water interface helps to overcome the binding constants at lower temperatures.
311
312

12

a

Low T
(warm side 34 °C
cold side 15 °C)

CM-Dex pLys RNA

100 µm

b

High T
(warm side 81 °C
cold side 74 °C)

CM-Dex pLys RNA

313
314 ***Supplementary Figure 8.2. Bulk droplets enriched in all three components form at higher temperatures.*** *a) At low*
315 *temperatures (34 °C - 15 °C gradient), the bulk droplets are preferentially enriched in pLys and RNA, while poor in*
316 *CM-Dex. b) At higher temperatures (81 °C - 74 °C gradient) the binding constants are overridden by the increased*
317 *kinetic energy and the bulk coacervate droplets are enriched of all three components. Every picture corresponds to a*
318 *different experiment. The solutions contained: 10 mM MgCl$_2$, 10 mM Tris, pH 8. CM-Dex:pLys [carboxyl]/[amine] = 7,*
319 *molar ratio 4:1. Total polymer concentration was 2 mM, RNA concentration 1 µM. Note that every picture*
320 *corresponds to a separate experiment.*

321

322 **9. Component ratio of the coacervates in the thermal pore**

323   To characterize the effect of the water-air interface on properties of the coacervate droplets we
324 measured the zeta potential (ζ) of coalescing coacervate droplets (CM-Dex:pLys) in bulk solution over time
325 and compared this to any observed changes in the charge ratio determined by image analysis of the
326 droplets within the thermal trap. The ζ potential corresponds to the difference between the potential on
327 the shear surface of the droplet and the potential of the solution and is an indirect measure of the charge
328 ratio at the surface of the droplet. To do this, dispersions of CM-Dex:pLys coacervate droplets at 2 mM in
329 10 mM Tris and 4 mM MgCl$_2$ at pH 8 (CM-Dex:pLys molar ratio 4:1, [carboxyl]/[amine] = 7) were prepared
330 and immediately loaded into folded capillary cells (DTS1070) so that the water level was above the gold
331 electrodes with no air bubbles observable to the eye. The cell was loaded into a Zetasizer Nano ZS (Pzen
332 5600) that was preheated at 30 °C. The sample was incubated for 10 minutes and 5 runs of 10 seconds
333 were taken using the 173° backscatter mode to obtain dynamic light scattering data. This measurement
334 was repeated 3 times. The sample was then subjected to zeta potential measurements which consisted
335 of 10 secs equilibration time followed by 3 measurements of 10 runs with 300 secs between each
336 measurement. This cycle was repeated over at least 2.5 hrs. The Zeta sizer was controlled using the
337 manufacturers zetasizer software which undertook the analysis of the data using the general purpose
338 analysis mode (light scattering) and the Smoluchowski model (Zeta measurements) using 1.378 and 1.334
339 for the refractive index for the coacervate and supernatant respectively.
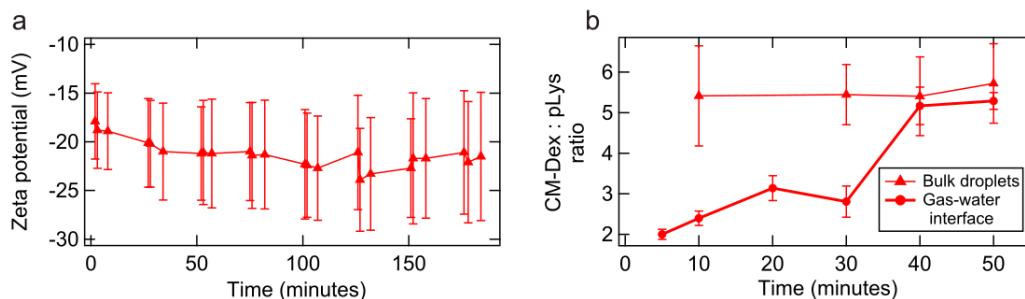
13

We did not find a significant change in the surface charge over time (Figure S9.1a). Even though this measurement was performed in the bulk solution and under isothermal conditions, we observed analogous behavior within the bulk region in the trap experiment (Figure S9.1b). This was determined by fluorescence microscopy, by performing different experiments with FITC-labeled CM-Dex or pLys. We characterized the ratio of the polymers of the coacervate droplets assembled at the gas-water interface and in the bulk of our thermal pores. Conversely, at the gas-water interface, a change in the polymeric ratio could be observed during time. This could be attributed to differential accumulation of the individual polymers at the gas-water interface, driven by different diffusion coefficients, that variably enriched the droplets.

Furthermore, we undertook image analysis of dispersion of CM-Dex:pLys:RNA (51 nt) (1.6 mM, 0.4 mM, 1 μM, respectively), in a buffer containing 10 mM Tris, 4 mM MgCl$_2$, pH 8 within the thermophoretic pore. The temperature gradient was: hot side 34 °C, cold side 15 °C. The data shown in Supplementary Figure 9.2 have been obtained by analyzing the dual-channel fluorescence movies over time where two of the three polymers were labeled. [Note that the ratios in Figure S9.2 are given as molar ratios between the polymers, not as ratios between chemical groups (e.g. [carboxy]/[amine]).

The analysis shows that the ratio of the components in the droplets changes over time. Both the ratios CM-Dex:RNA (Supplementary Figure 9.2a) and pLys:RNA (Supplementary Figure 9.2b) decreased over time, while the CM-Dex:pLys ratio (Supplementary Figure 9.2c) remained almost constant. This can be explained by the fact that the droplets, both at the interface and in the bulk (Supplementary Figure 9.3)., become enriched in RNA over time. The coacervate droplets in the bulk were particularly poor in CM-Dex in comparison to the coacervates assembled at the gas-water interface (Supplementary Figure 9.2d).

14

369
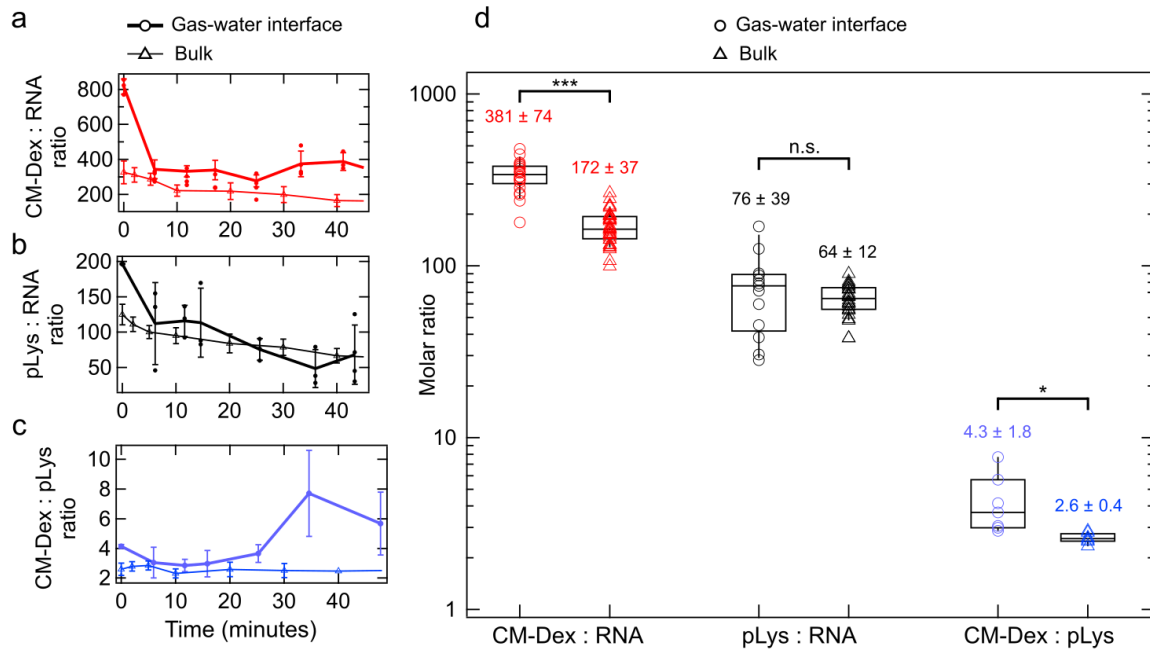
Supplementary Figure 9.2. Component ratio of a CM-Dex:pLys:RNA mixture in the thermal pore. *The droplets become enriched in RNA over time. CM-Dex:RNA (a), pLys:RNA (b) and CM-Dex:pLys molar ratios over time calculated on the coacervate droplets at the gas-water interface (thick lines with circles) or in the bulk (thin lines with triangles). d) Box plots of the ratios from a-c at steady state. The statistical difference between gas-water interface (circles) and bulk (triangles) was tested with a t-test.*
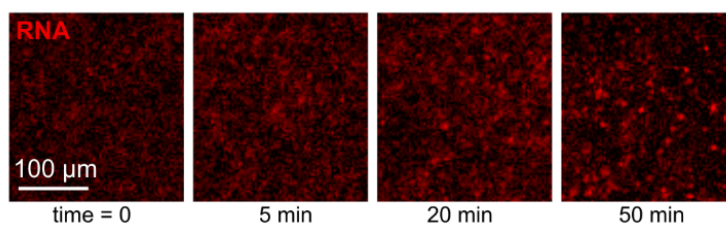
380 **Supplementary Figure 9.3. RNA enrichment in the bulk coacervate droplets over time.** *Fluorescence images (RNA*
381 *fluorescence) of the bulk coacervate droplets at different times. An increase in the fluorescence levels is clearly visible.*
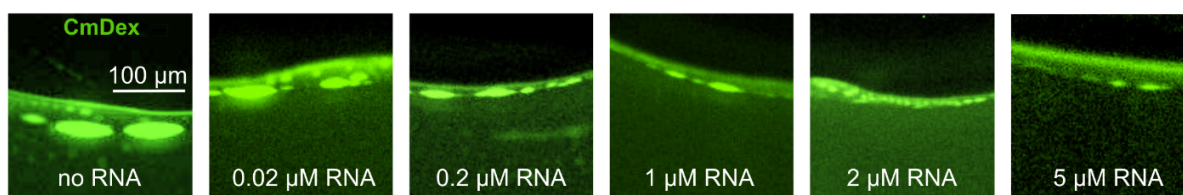
382

383

384

385

15

10. Figure 5 extended: RNA concentration vs final coacervate size

Supplementary Figure 10. RNA reduces the size of CM-Dex:pLys droplets in a concentration-dependent manner.
From left to right: no RNA, 0.02 mM RNA, 0.2 µM RNA, 1 µM RNA, 2 µM RNA, 5 µM RNA were added in a solution of CM-Dex:pLys (molar ration 4:1, [carboxyl]/[amine] = 7) at a concentration of 2 mM containing 0.1% of FITC-labeled CM-Dex in a buffer made of 4 mM MgCl$_2$, 10 mM Tris at pH 8. The images show the resulting coacervates at the gas-water interface after ~1h of temperature gradient (warm side 34 °C, cold side 15 °C).

11. List of attached files

supplementary_movie_1_coacervate_fusion.avi
supplementary_movie_2_coacervate_division.avi
supplementary_movie_3_coacervate_fragmentation.avi
supplementary_movie_4_dual_channel.avi

12. Author contribution

A.I., T-Y.D.T., C.B.M., D.B. designed the study. A.I., T-Y.D.T., J.S., A.K. performed the experiments. A.I. analyzed the data. A.I., T-Y.D.T., J.S., A.K., C.B.M., D.B., T-Y.D.T. wrote the manuscript.

13. References

(1)   Ianeselli, A.; Mast, C. B.; Braun, D. Periodic Melting of Oligonucleotides by Oscillating Salt Concentrations Triggered by Microscale Water Cycles Inside Heated Rock Pores. *Angew. Chemie Int. Ed.* **58**, 13155-13160 (2019).

16

Bibliography

[1] A. Hampel and J. Cowan, "A unique mechanism for RNA catalysis: the role of metal cofactors in hairpin ribozyme cleavage," *Chemistry & Biology*, vol. 4, pp. 513–517, jul 1997.

[2] M. G. AbouHaidar and I. G. Ivanov, "Non-Enzymatic RNA Hydrolysis Promoted by the Combined Catalytic Activity of Buffers and Magnesium Ions," *Zeitschrift für Naturforschung C*, vol. 54, pp. 542–548, aug 1999.

[3] O. Taran, O. Thoennessen, K. Achilles, and G. von Kiedrowski, "Synthesis of information-carrying polymers of mixed sequences from double stranded short deoxynucleotides," *Journal of Systems Chemistry*, vol. 1, p. 9, aug 2010.

[4] J. W. Szostak, "The eightfold path to non-enzymatic RNA replication," *Journal of Systems Chemistry*, vol. 3, p. 2, feb 2012.

[5] A. Mariani, C. Bonfio, C. M. Johnson, and J. D. Sutherland, "pH-Driven RNA Strand Separation under Prebiotically Plausible Conditions," *Biochemistry*, vol. 57, pp. 6382–6386, nov 2018.

[6] J. Yoon, D. Thirumalai, and C. Hyeon, "Urea-Induced Denaturation of PreQ1-Riboswitch," *Journal of the American Chemical Society*, vol. 135, pp. 12112–12121, aug 2013.

[7] R. D. Blake and S. G. Delcourt, "Thermodynamic effects of formamide on DNA stability.," *Nucleic acids research*, vol. 24, pp. 2095–103, jun 1996.

[8] D. R. Mills, R. L. Peterson, and S. Spiegelman, "An extracellular Darwinian experiment with a self-duplicating nucleic acid molecule.," *Proceedings of the National Academy of Sciences of the United States of America*, vol. 58, pp. 217–224, jul 1967.

[9] C. De Duve, "The onset of selection," feb 2005.

[10] C. Schildkraut and S. Lifson, "Dependence of the melting temperature of DNA on salt concentration," *Biopolymers*, vol. 3, pp. 195–208, apr 1965.

[11] D. W. Gruenwedel and C.-H. Hsu, "Salt effects on the denaturation of DNA," *Biopolymers*, vol. 7, pp. 557–570, apr 1969.

[12] R. H. Waring, S. W. Running, R. H. Waring, and S. W. Running, "Water Cycle," *Forest Ecosystems*, pp. 19–57, jan 2007.

[13] S. M. Som, R. Buick, J. W. Hagadorn, T. S. Blake, J. M. Perreault, J. P. Harnmeijer, and D. C. Catling, "Earth's air pressure 2.7 billion years ago constrained to less than half of modern levels," *Nature Geoscience*, vol. 9, pp. 448–451, jun 2016.

[14] B. Marty, L. Zimmermann, M. Pujol, R. Burgess, and P. Philippot, "Nitrogen isotopic composition and density of the Archean atmosphere.," *Science (New York, N.Y.)*, vol. 342, pp. 101–4, oct 2013.

[15] E. Özgür and K. Koçak, "The effects of the atmospheric pressure on evaporation," *Acta Geobalcanica*, vol. 1, pp. 17–24, jul 2015.

[16] A. N. Kapanidis, N. K. Lee, T. A. Laurence, S. Doose, E. Margeat, and S. Weiss, "Fluorescence-aided molecule sorting: Analysis of structure and interactions by alternating-laser excitation of single molecules," *Proceedings of the National Academy of Sciences*, vol. 101, pp. 8936–8941, jun 2004.

[17] V. V. Didenko, "DNA probes using fluorescence resonance energy transfer (FRET): designs and applications.," *BioTechniques*, vol. 31, pp. 1106–16, 1118, 1120–1, nov 2001.

[18] F. J. Millero and A. Poisson, "International one-atmosphere equation of state of seawater," *Deep Sea Research Part A. Oceanographic Research Papers*, vol. 28, pp. 625–629, jun 1981.

[19] D. M. Considine, *Van Nostrand's scientific encyclopedia.* Van Nostrand Reinhold, 1989.

[20] S. Rahmstorf, "Thermohaline circulation: The current climate," *Nature*, vol. 421, pp. 699–699, feb 2003.

[21] M. Morasch, J. Liu, C. F. Dirscherl, A. Ianeselli, A. Kühnlein, K. Le Vay, P. Schwintek, S. Islam, M. K. Corpinot, B. Scheu, D. B. Dingwell, P. Schwille, H. Mutschler, M. W. Powner, C. B. Mast, and D. Braun, "Heated gas bubbles enrich, crystallize, dry, phosphorylate and encapsulate prebiotic molecules," *Nature Chemistry*, p. 1, jul 2019.

[22] L. Keil, M. Hartmann, S. Lanzmich, and D. Braun, "Probing of molecular replication and accumulation in shallow heat gradients through numerical simulations," *Physical Chemistry Chemical Physics*, vol. 18, pp. 20153–20159, jul 2016.

[23] J. F. Kasting, "Earth's early atmosphere.," *Science (New York, N.Y.)*, vol. 259, pp. 920–6, feb 1993.

[24] J. C. G. Walker, "Carbon dioxide on the early earth," *Origins of Life and Evolution of the Biosphere*, vol. 16, pp. 117–127, jun 1985.

[25] H. T. Byck, "Effect of dissolved CO2 on the pH of water.," *Science*, vol. 75, pp. 224–224, feb 1932.

[26] D. Carroll, S. L. Udall, and T. B. Nolan, "Rainwater as a Chemical Agent of Geologic Processes A Review Chemical composition of rainwater and its probable relation to soil water and exchangeable cations in weathering processes. United States Department of the Interior.," tech. rep.

[27] A. Wada and A. Suyama, "Local stability of DNA and RNA secondary structure and its relation to biological functions," *Proo. Biophys. molec. Biol*, vol. 47, pp. 113–157, 1986.

[28] A. F. Mason, N. A. Yewdall, P. L. W. Welzen, J. Shao, M. van Stevendaal, J. C. M. van Hest, D. S. Williams, and L. K. E. A. Abdelmohsen, "Mimicking Cellular Compartmentalization in a Hierarchical Protocell through Spontaneous Spatial Organization.," *ACS central science*, vol. 5, pp. 1360–1365, aug 2019.

[29] E. Sokolova, E. Spruijt, M. M. K. Hansen, E. Dubuc, J. Groen, V. Chokkalingam, A. Piruska, H. A. Heus, and W. T. S. Huck, "Enhanced transcription rates in membrane-free protocells formed by coacervation of cell lysate," *Proceedings of the National Academy of Sciences*, vol. 110, pp. 11692–11697, jul 2013.

[30] A. I. Oparin, "The Origin of Life and the Origin of Enzymes," in *Advances in enzymology and related areas of molecular biology*, vol. 27, pp. 347–380, Adv Enzymol Relat Areas Mol Biol, nov 2006.

[31] S. Koga, D. S. Williams, A. W. Perriman, and S. Mann, "Peptide-nucleotide microdroplets as a step towards a membrane-free protocell model," *Nature Chemistry*, vol. 3, pp. 720–724, sep 2011.

[32] M. Tena-Solsona, J. Janssen, C. Wanzke, F. Schnitter, H. Park, B. Rieß, J. M. Gibbs, C. A. Weber, and J. Boekhoven, "Kinetic Control over Droplet Ripening in Fuel-Driven Active Emulsions," oct 2019.

[33] J. Crosby, T. Treadwell, M. Hammerton, K. Vasilakis, M. P. Crump, D. S. Williams, and S. Mann, "Stabilization and enhanced reactivity of actinorhodin polyketide synthase minimal complex in polymer–nucleotide coacervate droplets," *Chemical Communications*, vol. 48, p. 11832, nov 2012.

[34] B. Drobot, J. M. Iglesias-Artola, K. Le Vay, V. Mayr, M. Kar, M. Kreysing, H. Mutschler, and T.-Y. D. Tang, "Compartmentalised RNA catalysis in membrane-free coacervate protocells," *Nature Communications*, vol. 9, p. 3643, dec 2018.

[35] R. R. Poudyal, R. M. Guth-Metzler, A. J. Veenis, E. A. Frankel, C. D. Keating, and P. C. Bevilacqua, "Template-directed RNA polymerization and enhanced ribozyme catalysis inside membraneless compartments formed by coacervates," *Nature Communications*, vol. 10, pp. 1–13, dec 2019.

[36] T. Y. Dora Tang, C. Rohaida Che Hak, A. J. Thompson, M. K. Kuimova, D. S. Williams, A. W. Perriman, and S. Mann, "Fatty acid membrane assembly on coacervate micro-droplets as a step towards a hybrid protocell model," *Nature Chemistry*, vol. 6, pp. 527–533, apr 2014.

[37] R. R. Poudyal, F. Pir Cakmak, C. D. Keating, and P. C. Bevilacqua, "Physical Principles and Extant Biology Reveal Roles for RNA-Containing Membraneless Compartments in Origins of Life Chemistry," may 2018.

[38] M. Santos, E. Zintzaras, and E. Szathmáry, "Origin of sex revisited.," *Origins of life and evolution of the biosphere : the journal of the International Society for the Study of the Origin of Life*, vol. 33, pp. 405–32, oct 2003.

[39] A. F. Mason, B. C. Buddingh, D. S. Williams, and J. C. Van Hest, "Hierarchical Self-Assembly of a Copolymer-Stabilized Coacervate Protocell," *Journal of the American Chemical Society*, vol. 139, pp. 17309–17312, dec 2017.

[40] H. M. Van Der Kooij, E. Spruijt, I. K. Voets, R. Fokkink, M. A. Cohen Stuart, and J. Van Der Gucht, "On the stability and morphology of complex coacervate core micelles: From spherical to wormlike micelles," *Langmuir*, vol. 28, pp. 14180–14191, oct 2012.

[41] S. Perry, Y. Li, D. Priftis, L. Leon, and M. Tirrell, "The Effect of Salt on the Complex Coacervation of Vinyl Polyelectrolytes," *Polymers*, vol. 6, pp. 1756–1772, jun 2014.

[42] N. Urakami, T. Jimbo, Y. Sakuma, and M. Imai, "Molecular mechanism of vesicle division induced by coupling between lipid geometry and membrane curvatures," *Soft Matter*, vol. 14, no. 16, pp. 3018–3027, 2018.

[43] R. R. Poudyal, C. D. Keating, and P. C. Bevilacqua, "Polyanion-Assisted Ribozyme Catalysis Inside Complex Coacervates," 2019.

List of my publications

PhD-related

Ianeselli, A.; Juanatey, M. A.; Kudella, P.; Gerland, U; Mast, C. B.; Braun, D. Water cycles in a Hadean CO_2 atmosphere drive DNA evolution. *Nature Physics* 2022. https://doi.org/10.1038/s41567-022-01516-z

Ianeselli, A.; Tetiker, D.; Stein, J.; Kühnlein, A.; Mast, C. B.; Braun, D.; Tang, D. T-Y.; Non equilibrium conditions inside rock pores drive fission, maintenance and selection of coacervate protocells. *Nature Chemistry* 2021. https://doi.org/10.1038/s41557-021-00830-y.

Ianeselli, A.; Mast, C. B.; Braun, D. Periodic Melting of Oligonucleotides by Oscillating Salt Concentrations Triggered by Microscale Water Cycles Inside Heated Rock Pores. *Angewandte Chemie International Edition* 2019. Very important paper. https://doi.org/10.1002/anie.201907909

Stein, J. A. C.; **Ianeselli, A.**; Braun, D. Kinetic Microscale Thermophoresis for Simultaneous Measurement of Binding Affinity and Kinetics. *Angewandte Chemie International Edition 2021.* https://doi.org/10.1002/anie.202101261

Morasch, M.; Liu, J.; Dirscherl, C. F.; **Ianeselli, A.**; Kühnlein, A.; Le Vay, K.; Schwintek, P.; Islam, S.; Corpinot, M. K.; Scheu, B.; et al. Heated Gas Bubbles Enrich, Crystallize, Dry, Phosphorylate and Encapsulate Prebiotic Molecules. *Nature Chemistry* 2019, 1. https://doi.org/10.1038/s41557-019-0299-5

Other

Ianeselli, A.; Orioli, S.; Spagnolli, G.; Faccioli, P.; Cupellini, L.; Jurinovich, S.; Mennucci, B. Atomic Detail of Protein Folding Revealed by an Ab Initio Reappraisal of Circular Dichroism. *Journal of American Chemical Society* 2018, 140 (10), 3674–3682. https://doi.org/10.1021/jacs.7b12399

Ianeselli, A.: Orioli, S.; Spagnolli, G.; Faccioli, P. All-Atom Calculation of Protein Free-Energy Profiles. *Journal of Chemical Physics* 2017, 147 (15), 152724. https://doi.org/10.1063/1.5006039

Spagnolli, G.; Massignan, T.; Astolfi, A.; Biggi, S.; Rigoli, M.; Brunelli, P.; Libergoli, M.; **Ianeselli, A.**; Orioli, S.; Boldrini, A.; et al. Pharmacological Inactivation of the Prion Protein by Targeting a Folding Intermediate. *Nature Communications Biology* 2021, 4 (1), 1–16. https://doi.org/10.1038/s42003-020-01585-x

Mittelberger, C.; Obkircher, L.; Oberkofler, V.; **Ianeselli, A.**; Kerschbamer, C.; Gallmetzer, A.; Reyes-Dominguez, Y.; Letschka, T.; Janik, K. Development of a Universal Endogenous QPCR Control for Eukaryotic DNA Samples. *Plant Methods* 2020, 16 (1). https://doi.org/10.1186/s13007-020-00597-2

Mittelberger, C.; Obkircher, L.; Oberkofler, V.;**Ianeselli, A.**; Kerschbamer, C.; Janik, K. Development of an endogenous universal internal control for qPCR applications and the importance of different evaluation criteria. *Phytopathogenic Mollicutes* 2019, 9 (1), 77-78. http://dx.doi.org/10.5958/2249-4677.2019.00039.2

Wang, F.; Orioli, S.; **Ianeselli, A.**; Spagnolli, G.; a Beccara, S.; Gershenson, A.; Faccioli, P.; Wintrode, P. L. All-Atom Simulations Reveal How Single-Point Mutations Promote Serpin Misfolding. *Biophysics Journal* 2018, 114 (9), 2083–2094. https://doi.org/10.1016/J.BPJ.2018.03.027